MEASUREMENT OF THE MUON CHARGE ASYMMETRY IN INCLUSIVE W BOSON PRODUCTION AT 7 TEV WITH CMS DETECTOR

A Dissertation

Presented to the Faculty of the Graduate School

of Cornell University

in Partial Fulfillment of the Requirements for the Degree of

Doctor of Philosophy

by

Aleko Khukhunaishvili

January 2014

MEASUREMENT OF THE MUON CHARGE ASYMMETRY IN INCLUSIVE W BOSON PRODUCTION AT 7 TEV WITH CMS DETECTOR

Aleko Khukhunaishvili, Ph.D.

Cornell University 2014

This thesis describes a precise measurement of the muon charge asymmetry in inclusive $pp \to W + X$ production at the center of mass energy of $\sqrt{s} = 7$ TeV of colliding protons. The data sample was collected with the Compact Muon Solenoid detector at the Large Hadron Collider and corresponds to an integrated luminosity of 4.7 fb^{-1}. The measurement was performed in 11 bins of the muon pseudorapidity within $|\eta| < 2.4$ range and for two thresholds on its transverse momentum: $p_T > 25$ GeV and $p_T > 35$ GeV.

Precise measurement of the muon charge asymmetry provides an important test for the Standard Model physics. Thanks to the large data sample, containing more than 20 million $W \to \mu\nu$ events, statistical precision is greatly improved compared with the previous lepton charge asymmetry results at the LHC. Total absolute uncertainty on the charge asymmetry varies within $0.2\% - 0.4\%$ in different muon pseudorapidity bins. The result provides significant constraints on the parton distribution functions of the proton in the Bjorken-x range from 0.001 to 0.1.

BIOGRAPHICAL SKETCH

Aleko Khukhunaishvili graduated from Vecua Physics-Math School (Tbilisi, Georgia) in 1999. In his last year of high school, Aleko won the silver medal at the XXX International Physics Olympiad (Padova, Italy), after which he entered Moscow Institute for Physics and Technology (Russia) to study undergraduate Physics. He received his Bachelor's and Master's degrees in Physics in 2004 and 2006, respectively. During his Master's program, he performed his scientific research at the Joint Institute for Nuclear Research (Dubna, Russia).

Aleko started his graduate study at Cornell University in Fall 2006. During the first two years he took classes and assisted undergraduate courses in Classical Mechanics and Heat & Electromagnetism. Having taken the Qualifying Exam, Aleko moved to CERN to do his graduate research in CMS experiment at the LHC (Geneva, Switzerland).

Aleko played a leading role in the precise measurement of the muon charge asymmetry, which is the main topic of this thesis. He also made a significant contribution to the development and commissioning of the *MET significance* algorithm in CMS, published in JINST in 2011. As a service project, he took Online Data Quality Monitoring shifts in 2011. In addition, Aleko also operated the Dataset Bookkeeping System (DBS), designed to catalog all CMS data; and developed a new, python-based DBS server prototype. He presented a talk on "W and Z production at CMS" at the DIS Conference (Marseille, 2013) on behalf of the CMS collaboration. Aleko received the NSF US LHC Student Support Award in 2010.

After graduation Aleko will continue working in CMS as a post-doctorate research associate at the University of Rochester.

To my family

ACKNOWLEDGEMENTS

I owe my gratitude to many people who helped me during my graduate work in physics and who made this dissertation possible. First and foremost, I am extremely lucky to have worked with Lawrence Gibbons who has been an excellent mentor throughout my graduate program in all regards. All my project works, presentations in various meetings and, in particular, this dissertation, have been performed under the close guidance of my advisor, for which I am extremely grateful. I have learnt a great deal from him, ranging from high energy physics and analysis techniques to details like best coding practices. I am forever indebted to him for all his effort and the time he took to help me grow into a physicist and a researcher.

I would also like to thank my other Special Committee members, Peter Wittich and Maxim Perelstein, for their help and support throughout my PhD program and for their thorough reviews of and suggestions about my dissertation. I am very grateful to Jim Alexander, Anders Ryd, Julia Thom, and Ritchie Patterson, as well as all the students, postdocs, and research associates of the Cornell HEP group, for creating a wonderful collegial atmosphere to enjoy doing physics in. Special thanks to Jim Alexander, Xin Shi, Freya Blekman and Nathan Mirman, with whom it was a great pleasure to work on the MET Significance. I would also like to thank Valentin Kuznetsov, who introduced me into the world of CMS computing and the Dataset Bookkeeping System.

It is a pleasure to thank Ping Tan, convener of the CMS muon charge asymmetry group, for his excellent supervision of this measurement and his masterful leading of the group through all steps of the analysis, documentation, and approval procedure. Ping also gets additional credit for the measurement of muon selection efficiencies, which is a crucial part of this analysis, and for

sharing the load of calculating NNLO theoretical predictions. Special thanks to Arie Bodek and Jiyeon Han, particularly, for deriving muon momentum correction factors, which is another key component of this measurement. I would also like to thank all the other members of muon charge asymmetry team, especially Saranya Gosh and Gobinda Majumber, for their important inputs and cross-checks in different critical steps of the analysis. I gratefully acknowledge the very important first study of the impact of our measurement on PDFs performed by our team of PDF experts: Ringaile Placakyte, Andrea Vargas, Marco Guzzi, Katerina Lipka, and Juan Rojo. Additional thanks to Ringaile and Marco for providing theoretical predictions with the DYNNLO and RESBOS tools.

I want to thank our Analysis Review Committee members: Michael Schmitt, Nicholas Hadley, Georg Steinbrueck, Konstantinos Fountas, and Richard Loveless, for their detailed review, comments, and suggestions on the analysis. Special thanks to the CMS SM Physics group conveners, Jeffrey Berryhill and Maxime Gouzevitch, for their constant support throughout all steps of the CMS analysis approval procedure. I would also like to thank the CMS Statistics Committee, particularly Louis Lyons, Ulrich Heintz, Bob Cousins, and Tomasso Dorigo, for useful suggestions and review of our fitting technique. I want to express my gratitude to all members of the CMS and LHC collaborations, without whose efforts this analysis would not have been possible.

It is a pleasure to thank Judy Swann for helping me proofread this thesis and greatly improve its readability.

I would like to thank all my friends and fellow colleagues who made my entire time spent in Ithaca and at CERN a wonderful experience. Finally, countless thanks to all my family — my wife and daughter, my parents and sister, for giving me so much love, support, and happiness.

TABLE OF CONTENTS

CHAPTER 1

INTRODUCTION

Hadron colliders have been the primary tool for exploring the energy-frontier of experimental particle physics. CERN's Large Hadron Collider (LHC) [2], which collides protons with unprecedented energies and luminosities, probes the fundamental interactions of nature at the shortest distances achieved to date. Since the LHC's startup in 2010, the Compact Muon Solenoid (CMS) [3], one of two high-luminosity experiments at the LHC, collected about 5 fb^{-1} of $\sqrt{s} = 7$ TeV and about 20 fb^{-1} of $\sqrt{s} = 8$ TeV data, which enabled numerous precise measurements and studies of rare processes in Standard Model (SM) physics. The discovery of the Higgs boson, predicted by the SM's electroweak theory about 40 years ago, is certainly the most remarkable achievement of the LHC to date. An extensive number of searches for signatures of beyond-the-SM (BSM) physics have also been performed. When the LHC starts up again in 2015, with $\sqrt{s} = 13$ TeV of colliding protons, the search will go on.

Since the proton is a composite object, the kinematics of the hard pp scattering process at the LHC is defined by the momenta of the proton's partons that are involved in a given hard interaction. Therefore, interpretation of LHC data requires knowledge of the densities of all constituent partons in the proton. These parton densities, described by Parton Distribution Functions (PDFs), are measured by analyzing data obtained from various fixed-target, lepton-hadron, and hadron-hadron scattering experiments.

Uncertainties in the PDFs often dominate the overall theoretical uncertainty of inclusive and differential cross sections of the processes studied at the LHC. Consequently, PDF uncertainties result in non-negligible contributions to sys-

tematic uncertainties in many current SM measurements. They also translate into uncertainties in SM backgrounds of BSM processes. Therefore, accurate knowledge of PDFs is crucial to performing precision measurements and detecting new physics at the LHC.

Due to their large production cross section and clean experimental signature, W and Z bosons and their leptonic decay are important SM standard candles at the LHC. These processes are extensively used for calibrating detector response and commissioning charged leptons and missing transverse energy. In addition, they provide a crucial test for the theoretical framework used to calculate inclusive and differential cross sections. At the same time, precise measurements of certain observables in the W and Z processes provide additional information to help constrain the PDFs in the proton. This thesis describes one of such measurements.

In pp collisions, W bosons are produced primarily through the annihilation of a valence quark from one of the protons with a sea antiquark from the other: $u\bar{d} \rightarrow W^+$, $d\bar{u} \rightarrow W^-$. Because of the presence of two valence u quarks in the proton, W^+ bosons are produced more often than W^- bosons. In this work we present a precise measurement of $pp \rightarrow W^\pm \rightarrow \mu^\pm\nu$ production asymmetry as a function of daughter muon pseudorapidity[1],

$$A(\eta) = \frac{\mathrm{d}\sigma(W^+ \rightarrow \mu^+\nu)/\mathrm{d}\eta - \mathrm{d}\sigma(W^- \rightarrow \mu^-\nu)/\mathrm{d}\eta}{\mathrm{d}\sigma(W^+ \rightarrow \mu^+\nu)/\mathrm{d}\eta + \mathrm{d}\sigma(W^- \rightarrow \mu^-\nu)/\mathrm{d}\eta}, \tag{1.1}$$

that is sensitive to the valence and sea quark distributions in the proton. At the same time, being a ratio, the charge asymmetry is free from many sources of systematic uncertainty and can therefore be measured with high accuracy.

[1] Pseudorapidity is defined as $\eta = -\ln[\tan(\theta/2)]$, where θ is a polar angle relative to the beam axis.

This thesis is organized as follows. In Chapter 2 we introduce the basic concepts of perturbative quantum chromodynamics (QCD) and PDFs that are used for calculating cross sections in proton-proton collisions. We then concentrate on W production in pp collisions and discuss the motivation for W charge asymmetry measurement in more detail, followed by a short review of previous asymmetry measurements made at the Tevatron and the LHC. In Chapter 3 we describe some basic characteristics of the LHC and the CMS detector. Chapter 4 discusses reconstruction algorithms for various physics objects in the CMS, such as muons. It also discusses missing transverse energy ($\not\!\!E_{\mathrm{T}}$), which is important to our analysis. Finally, in Chapter 5 we give a detailed overview of the muon charge asymmetry measurement we produced using the CMS detector and in Chapter 6 we summarize the results of this measurement and discuss the possible improvements and challenges in future measurements of the charge asymmetry in $\sqrt{s} = 8$ TeV and $\sqrt{s} = 13$ (14) TeV of pp collisions.

CHAPTER 2

OVERVIEW OF THE THEORETICAL BACKGROUND AND PREVIOUS MEASUREMENTS

Scattering processes at hadron colliders are described by Quantum Chromodynamics (QCD) [4, 5], which is a theory of the strong interactions between quarks and gluons — the constituents of hadrons.

The idea of quarks as the fundamental building blocks of matter was first suggested by Gell-Man [6] and Zweig [7] in 1964 to explain the observed spectra of hadron mass resonances. The concept of *color*, the charge of the strong interaction, was introduced to avoid a problem with the symmetric wave-function of baryons under the exchange of two quarks, which would contradict the Pauli principle. Several experimental measurements (e.g. full hadronic cross section of e^+e^- scattering) also indicated the need for an extra degree of freedom. In 1973, the idea of color was extended into the gauge $SU(3)_C$ theory of Quantum Chromodynamics (Fritzsch and Gell-Mann [8]). The fundamental constants of the QCD are the strong coupling constant g (or $\alpha_s = g^2/4\pi$) and masses of six quarks.

Quarks, which carry fractional electric charges, have never been observed as single particles in the experiment. This experimental fact is related to a property of strong interactions, called *confinement*, which implies that the quarks can only exist in color-less combinations of quark-antiquark pairs, called mesons, and bound states of three quarks, called baryons. When produced by high energy collisions, quarks and gluons hadronize and are revealed as *jets* of the final state hadrons, leptons and photons.

A distinctive property of QCD is *asymptotic freedom*, which implies that at short distances the strong coupling constant becomes so small that the quarks and gluons can be treated as approximately free particles within a hadron. It is this feature of strong interactions that allows application of the perturbative formalism of the quantum field theory to QCD at high energies [9, 10].

The first evidence of the asymptotically free behavior of the point-like constituents of protons came from Deep Inelastic Scattering (DIS) experiments at SLAC, when particle accelerators became powerful enough to probe the internal structure of hadrons. When scattering electrons off the protons, it was revealed that their structure functions did not depend on the momentum transfer Q, but only on $x = Q^2/M(E' - E)$, where E and E' are the energies of the incoming and outgoing lepton in the proton rest frame, respectively. This phenomenon, now known as Bjorken scaling, led Feynman (1969) [11] and Bjorken and Paschos (1969) [12] to the idea of *partons*, the point-like constituents of hadrons, which carry the fraction x of the hadron's total momentum with a certain distribution of probability, called parton distribution functions. These partons, after detailed studies of their properties, were identified with quarks, previously suggested from the hadron spectroscopy, and gluons — the particles responsible for the binding strong force.

This somewhat unintuitive behavior of the strong interaction, which becomes stronger at large distances (small energies) and weaker at small distances (large energies), follows naturally when quantum corrections from vacuum polarization are taken into account. Ultraviolet divergencies, which arise from the loop diagrams of quark and gluon self-interactions, are regulated with renormalization techniques. After the renormalization procedure, the strong cou-

pling constant acquires logarithmic μ-scale dependence. In leading-order approximation this dependence is given by the equation:

$$\alpha_s(\mu) \approx \frac{\alpha_s(\mu_0)}{1 + \frac{\beta_0}{4\pi}\alpha_s(\mu_0)\ln\left(\frac{\mu^2}{\mu_0^2}\right)} = \frac{4\pi}{\beta_0 \ln(\mu^2/\Lambda^2_{\mathrm{QCD}})}, \tag{2.1}$$

where $\alpha_s(\mu_0)$ is some reference value, Λ_{QCD} is the QCD scale where non-perturbative effects become important, and $\beta_0 = 11 - 2/3N_f$, where $N_f = 6$ is the number of quark flavors. At short distances, where $\mu^2/\Lambda^2_{\mathrm{QCD}} \to \infty$, $\alpha_s \to 0$, which confirms *asymptotic freedom*. At large distances, or equivalently, when momentum transfer approaches Λ_{QCD}, the coupling becomes very large, which is consistent with *confinement*. Such decreasing $\alpha_s = \alpha_s(\mu^2)$ dependence is driven by positive contribution to β_0 (i.e. +11) that arises from the non-Abelian gluon loop diagrams. These diagrams are characteristic of the strong interaction, because the propagator of the interaction (i.e. gluon) carries the charge of the interaction (i.e. color) and can, therefore, self-interact.

QCD does not predict the value of the strong coupling constant, only its scale-dependence, so it must be measured by experiment. Figure 2.1 summarizes numerous measurements of the strong coupling constant, performed at various experiments at different Q-scales, including the latest measurement at CMS of the three-jet mass [13]. One can see that the theory correctly predicts the universal scale-dependence of the strong coupling across three orders of magnitude, which provides the most powerful test of perturbative QCD and strong evidence of its validity. By convention, the value of the strong coupling is quoted at the reference scale of $\mu_0 = M_Z$. The current world average value is

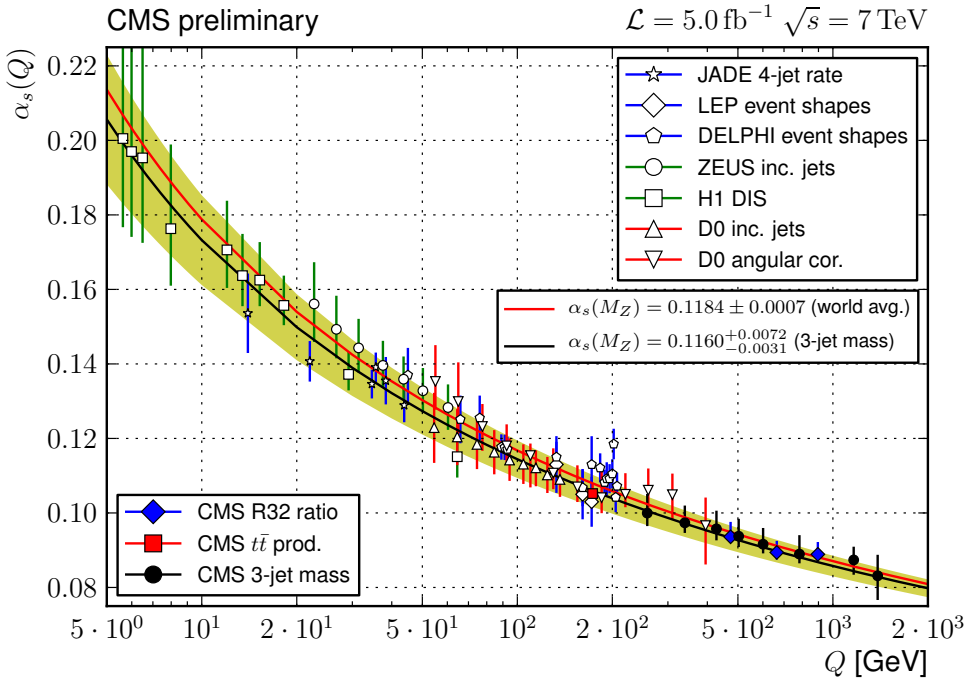

Figure 2.1: Comparison of various measurement of α_s at different Q-scales. The black curve shows the α_s evolution as determined from the latest 3-jet mass measurement at CMS, with the corresponding error band. The red curve shows the world-average α_s evolution [13].

$\alpha_s(M_Z) = 0.1184 \pm 0.0007$ [14].

2.1 Cross sections at hadron-hadron colliders

Calculation of production cross sections in hadron-hadron collisions with perturbative QCD relies on the concept of *factorization* [15]. This concept was first introduced by Drell and Yan [16] to extend the partonic model of hadrons, developed from DIS experiments, to hadron collisions. It was postulated that the total hadronic cross section of Drell-Yan production of a pair of muons, $\sigma(AB \to \mu^+\mu^- X)$, can be calculated by weighting the partonic level cross sec-

tions, $\hat{\sigma}(q\bar{q} \rightarrow \mu^+\mu^- X)$, with the *universal* parton distribution functions, $f_{a/A}(x)$ and $f_{b/B}(x)$, measured with DIS experiments:

$$\sigma_{AB\rightarrow\mu^+\mu^- X} = \sum_{a,b} \int \mathrm{d}x_a \mathrm{d}x_b f_{a/A}(x_a) f_{b/B}(x_b) \hat{\sigma}_{ab\rightarrow\mu^+\mu^- X}, \tag{2.2}$$

where $ab = q\bar{q}, \bar{q}q$. A good agreement between the theoretical predictions and the measured cross sections confirmed the applicability of the partonic model in hadron-hadron collisions and the method was extended to other hard scattering processes.

Perturbative corrections from real and virtual gluon emission result in logarithmic divergencies in the soft and collinear limits. These divergences are regulated by introducing a cut-off factorization scale μ_F, which separates the long and short distance physics. The divergent, non-perturbative part is absorbed into the definition of PDFs which, consequently, acquire logarithmic μ_F-dependence in accordance with the corresponding renormalization group equations, called Dokshitzer-Gribov-Lipatov-Altarelli-Parisi (DGLAP) evolution equations [17, 18]. The remaining finite part of the perturbative correction is process-specific, and can be expressed as a perturbative series of $\alpha_s(\mu_R)$, where μ_R is the renormalization scale for the running coupling. The generic cross section for $AB \rightarrow X$ process can thus be written as

$$\sigma_{AB\rightarrow X} = \sum_{a,b} \int \mathrm{d}x_a \mathrm{d}x_b f_{a/A}(x_a, \mu_F) f_{b/B}(x_b, \mu_F) \times [\hat{\sigma}_{LO} + \alpha_s(\mu_R)\hat{\sigma}_{NLO} + ...]_{ab\rightarrow X}. \tag{2.3}$$

Figure 2.2 shows the theoretical cross sections of various processes at the Tevatron and the LHC, calculated at NLO in perturbative QCD.

Factorization and renormalization scale dependencies of individual partonic cross sections $\hat{\sigma}_k$ are such that, when summed over all orders of perturbation series, they exactly cancel the explicit μ_R-dependence of the strong coupling and

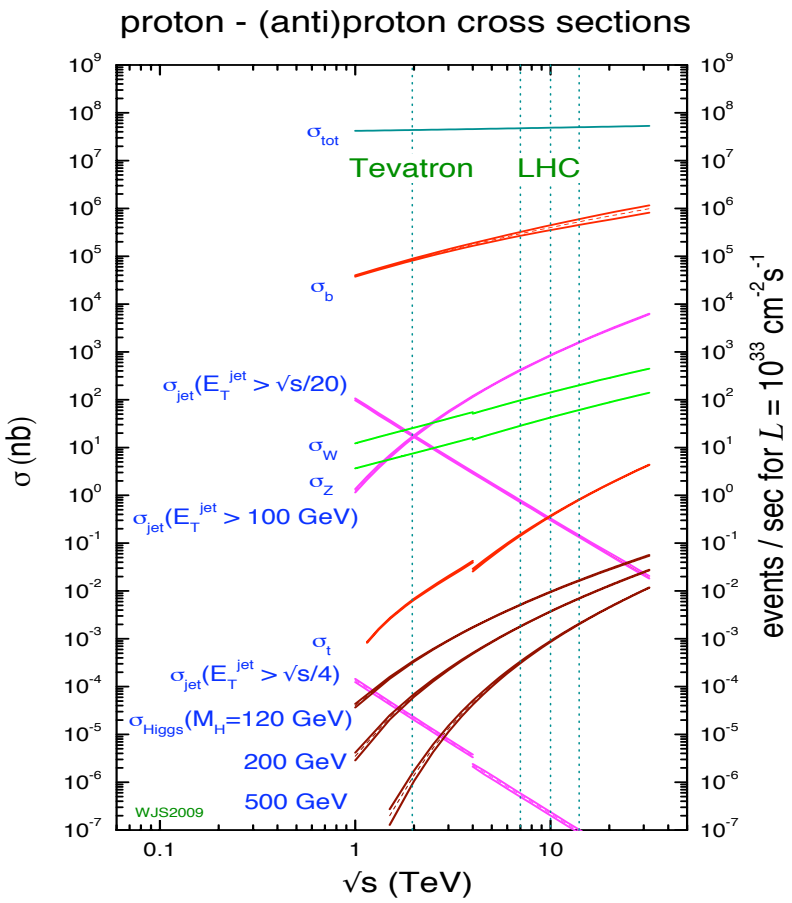

Figure 2.2: Standard Model cross sections of various processes at the Tevatron and the LHC, calculated at NLO in perturbative QCD [19].

μ_F-dependence of PDFs, so that the total cross section is independent of these parameters. In practice, however, only a limited number of perturbative terms can be calculated, since the complexity of the calculations increases dramatically with each order. As a result, calculated cross sections acquire artificial scale-dependence and the actual numerical results will depend on the choice of these parameters. Usually, they are both chosen to be equal to a typical scale of the process; e.g. in $pp \to W+X$ production it will be a mass of the W boson, $\mu_R = \mu_F = M_W$; and the theoretical uncertainty of the calculation is estimated by varying these scales by a factor of two $\mu_R = \mu_F = 0.5M_W, 2M_W$. Since this uncertainty

arises from the missing terms in the calculation, the higher the calculated order, the smaller the theoretical uncertainty associated with the renormalization and factorization procedure will be.

2.2 Parton Distribution Functions

In order to make theoretical predictions of the cross sections in pp collisions, knowledge of the parton distribution functions is required. The evolution of PDFs with the factorization scale μ is described by DGLAP equations,

$$\begin{aligned}\frac{\partial q_i(x,\mu^2)}{\partial \log \mu^2} &= \frac{\alpha_S}{2\pi}\int_x^1 \frac{\mathrm{d}z}{z}\left[P_{q_iq_j}(z,\alpha_S)q_j\left(\frac{x}{z},\mu^2\right) + P_{q_ig}(z,\alpha_S)g\left(\frac{x}{z},\mu^2\right)\right] \\ \frac{\partial g(x,\mu^2)}{\partial \log \mu^2} &= \frac{\alpha_S}{2\pi}\int_x^1 \frac{\mathrm{d}z}{z}\left[P_{gq_j}(z,\alpha_S)q_j\left(\frac{x}{z},\mu^2\right) + P_{gg}(z,\alpha_S)g\left(\frac{x}{z},\mu^2\right)\right] \end{aligned} \tag{2.4}$$

where $q(x,\mu^2)$ and $g(x,\mu^2)$ denote quark and gluon distribution functions, respectively; and P_{ab}'s are called kernel functions (or "splitting functions") and have perturbative expansions

$$P_{ab}(x,\alpha_S) = P_{ab}^{(0)} + \frac{\alpha_S}{2\pi}P_{ab}^{(1)} + ... \tag{2.5}$$

These splitting functions are known up to $P_{ab}^{(2)}$ and are normally used in the numerical solutions of the evolution equations.

QCD, however, cannot predict the PDFs themselves so, as is the case with the strong coupling, they must be measured experimentally. Since these are the universal distributions, they are measured by analyzing all available data of deep inelastic scattering, Drell-Yan and jet production processes, accumulated by various lepton-hadron and hadron-hadron scattering experiments.

Various processes from different experiments probe certain partons cover-

ing a limited region of $x - Q^2$ kinematic plane. The HERA data from the H1 and ZEUS experiments probe mostly the low-x region, while the fixed target DIS and DY data cover the higher x values. Collider data covers a wide range of $x - Q^2$ plane. Figure 2.3 (left) shows the parton kinematic plane of fixed target, HERA, and LHC experiments. As one can see, the LHC explores a new kinematic region. Therefore, theoretical calculations for hard-scattering processes have to rely on the evolution equations of PDFs determined from the previous experiments.

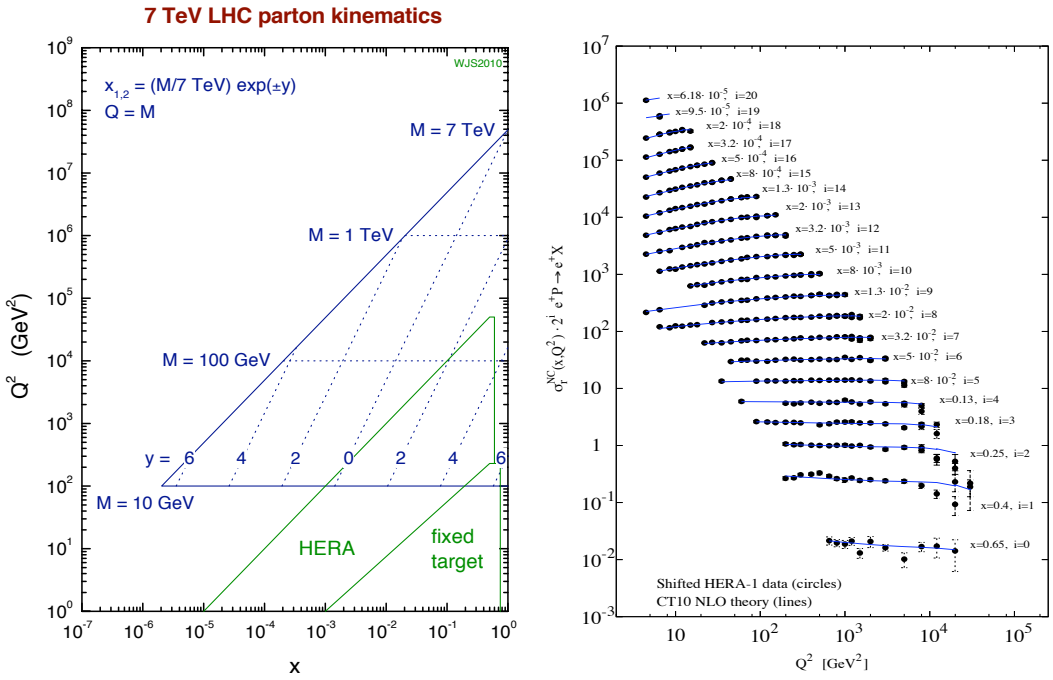

Figure 2.3: (left) Parton kinematic plane at fixed target, HERA and LHC experiments [19]. (right) NLO QCD fit of the neutral current cross sections at HERA experiments with CT10 PDF model [20].

There are several groups that perform the global PDF analysis. In this analysis we will focus on four of them: CTEQ [20], MSTW [21], NNPDF [22] and HERA [23]. The first three include most of the available data and are regarded as

global PDFs, while the HERA PDF relies primarily on the data from the H1 and ZEUS experiments. PDFs from various groups or versions of the same group usually differ due to different procedures in the analysis of the global data. The differences arise from a number of sources, including differences in the selected data sample used in the global PDF analysis, the QCD perturbation order, the treatment of experimental uncertainties, choice of the strong coupling value, factorization and renormalization schemes, treatment of heavy flavor quarks, assumptions at $x \to 0$ and $x \to 1$ limits, assumptions about the sea quarks etc [24].

Normally the PDFs are parameterized at some low $Q_0^2 \sim 1$ GeV^2 scale and are evolved with DGLAP equations in the global QCD fit to include the data points provided at various Q-scales. A typical parameterization is of the form:

$$xq(x; Q_0) = A_0 x^{A_1}(1-x)^{A_2} C(x; A_3, ...), \tag{2.6}$$

where A_1 and A_2 describe the behavior at $x \to 0$ and $x \to 1$ limits, respectively; and $C(x, A_3, ...)$ is a residual smooth function, which is different in various PDF models and provides an extra flexibility to allow accurate description of the parton density shapes. The parameterizations are constrained to obey the sum rules, dictated by the number of valence quarks in the proton:

$$\int_0^1 u_v(x, Q_0^2)\mathrm{d}x = 2, \quad \int_0^1 d_v(x, Q_0^2)\mathrm{d}x = 1, \quad \int_0^1 s_v(x, Q_0^2)\mathrm{d}x = 0. \tag{2.7}$$

where $q_v \equiv q - \bar{q}$. In addition, the total momentum carried by all partons must be equal to that of the proton:

$$\int_0^1 \left(g(x; Q_0) + \sum_i \left(q_i(x; Q_0) + \bar{q}_i(x; Q_0) \right) \right) x\mathrm{d}x = 1. \tag{2.8}$$

Figure 2.4 shows the typical processes that are used in the global PDF fit in, for example, the MSTW2008 analysis, along with involved partons and x-

ranges, in which the parton-densities are probed. A total of about 2700 data points are used in the NLO MSTW2008 global QCD fit. Figure 2.3 (right) shows the result of the NLO QCD fit of the HERA data subset of the neutral current cross sections in the CT10 PDF analysis.

Process	Subprocess	Partons	x range
$\ell^{\pm}\{p,n\} \to \ell^{\pm} X$	$\gamma^* q \to q$	$q, \bar{q}, g$	$x \gtrsim 0.01$
$\ell^{\pm} n/p \to \ell^{\pm} X$	$\gamma^* d/u \to d/u$	d/u	$x \gtrsim 0.01$
$pp \to \mu^+\mu^- X$	$u\bar{u}, d\bar{d} \to \gamma^*$	$\bar{q}$	$0.015 \lesssim x \lesssim 0.35$
$pn/pp \to \mu^+\mu^- X$	$(u\bar{d})/(u\bar{u}) \to \gamma^*$	$\bar{d}/\bar{u}$	$0.015 \lesssim x \lesssim 0.35$
$\nu(\bar{\nu})\, N \to \mu^-(\mu^+)\, X$	$W^* q \to q'$	$q, \bar{q}$	$0.01 \lesssim x \lesssim 0.5$
$\nu\, N \to \mu^-\mu^+ X$	$W^* s \to c$	s	$0.01 \lesssim x \lesssim 0.2$
$\bar{\nu}\, N \to \mu^+\mu^- X$	$W^* \bar{s} \to \bar{c}$	$\bar{s}$	$0.01 \lesssim x \lesssim 0.2$
$e^{\pm} p \to e^{\pm} X$	$\gamma^* q \to q$	$g, q, \bar{q}$	$0.0001 \lesssim x \lesssim 0.1$
$e^+ p \to \bar{\nu} X$	$W^+\{d,s\} \to \{u,c\}$	d, s	$x \gtrsim 0.01$
$e^{\pm} p \to e^{\pm} c\bar{c} X$	$\gamma^* c \to c$, $\gamma^* g \to c\bar{c}$	c, g	$0.0001 \lesssim x \lesssim 0.01$
$e^{\pm} p \to \text{jet} + X$	$\gamma^* g \to q\bar{q}$	g	$0.01 \lesssim x \lesssim 0.1$
$p\bar{p} \to \text{jet} + X$	$gg, qg, qq \to 2j$	g, q	$0.01 \lesssim x \lesssim 0.5$
$p\bar{p} \to (W^{\pm} \to \ell^{\pm}\nu)\, X$	$ud \to W, \bar{u}\bar{d} \to W$	$u, d, \bar{u}, \bar{d}$	$x \gtrsim 0.05$
$p\bar{p} \to (Z \to \ell^+\ell^-)\, X$	$uu, dd \to Z$	d	$x \gtrsim 0.05$

Figure 2.4: Processes used in MSTW2008 global QCD analysis, along with involved partons and approximate x-ranges probed. Processes are ordered in three groups: fixed target experiments, HERA and Tevatron [21].

In addition to the best PDF parameter values $\{S_0\}$, one also needs to know their uncertainties to estimate the theoretical errors of the calculated cross sections. Most of the PDF models use the Hessian method to estimate the uncertainties, except for NNPDF, which uses Monte-Carlo sampling. In the case of NNPDF, an ensemble of $n = 100$ (or 1000) PDF replicas are generated, which provide their correlated variations $\{S_k\}$ within their uncertainties. The central value and the error of some variable $F = F(S)$, due to uncertainties in PDFs can

be then calculated as:

$$\langle F \rangle = \frac{1}{n} \sum_{k=1}^{n} F(S_k)$$
$$\Delta F = \sqrt{\frac{n}{n-1} (\langle F^2 \rangle - \langle F \rangle^2)}. \tag{2.9}$$

In the Hessian approach (MSTW, CT10, HERA), a covariance $n \times n$ matrix from the global fit, where n is the number of free parameters, is first diagonalized to get the eigen-states in the free-parameter space. Each eigen-vector direction is then further scanned to provide asymmetric ΔS_k^+ and ΔS_k^- variations, corresponding to the $\Delta\chi^2$ tolerance for the required confidence interval (usually 68%), taking into account non-quadratic behavior of the χ^2 near the global minimum. Thus, a total of $2 \times n$ parameter variations are included in the PDF error set and the uncertainty on a variable $F = F(S)$ is calculated as

$$\Delta F = \frac{1}{2} \sqrt{\sum_{k=1}^{n} \left(F(S_k^+) - F(S_k^-) \right)^2}. \tag{2.10}$$

To calculate asymmetric uncertainties, the following equations should be used instead [25]:

$$(\Delta F)_+ = \left(\sum_{k=1}^{n} \left[\max \left(F(S_k^+) - F(S_k^0), F(S_k^-) - F(S_k^0), 0 \right) \right]^2 \right)^{1/2}$$
$$(\Delta F)_- = \left(\sum_{k=1}^{n} \left[\max \left(F(S_k^0) - F(S_k^+), F(S_k^0) - F(S_k^-), 0 \right) \right]^2 \right)^{1/2} \tag{2.11}$$

Since the strong coupling constant and the PDFs are both involved in the calculations, the best-fit PDF parameters depend on the choice of the value of α_S. Different PDF groups have different treatments of α_S, e.g. MSTW extracts the best α_S value from the fit, while NNPDF provides 100 PDF replicas for each value of the strong coupling between 0.114 and 0.124 in steps of 0.001. Table 2.1

summarizes the strong coupling values at which the PDF error sets are provided. For NNPDF set we will choose the value of $\alpha_S = 0.119$ in our calculations, which is consistent with current world average value from the PDG.

Table 2.1: Central strong coupling values for different PDF sets.

PDF set	$\alpha_S^{NLO}(M_Z)$
CT10	0.118
HERAPDF1.5	0.1176
MSTW2008	0.1202
NNPDF2.3	0.119

Figure 2.5 displays the parton distribution functions predicted by the MSTW2008 set at two Q^2 values with the corresponding error bands. For $Q^2 = 10^4$ GeV^2, parton distribution functions are boosted toward low momentum fractions with an increased contribution from gluons because at high Q^2 values, valence quarks radiate more gluons; and gluons split into quark-antiquark pairs.

2.3 W production at the LHC

A dominant mechanism of W-boson production in pp collisions at the LHC proceeds through the annihilation of a valence quark from one of the colliding protons with a sea antiquark from the other. The corresponding Feynman diagrams for a leptonic decay channel (muon, in our case) are shown in Fig. 2.6.

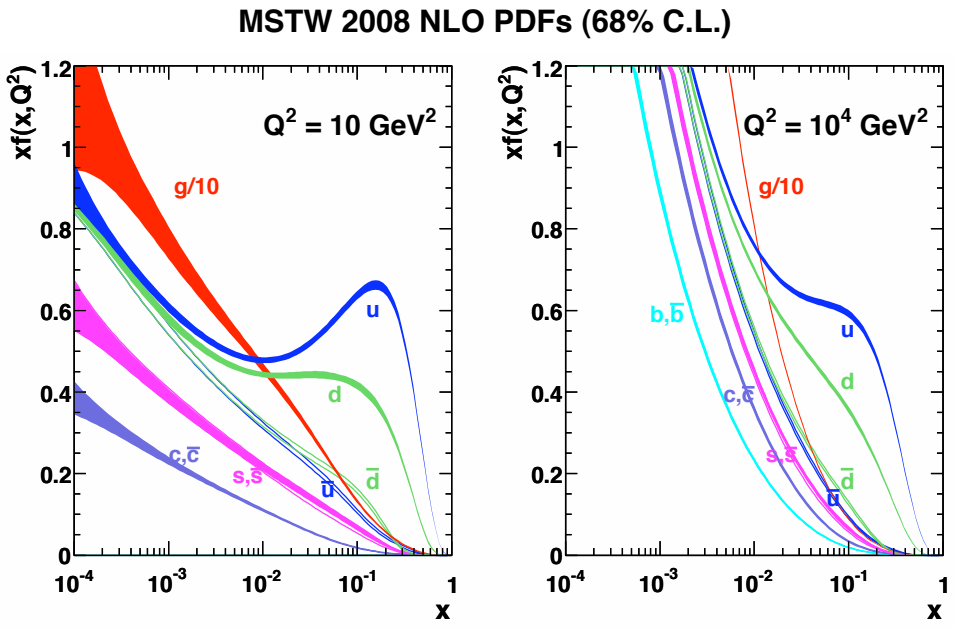

Figure 2.5: NLO MSTW2008 PDFs with 68 C.L. uncertainty band at different $Q^2 = 10$ GeV^2 (left) and $Q^2 = 10000$ GeV^2 (right) [21].

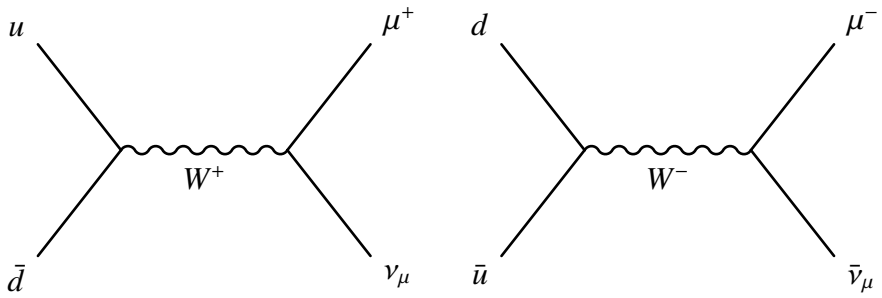

Figure 2.6: Feynman diagrams for leading order W production in a muon decay channel in proton-proton collisions at the LHC .

Given the four-momenta of the colliding partons,

$$\mathcal{P}_1 = \frac{\sqrt{s}}{2}(x_1, 0, 0, x_1),$$
$$\mathcal{P}_2 = \frac{\sqrt{s}}{2}(x_2, 0, 0, -x_2),$$

the fractional momenta $x_{1,2}$ of the partons can be related with the mass and the

rapidity $y = 0.5 \ln[(E + p_z)/(E - p_z)]$ of the W as:

$$M^2 = \mathcal{P}_W^2 = (\mathcal{P}_1 + \mathcal{P}_2)^2 = s x_1 x_2 \tag{2.12}$$

$$y = \frac{1}{2} \ln \frac{\mathcal{P}_{W_0} + \mathcal{P}_{W_3}}{\mathcal{P}_{W_0} - \mathcal{P}_{W_3}} = \frac{1}{2} \ln \frac{x_1}{x_2}, \tag{2.13}$$

where $\sqrt{s}$ is the center of mass energy of colliding protons. Therefore, a given W rapidity corresponds to the following x-values of the partons:

$$x_{1,2} = \frac{M}{\sqrt{s}} \exp(\pm y). \tag{2.14}$$

CMS can detect W bosons up to a rapidity of ~ 2.5 in its leptonic decay channel, limited by the fiducial coverage of the tracking system used to detect the charged leptons from the decay. Therefore, with W production studies CMS can effectively probe the parton densities in $0.001 \lesssim x \lesssim 0.1$ range.

In leading order, the partonic cross section for $W^{\pm}$ production is given by:

$$\hat{\sigma}(q\bar{q}' \to W) = \frac{\sqrt{2}\pi}{3} G_F M^2 |V_{qq'}|^2 \delta(\hat{s} - M^2), \tag{2.15}$$

where$V_{qq'}$ is the CKM matrix element, and $\hat{s} = x_1 x_2 s$ is the square of center-of-mass energy of the partonic system. Factorization Eq. 2.3, upon integrating over $\hat{s}$, leads the following expressions for the differential cross sections of W^+ and W^- production:

$$\begin{aligned}
\frac{\mathrm{d}\sigma(u\bar{d} \to W^+)}{\mathrm{d}y} &= \frac{\sqrt{2}\pi}{3} \frac{G_F M^2 |V_{ud}|^2}{s} \Big(u(x_1)\bar{d}(x_2) + u(x_2)\bar{d}(x_1) \Big), \\
\frac{\mathrm{d}\sigma(d\bar{u} \to W^-)}{\mathrm{d}y} &= \frac{\sqrt{2}\pi}{3} \frac{G_F M^2 |V_{ud}|^2}{s} \Big(d(x_1)\bar{u}(x_2) + d(x_2)\bar{u}(x_1) \Big),
\end{aligned} \tag{2.16}$$

where $x_{1,2}$ are given by Eq. 2.14. We have restricted ourselves to first generation quark-antiquark annihilation, which dominates the total cross section because the valence quarks are first generation. In these equations the parton densities should be evaluated at the W mass scale: $q(x) = q(x; \mu_F = M_W)$.

The next-to-leading (NLO) order QCD corrections to the W production cross sections, which are $O(\alpha_s)$, involve virtual corrections (loop diagrams) and real emission of gluons and quarks from initial state quarks and gluons, respectively. Figure 2.7 depicts example Feynman diagrams that lead to NLO QCD corrections to the original LO diagram of W^+ production. In leading order, W bosons are produced with zero transverse momentum when the transverse motion of the colliding partons are neglected. At NLO, W bosons can recoil against the emitted quarks and gluons with a sizable transverse momentum. This is the dominant production mechanism for W + 1 jet events.

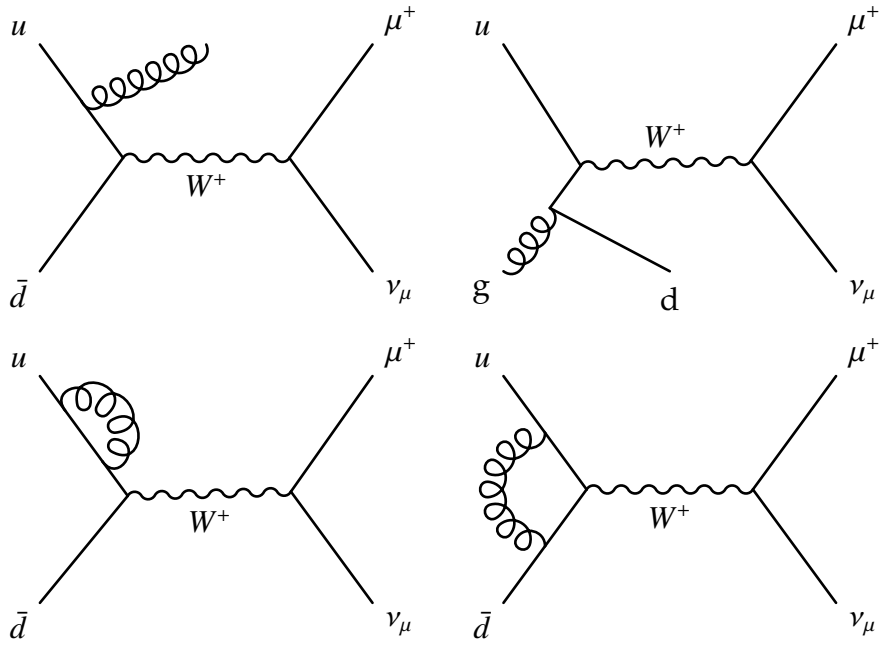

Figure 2.7: Example Feynman diagrams of real (top) and virtual (bottom) NLO QCD corrections to LO W^+ production in the muon decay channel.

Calculation of the vector boson production cross sections is available at next-to-next-to (NNLO) leading order in QCD, $O(\alpha_s^2)$ [26]. It has been found that while the NLO QCD corrections to vector boson production is significant, the NNLO corrections are relatively small. Figure 2.8 shows the differential cross

sections of W^+ and W^- production in proton-proton collisions calculated at LO, NLO and NNLO in perturbative QCD at $\sqrt{s} = 14$ TeV. The PDFs were modeled with MRST set in these calculations. The error band shows the variation in the calculated cross sections when the factorization and renormalization scales are varied within a factor of two: $M/2 \leq \mu \leq 2M$. As expected, the theoretical uncertainty associated with the choice of these scales reduces dramatically with each order of perturbation series.

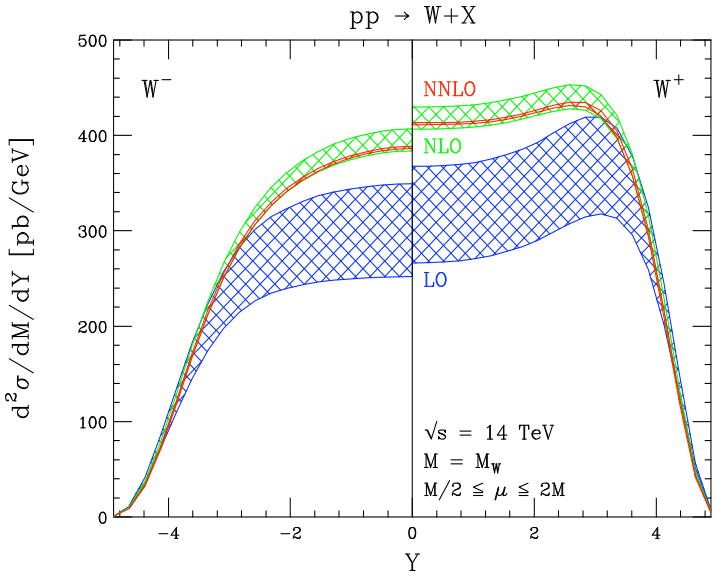

Figure 2.8: Differential $W^{\pm}$ production cross section as a function of y in pp collisions with $\sqrt{s} = 14$ center-of-mass energy, calculated at LO, NLO and NNLO in perturbative QCD. The MRST PDF model is used. The uncertainty bands reflect the variation of the renormalization and factorization scales in $M/2 \leq \mu \leq 2M$ range [27].

In this analysis the main reference theoretical predictions will be performed at NLO. However, we will also study the impact of the NNLO QCD corrections.

2.4 W and lepton charge asymmetry

Experimentally W's are normally observed through their leptonic decays, which have a branching fraction of about 11%[1]. A typical $W^{\pm} \to l^{\pm}\nu$ event is characterized by one isolated high-p_T charged lepton and large missing transverse energy, introduced by the neutrino.

Due to the excess of the u valence quark over d, from Eqs. 2.16 one can see that there will be more W^+ than W^- produced. One usually considers the differential charge asymmetry as a function of W rapidity, defined as

$$A(y) = \frac{\mathrm{d}\sigma(W^+)/\mathrm{d}y - \mathrm{d}\sigma(W^-)/\mathrm{d}y}{\mathrm{d}\sigma(W^+)/\mathrm{d}y + \mathrm{d}\sigma(W^-)/\mathrm{d}y}. \tag{2.17}$$

In the leading order approximation, assuming the sea anti-quark contributions to proton momentum to be equal ($\bar{u} \approx \bar{d}$), for the central rapidity ($y = 0$) the expression above simplifies to

$$A(0) \approx \frac{u(x_0) - d(x_0)}{u(x_0) + d(x_0)} = \frac{u_v(x_0) - d_v(x_0)}{u_v(x_0) + d_v(x_0) + 2\bar{q}(x_0)}, \tag{2.18}$$

where $x_0 = M_W/\sqrt{s} \approx 0.01$. So, at central rapidity we expect some non-zero asymmetry and the value will depend on the excess of $u(x_0)$ over $d(x_0)$.

As one increases the W rapidity, one of the partons acquires a higher x-value and the other parton acquires a lower x-value, according to the Eq. 2.14. Assuming u and d parton densities are roughly equal for low x, since they are dominated by the sea contribution, at high W rapidities the asymmetry can be described with the same expression above, with x_0 now being the largest momentum fraction of the two partons. Since the $u(x)/d(x)$ ratio increases with x as we probe more of the valence quarks, the asymmetry is expected to be larger

[1]Hadronic decay channels, despite having a total branching fraction of $\sim$ 67%, are overwhelmed by QCD dijet background.

for the high W rapidity values. Therefore, by measuring the asymmetry as a function of W rapidity, one can directly probe the shapes of the valence and sea quark distribution functions.

There is, however, an experimental complication associated with the fact that leptonic decay of a W boson always involves an undetected neutrino, whose longitudinal momentum cannot be measured. Therefore, the full momentum of the W and, hence, its rapidity, cannot be directly reconstructed. A commonly accepted approach is to measure the charge asymmetry as a function of the decay charged lepton pseudorapidity η, defined as

$$A(\eta) = \frac{\mathrm{d}\sigma(W^+ \to \mu^+\nu)/\mathrm{d}\eta_\mu - \mathrm{d}\sigma(W^- \to \mu^-\nu)/\mathrm{d}\eta_\mu}{\mathrm{d}\sigma(W^+ \to \mu^+\nu)/\mathrm{d}\eta_\mu + \mathrm{d}\sigma(W^- \to \mu^-\nu)/\mathrm{d}\eta_\mu}. \tag{2.19}$$

The muon charge asymmetry is not directly related to PDFs but instead is a convolution of the original W charge asymmetry by its anisotropic decay into the muon and the neutrino. Because of the $V - A$ nature of the charged weak current, which couples to only the left-handed fermions and right-handed anti-fermions, the μ^- will prefer to follow the direction of the incoming quark, while the μ^+ will prefer the direction of the anti-quark. The opening angle θ^* between the charged lepton and the incoming quark in the rest frame of the W is distributed as $(1 \pm \cos\theta^*)^2$. The schematic diagrams of $u\bar{d} \to W^+ \to \mu^+\nu$ and $d\bar{u} \to W^- \to \mu^-\bar{\nu}$ processes are shown in Fig. 2.9.

The muon pseudorapidity in the lab frame can be expressed in terms of the W rapidity in the same frame and the muon pseudorapidity in the W rest frame as:

$$\eta_\mu = y_W + \eta^*_\mu \approx y_W + \frac{1}{2}\ln\frac{1+\cos\theta^*}{1-\cos\theta^*}. \tag{2.20}$$

Because the quarks carry a larger average fraction of the proton momentum

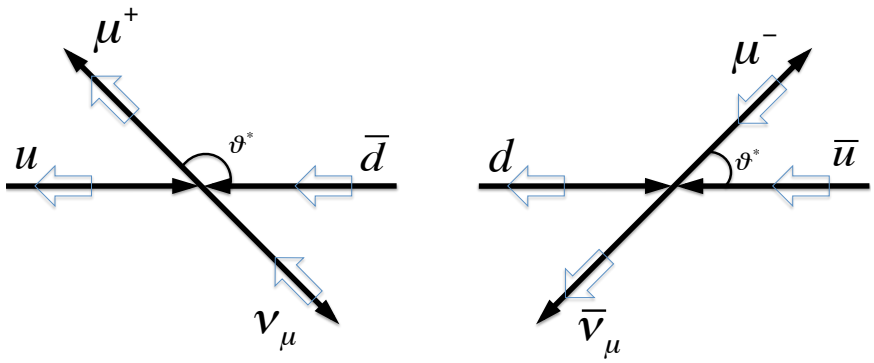

Figure 2.9: Schematic diagram for $u\bar{d} \to W^+ \to \mu^+\nu$ (left) and $d\bar{u} \to W^- \to \mu^-\nu$ (right) production. The black solid arrows show the momentum direction, while the blue open arrows show the direction of spin. The μ^- prefers to follow the direction of the incoming quark, while the μ^+ prefers the direction of the antiquark.

than the antiquarks, W's are more likely to be boosted in the quark direction, and the larger the boost the more likely it is so. Therefore, W^+ (W^-) bosons with, say, large positive rapidity are mostly produced through the annihilation of u (d) quarks, moving in the positive z direction and having a large x-value, with $\bar{d}$ ($\bar{u}$) antiquarks, moving in the opposite direction and having a small x-value. Therefore, the daughter μ^+ (μ^-) muons, which prefer to go against (in) the direction of incoming u (d) quarks, will tend to have negative (positive) pseudorapidity in the rest frame of the W. The situation is reversed when considering negative W rapidities. This effect results in the η_{μ^+} distribution boosted towards more central rapidities compared with the y_{W^+}, while the η_{μ^-} distribution gets wider and spreads over the higher rapidities, compared with y_{W^-}. Therefore, the lepton charge asymmetry is larger than the W charge asymmetry at central rapidities, and is smaller at high rapidities. The inclusive $pp \to WX^\pm \to \mu^\pm\nu X$ signal Monte-Carlo sample, described in Section 5.1.5, clearly shows this effect (see Fig. 2.10).

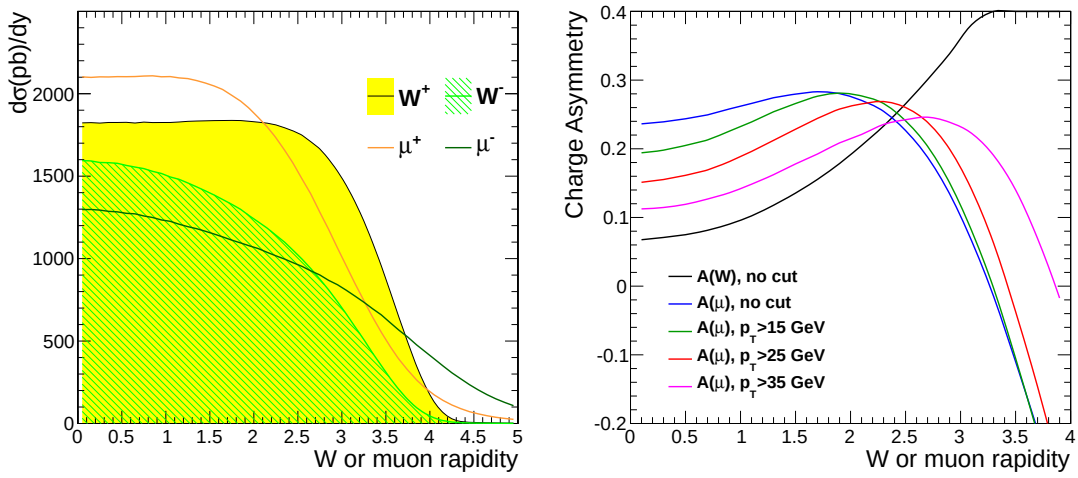

Figure 2.10: Distribution of W and muon rapidities (left) and charge asymmetries with different p_T threshold on the muon (right) in inclusive $pp \to WX^{\pm} \to \mu^{\pm}\nu X$ production, as modeled with POWHEG Monte-Carlo sample, interfaced with CT10 PDF set.

The lepton charge asymmetry is often measured within a certain fiducial region of pseudorapidity and transverse momentum of the charged lepton. The pseudorapidity coverage is normally limited by the tracker detector, while the p_T threshold is typically applied at the online trigger level to reduce the backgrounds. Figure 2.10 shows the change in the muon charge asymmetry when different thresholds are applied to its transverse momentum. When applying the p_T requirement, one removes mostly the boosted events around $\cos\theta^* \sim \pm 1$, which are mainly responsible for the difference between the W and muon charge asymmetries. Therefore, a higher p_T threshold will result in a smaller asymmetries in central bins and larger asymmetries at high rapidities.

Since the charge asymmetry is sensitive to the parton distribution functions, it provides discrimination among the PDF models that predict different shapes of valence and sea quark distribution. Figure 2.11 (left) shows a comparison of

the valence quark distributions for MSTW and CT10 PDF models evaluated at $Q^2 = M_W^2$. As one can see, their valence quark distributions are slightly different, particularly near $x \sim 0.01$, where CT10 predicts larger u but smaller d valence quark density compared with MSTW.

Figure 2.11 (right) shows the lepton charge asymmetries corresponding to MSTW and CT10 PDF models, calculated with FEWZ [28] at the NLO QCD, for $p_T > 25$ GeV threshold. As expected, at central rapidities, which correspond to $x_1 = x_2 \approx 0.01$, the disagreement is most visible and CT10 predicts larger charge asymmetry. Uncertainties in the CT10 (MSTW) PDF parameters translate to about 0.7% (0.5%) in the absolute uncertainty of the lepton charge asymmetry at central rapidities. The disagreement between the two predictions is about 2%. Therefore, measurement of the lepton charge asymmetry with a sub-percent precision can discriminate between different PDF sets and constrain their uncertainties. In Section 5.6.4 we will also consider other PDF sets and look at the effect of NNLO QCD corrections on the muon charge asymmetry.

2.5 Previous asymmetry measurements

W and lepton charge asymmetries have been measured by the CDF and D0 experiments at the Tevatron collider. In $p\bar{p}$ collisions W^+ (W^-) bosons are primarily produced by the annihilation of a valence u (d) quark in the proton with valence $\bar{d}$ ($\bar{u}$) quark in the antiproton. The total production cross sections of W^+ and W^- are equal. However, since the average momentum carried by u quark of the proton is larger than the average momentum carried by a $\bar{d}$ antiquark of the antiproton, W^+ will be boosted in the proton momentum direction, and the W^-

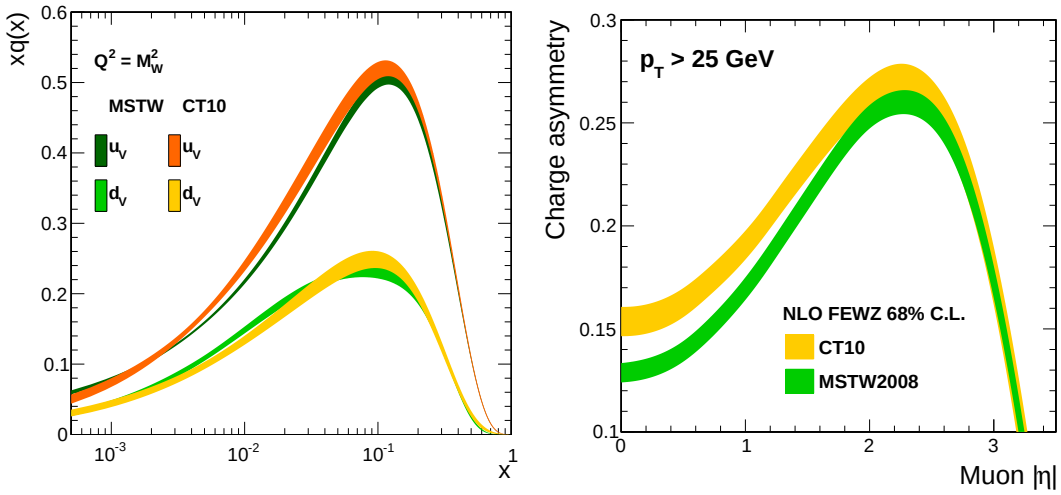

Figure 2.11: (left) Comparison of valence quark distributions between CT10 and MSTW PDF models at $Q^2 = M_W^2$. (right) Lepton charge asymmetries, calculated at NLO QCD with MSTW and CT10 PDF sets for $p_T > 25$ GeV threshold on the muon.

will be boosted in the antiproton momentum direction. This effect results in the rapidity-dependent charge asymmetry, which is asymmetric with respect to $y = 0$.

CDF has measured the charge asymmetry as a function of the W-rapidity by using the W mass constraint to recover the longitudinal momentum of the neutrino [29]. This constraint results in a quadratic equation that in general yields two rapidity solutions. Both solutions are used in this technique. Each rapidity solution is weighted according to the probabilities derived from MC simulation[2] and parameterized as a function of W charge, rapidity, transverse momentum, and the muon polarization angle in the W rest frame. Figure 2.12 (left) depicts the resulting W asymmetry distribution, showing good agreement with the theoretical prediction from the CTEQ PDF set. This result is included in most of

[2]The procedure is iterated to remove the possible bias in input from MC simulation.

the recent PDF fits.

The latest D0 W charge asymmetry measurement was performed in a muon decay channel with 7.3 fb^{-1} of the Tevatron data. The fiducial region was defined as $p_T^{\mu} > 25$ GeV and $E_T^{\nu} > 25$ GeV [30]. The resulting asymmetry distribution is depicted in Fig. 2.12 (right), showing excellent agreement with the theoretical predictions of the CT10 (CTEQ) PDF model. The measured asymmetries have consistently higher values compared with MSTW2008 predictions, though the two theoretical predictions are within the quoted uncertainty band.

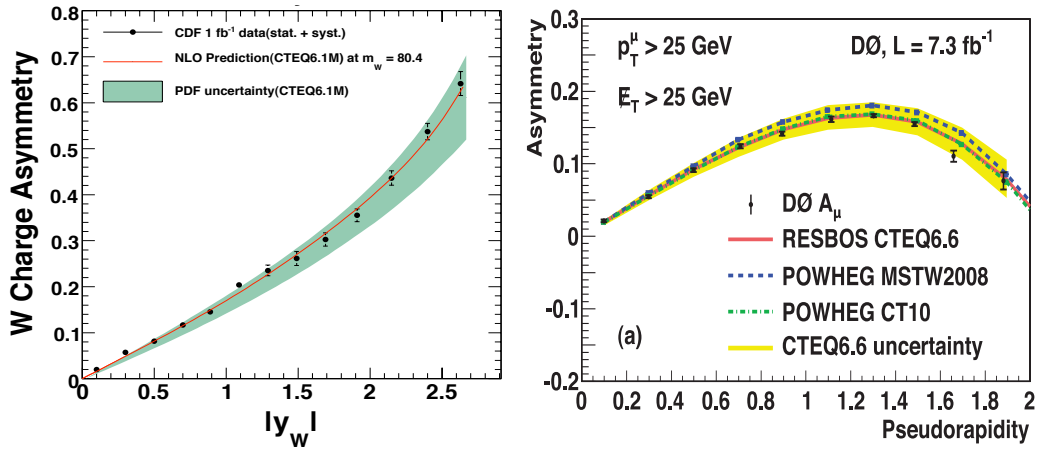

Figure 2.12: W and lepton charge asymmetries at CDF (left) [29] and D0 (right) [30] experiments.

The three LHC experiments — CMS, ATLAS and LHCb — measured lepton charge asymmetries with the first 35 pb^{-1} of 7 TeV data delivered in 2010. CMS measured both muon and electron charge asymmetries with $p_T > 25$ GeV and $p_T > 35$ thresholds on the charged lepton in 6 $|\eta|$ bins up to $|\eta| < 2.1$ [31]. ATLAS measured the combined lepton charge asymmetry within the fiducial region, defined by the following cuts on the lepton and $\not{E}_{\mathrm{T}}$: $p_T^l > 20$ GeV, $\not{E}_{\mathrm{T}} > 25$ GeV, $M_T > 40$ GeV [32]. LHCb provided the complementary measurement of

the muon charge asymmetry with $p_T > 25$ GeV threshold, extending the pseudorapidity coverage from $|\eta| = 2.1$ to $|\eta| = 4.5$ [33]. The measured asymmetry distributions from ATLAS and LHCb experiments are shown in Fig. 2.13.

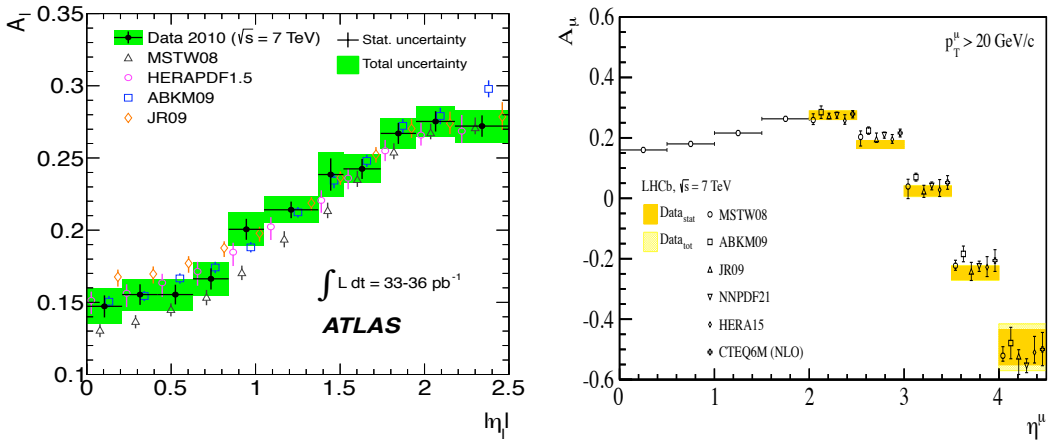

Figure 2.13: Lepton charge asymmetry measurements from ATLAS (left) [32] and LHCb (right) [33] experiments.

CMS has further updated the electron charge asymmetry measurement with the first 840 pb^{-1} of 7 TeV data, within the $p_T > 35$ GeV fiducial region, driven by the single electron trigger threshold [34]. The results, shown in Fig. 2.14 (left) was included in the global PDF analysis of NNPDF2.3 and was found to have significant impact on PDF uncertainties. Preliminary results of muon charge asymmetry measurement using the first 235 pb^{-1} of CMS data is also available [35].

The current analysis, described in this thesis, is based on the full 7 TeV dataset, collected by CMS during the 2011 operation and includes most of the sample used in the previous muon asymmetry measurement. Therefore, our result will supersede the previous muon asymmetry measurement.

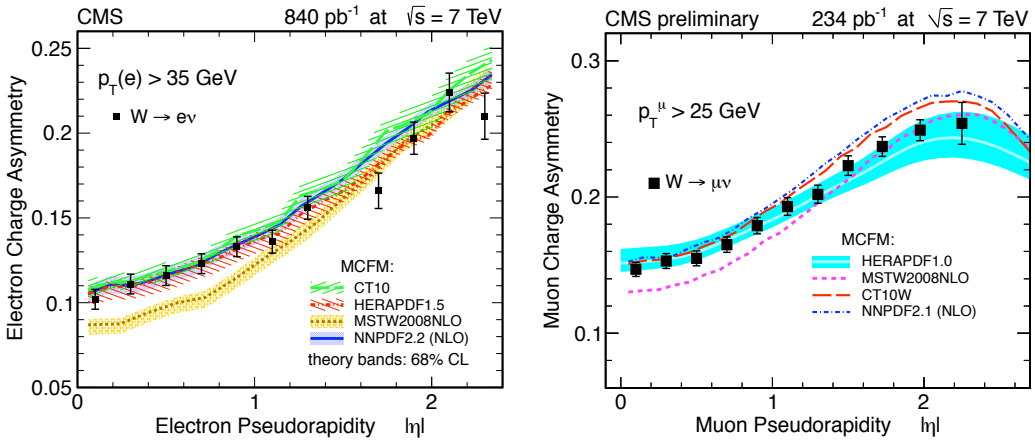

Figure 2.14: Latest electron asymmetry measurement (left) [34] and preliminary muon charge asymmetry results (right) [35] at CMS.

CHAPTER 3

EXPERIMENTAL APPARATUS

The dataset used in our muon charge asymmetry measurement was collected with the CMS detector which is installed at one of the high-luminosity interaction points (IP) of the LHC — the world's largest and most energetic particle collider. The primary motivation of the LHC is to explain electroweak symmetry breaking and to search for signatures of new physics beyond the SM. It is designed to collide protons at the center-of-mass energy of 14 TeV with a nominal instantaneous luminosity of 10^{34} $cm^{-2}s^{-1}$. During the 2011 (2012) Run, the LHC operated at a center-of-mass energy of 7 (8) TeV.

The seven-fold increase in energy and the hundred-fold increase in designed integrated luminosity over the previous hadron collider experiments significantly amplifies the discovery potential of the LHC. We can also explore particle physics at the TeV scale and can make precise measurements of high cross section processes. These extraordinary conditions, however, present significant challenges. At the design luminosity, the LHC's general-purpose detectors will observe 10^9 inelastic events per second, with thousands of particles emerging from the interaction point every 25 ns. These conditions require careful design of an online trigger system and pose stringent requirements on the time resolution and granularity of the different sub-detectors. Moreover, the radiation hardness of the detectors and the front-end electronics must be able to cope with the intense particle fluxes coming out of the interaction region. In this Chapter we review the basic characteristics of the LHC, as well as the various

sub-detectors and online trigger system of the CMS.

3.1 Large Hadron Collider

The LHC is a two-ring-superconducting hadron collider installed in an underground tunnel of 26.7 km circumference. The tunnel was originally constructed for the Large Electron Positron collider on the French-Swiss border near Geneva, Switzerland.

The LHC is supplied with protons by the series of acceleration steps displayed in Fig. 3.1. First, an ion source is used to strip electrons from hydrogen atoms. The resulting protons are accelerated through a 30-meter long linear accelerator LINAC to 50 MeV. Then they are injected into the Proton Synchrotron Booster (PSB), where they reach an energy of 1.4 GeV. In the next sequence, the Proton Synchrotron (PS) accelerates them to 26 GeV; the Super Proton Synchrotron increases their energy to 450 GeV; and finally they are injected into the LHC ring, where they reach a final designed energy of 3.5 TeV (in 2011), 4 TeV (in 2012) or 7 TeV (design). The basic characteristics of each machine are listed in Table 3.1.

Protons in the PS, SPS and LHC are accelerated using electric fields that are fed into Radio-Frequency (RF) cavities, which serve as resonators tuned to a specific frequency. Circular acceleration is done in many turns. In the LHC tunnel, it takes about 20 minutes to accelerate from 450 GeV to 7 TeV, with an average increase of 0.5 MeV in each turn. The RF systems provide longitudinal focusing, which constrains protons in a longitudinal phase-space to confined regions called RF buckets. The radio frequency of the LHC is 400 MHz, which

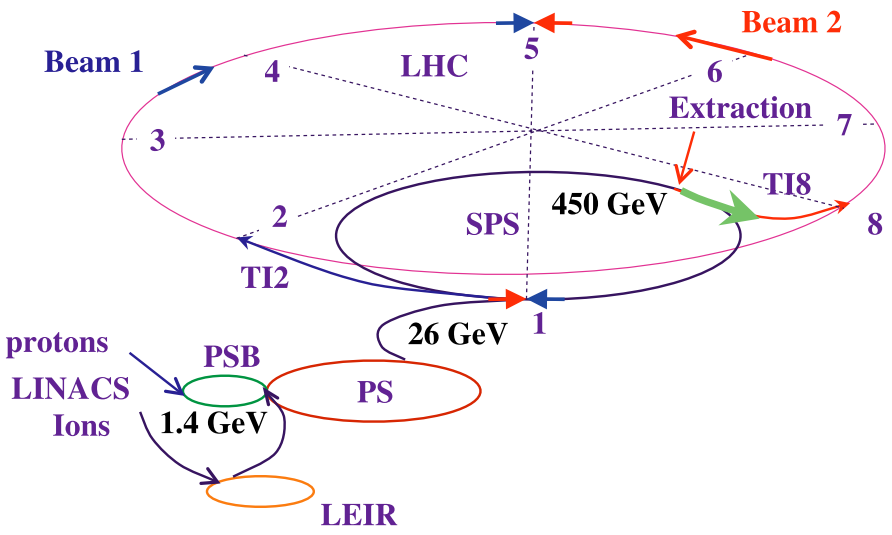

Figure 3.1: Schematic of the CERN accelerator complex [36].

corresponds to buckets of 2.5 ns in length. The design proton-bunch spacing at LHC is 10-RF buckets or 25 ns. During the 2011 data collection, the LHC operated with bunch spacing of 75 ns and 50 ns.

Table 3.1: Basic characteristics (length or circumference L, bending radius ρ and reached beam momentum p) of accelerators in proton acceleration chain at the LHC [36].

Machine	L(m)	ρ (m)	p (GeV)	Bunches
Linac2	30	–	0.05	4×2
PSB	175	8.3	1.4	4×2
PS	628	71	26	72
SPS	6912	741	450	4×72
LHC	26659	2804	7000	2×2808

The LHC tunnel consists of eight straight sections of about 528 m in length, and 8 arcs covering a total of about 22 km. Protons in the arcs are bent by dipole magnets. In order to achieve the momentum $p = 7$ TeV/c of the proton beams in the LHC tunnel with a curvature radius of $\rho = 2804$ m, a magnetic field of B

[T] = 3.336 × p [GeV/c] / ρ [m] = 8.3 T is required, which is achieved using the NbTi superconducting magnet technology, operating at the superfluid Helium temperature of 1.9 K. Along the straight sections of the LHC pipes, systems of quadrupole magnets are installed to stabilize the beams and focus them at the interaction points, thus minimizing their transverse size and achieving maximum luminosity.

Luminosity, together with beam energy, is the most important parameter for a collider. A colliding proton's high energy is essential to producing heavy particles. Luminosity, on the other hand, determines the production rate of interesting hard-scattering events; and maximizing it is equally important. For a given instantaneous luminosity $\mathcal{L}$, the production rate of a process with a cross section σ can be calculated as:

$$\frac{\mathrm{d}N}{\mathrm{d}t} = \sigma \times \mathcal{L}. \tag{3.1}$$

Luminosity at the interaction region of colliding beams can be calculated as:

$$\mathcal{L} = \frac{f_{rev} n_b N_b^2}{4\pi\sigma_x\sigma_y}, \tag{3.2}$$

where n_b is the number of bunches, N_b is the number of protons in each bunch (1.1 10^{11}), f_{rev} = 11.25 kHz is the revolution frequency, and σ_x and σ_y are the horizontal and vertical beam sizes at the interaction point.

Luminosity at the LHC is not constant during a physics run. It decays over time primarily due to proton-proton collisions at high-luminosity interaction points. The peak luminosities for different runs also change over time, depending on beam conditions. The evolution of the various parameters of the LHC during the 2011 data-collection run is presented in Table 3.2. The total number

Table 3.2: Evolution of peak LHC performance in 2011 [36].

Fill number	Date	Bunch space (ns)	Bunches	Peak L (10^{33} cm^{-1} s^{-1})	Number of protons per beam (10^{14})
1635	18 March 2011	75	32	0.03	0.04
1637	19 March 2011	75	64	0.06	0.07
1644	22 March 2011	75	136	0.17	0.16
1645	22 March 2011	75	200	0.25	0.24
1712	15 April 2011	50	228	0.24	0.29
1716	16 April 2011	50	336	0.35	0.42
1739	26 April 2011	50	480	0.51	0.58
1749	30 April 2011	50	624	0.72	0.76
1755	02 May 2011	50	768	0.83	0.93
1809	27 May 2011	50	912	1.10	1.15
1815	29 May 2011	50	1092	1.27	1.33
1901	27 June 2011	50	1236	1.25	1.64
2032	18 August 2011	50	1380	2.40	1.68

of events that a given process produces during a given period $t_1 - t_0$, however, depends only on an *integrated luminosity* L_{int} ($N = \sigma \times L_{int}$), calculated as

$$L_{int} = \int_{t_0}^{t_1} \mathcal{L}(\tau) \mathrm{d}\tau. \tag{3.3}$$

Four LHC experiments, installed at each of the four interaction points where the two beams intersect, detect the products of collisions and record a large variety of scattering events for subsequent analysis. Two multi-purpose detectors, CMS and ATLAS, are designed for high-luminosity proton-proton collisions ($L \sim 10^{34}$ cm^{-2} s^{-1}). LHCb is specifically designed for B-meson physics studies, requiring medium luminosities ($L \sim 10^{32}$ cm^{-2} s^{-1}) and ALICE is a dedicated experiment for ion collisions, operating with low luminosities ($L \sim 10^{29}$ cm^{-2} s^{-1}) of proton or heavy ion beams.

3.2 Compact Muon Solenoid

The CMS is a general-purpose detector, installed 100 meters underground [3, 37]. The overall layout of the CMS is shown in Fig. 3.2. At the core of the detector, a 13-meter long superconducting solenoid with a 6-meter inner-diameter provides a 3.8T magnetic field. The large bending power of this strong magnetic field is essential for an unambiguous determination of the muon charge for up to 1 TeV and precise measurement of muon momentum, yielding a dimuon mass resolution of about 1% at 100 GeV.

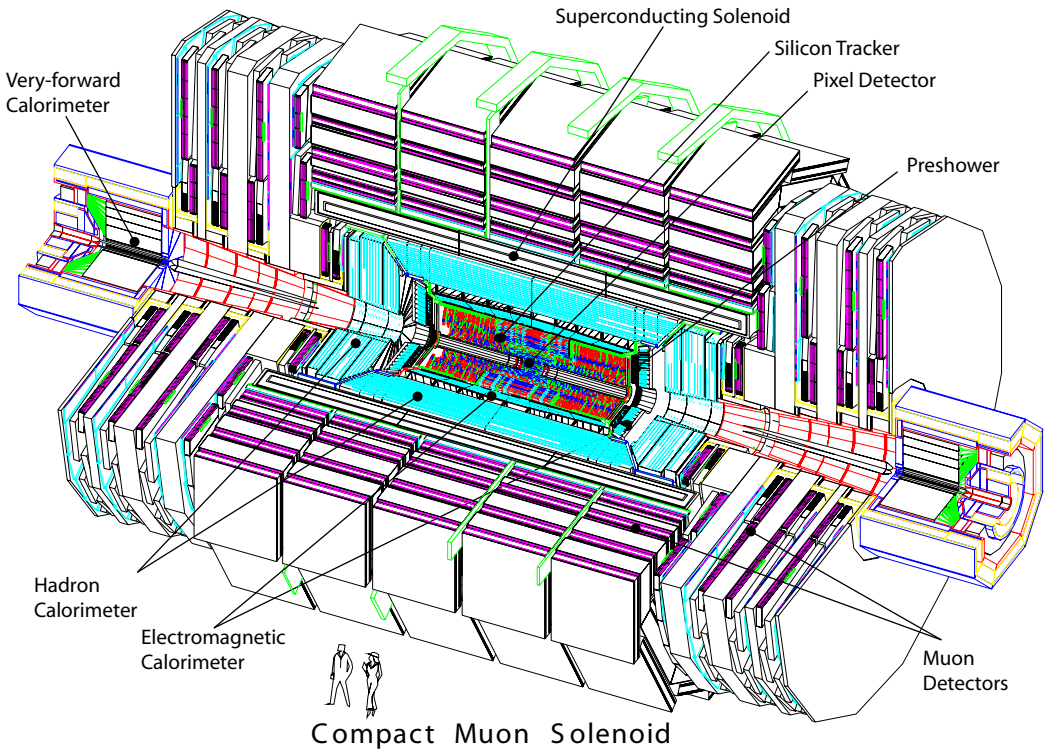

Figure 3.2: Layout of the CMS Detector [3].

The bore of the magnet coil accommodates the tracking system and the calorimeters. The tracking system consists of 10 layers of silicon microstrip de-

tectors, which provide high granularity and precision to deal with high track multiplicities, and 3 layers of silicon pixel detectors, which reside closest to the interaction point and are essential for precise determination of the impact parameter of charged particles and the position of secondary vertices.

The electromagnetic calorimeter (ECAL) uses lead tungstate ($PbWO_4$) crystals and covers the pseudorapidity region up to 3.0. A preshower detector is installed in front of the ECAL endcap to identify and reject neutral pions. ECAL provides good electromagnetic energy resolution, resulting in a $\sim 1\%$ level resolution in di-electron and di-photon mass at 100 GeV.

The hadronic calorimeter (HCAL) is crucial for the reconstruction of hadron jets and measuring the missing transverse energy. The central HCAL calorimeters, HCAL Barrel (HB) and HCAL Endcap (HE), surround the ECAL and cover the pseudorapidity region up to 3.0. The HB is complemented with outer HCAL (HO) which detects the hadronic tails that escape the central calorimetry. Forward HCAL (HF) calorimeter provides the pseudorapidity coverage up to 5.0.

The outermost part of the detector consists of the four stations of the muon systems, which, in addition to identifying muon tracks, significantly improve their momentum resolution at high momenta compared to the tracker measurement alone.

The distinguishing components of the CMS are the high-field solenoid, a full-silicon-based tracking system, and a homogeneous scintillating-crystals-based electromagnetic calorimeter. A large variety of physics processes can be effectively studied owing to the key features of the CMS detector, which can be summarized as follows.

- Excellent muon momentum resolution and identification over a wide range of its momenta and angles, as well as unambiguous determination of muon charge up to $p \sim 1$ TeV.
- Good charged particle momentum resolution and reconstruction efficiency in the tracker. Efficient $b-$tagging and τ reconstruction.
- Excellent electromagnetic energy resolution, efficient π^0 rejection, efficient photon and electron isolation at high luminosities.
- Good missing transverse energy and dijet mass resolution.

In the subsequent Sections we review the main characteristics of each subdetector and the online trigger system.

3.2.1 CMS tracking system

The tracking system of the CMS provides an accurate measurement of the trajectories of charged particles and a precise reconstruction of secondary vertices. The tracking system is located closest to the interaction point, has a length of 5.8 m and a diameter of 2.5 m. In order to efficiently deal with the thousands of charged particles from ~20 overlapping proton-proton interactions at design luminosity, high granularity and fast response is required. In addition, the intense particle flux causes severe radiation damage to the tracking system. To achieve the desired performance and an expected lifetime of 10 years under these harsh conditions, the tracker design is entirely based on silicon detector technology.

Figure 3.3 shows a schematic drawing of the CMS tracker. Three cylindrical layers of hybrid pixel detector modules surround the interaction point at a radii

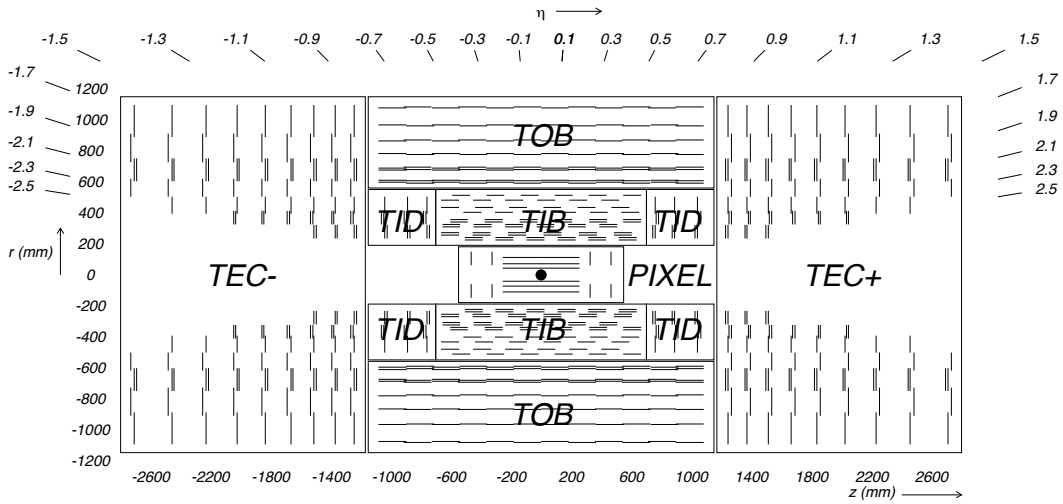

Figure 3.3: Layout of CMS Tracker [3].

of 4.4, 7.3, and 10.2 cm, delivering three high precision measurements of the track trajectory. The barrel layers are 53 cm in length and are complemented by two endcap disks of pixel modules on each side. The pixel detector covers an area of about 1 m^2 and has 66 million pixels. The pixel cells have a size of 100×150 μm^2, which provides similar track resolution in both $r-\phi$ and z directions. The spacial resolution of each measurement point is about 15−20 μm.

The silicon strip tracker occupies the radial region between 20 cm and 116 cm and consists of four different subsystems. Four cylindrical layers of the Tracker Inner Barrel (TIB) are complemented by three Tracker Inner Discks (TID) on each side, which extend up to 55 cm in radius. The inner tracking assembly is surrounded by six layers of the Tracker Outer Barrel (TOB), which extend up to 116 cm in radius and up to 118 cm along the z axis. The region between 124 cm $< |z| <$ 282 cm on each side of the detector is occupied by 9 disks of the Tracker Endcaps (TEC).

The strips of the silicon sensors are parallel to the beam axis in the TIB and TOB and are radial on the disks. The sensors have thicknesses of either 320 μm or 500 μm and a strip pitch ranging from 80 μm to 184 μm. The TIB and TID deliver up to 4 $r-\phi$ space points on a trajectory, the TOB provides another 6 $r-\phi$ measurements and the TEC provides 9 measurements in ϕ. In addition, the modules of the first two rings of TID and first two layers of TIB and TOB, as well as rings 1, 2 and 5 of TEC carry a second micro-strip detector which provides a second coordinate, z in the barrel and r in the endcaps.

Thus the overall tracker layout ensures at least 9 hits in the silicon strip tracker in the full range of $|\eta| < 2.4$, of which at least four are two-dimensional. The single point resolution ranges from ~20 μm to ~50 μm. The silicon strip tracker has a total of 9.3 million strips and 198 m^2 of active silicon area. The hit efficiency is above 99% in both the silicon pixel and the silicon strip detectors.

3.2.2 Electromagnetic calorimeter

The electromagnetic calorimeter of the CMS is a hermetic homogeneous calorimeter covering the pseudorapidity range $|\eta| < 3.0$. The ECAL crystals are made of lead tungstate ($PbWO_4$) which is characterized by a short radiation length (0.89 cm), small Moliere radius (2.2 cm), high density (8.28 g/cm^3), fast response, and high radiation resistance. These properties are essential to build a fast, compact, and granular calorimeter which can operate in the harsh radiation environment of the detector. The scintillation decay time of the crystals is of the same order as the LHC bunch crossing time, 80% of the light being emitted in 25 ns. The scintillation light is detected by silicon avalanche photodiodes in

the barrel region and vacuum phototriodes in the endcap regions.

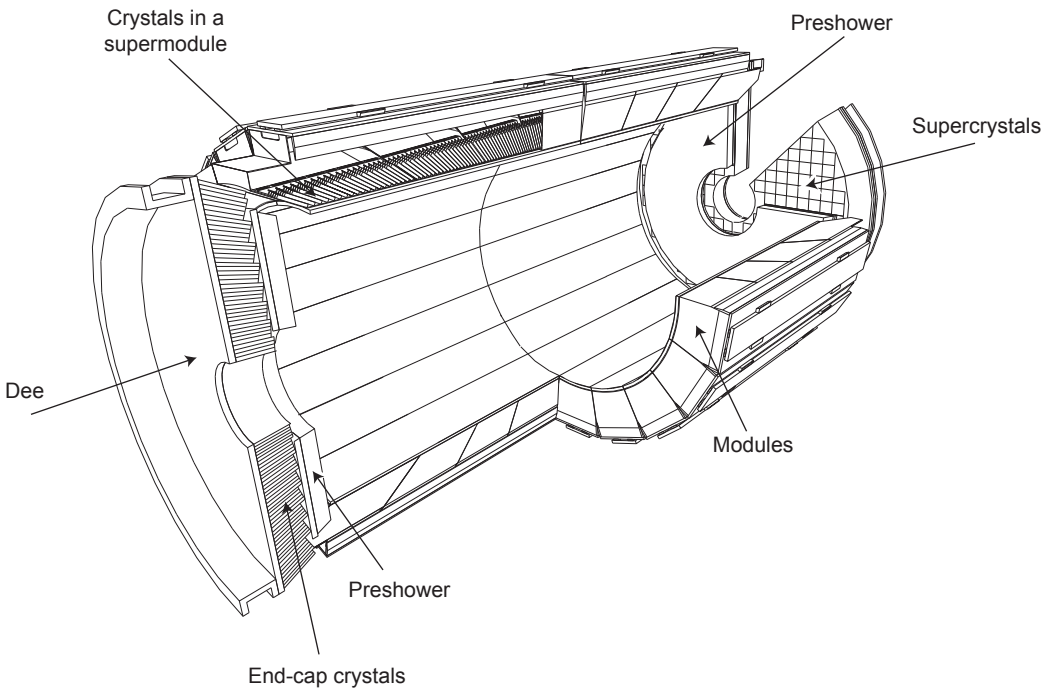

Figure 3.4: Layout of the CMS electromagnetic calorimeter [3].

The layout of the ECAL is shown in Fig. 3.4. The barrel part of the calorimeter (EB) covers the pseudorapidity range $|\eta| < 1.479$. Granularity of the EB is $360_{\phi} \times (2 \times 85)_{\eta}$, resulting in a total of 61,200 crystals. Each crystal has a front face of 22×22 mm^2, which corresponds to 0.0174×0.0174 in $\eta - \phi$; and a length of 230 mm, which corresponds to 25.8 units of radiation length. Each half of the EB is made of 18 *supermodules*, each covering 20° in ϕ. Each supermodule is composed of four *modules* (an assembly of 400 or 500 crystals) and contains a total of 1700 crystals.

The two endcap calorimeters (EE) provide a pseudorapidity coverage of $1.479 < |\eta| < 3.0$. Crystals in the EE are grouped in mechanical units of 5×5 crystals, called supercrystals. Each EE is divided into two halves, called *Dees*, each

containing a total of 3662 crystals. Each crystal has a front face of 29×29 mm^2 and a length of 220 mm, which corresponds to 24.7 units of radiation length.

The Preshower detectors (ES) are located in front of the EE and cover a pseudorapidity range $1.65 < |\eta| < 2.60$. Each detector is a sampling calorimeter made of two sets of lead absorber and silicon strip sensor layers. The material thickness of the lead is 2 X_0 in the first layer and 1 X_0 in the second layer. Each silicon sensor has an active area of 61×61 mm^2 and is divided into 32 strips of 1.9 mm pitch. The primary purpose of the ES is to identify neutral pions. Effective π^0 identification is achieved with the high granularity of the ES, which is able to separate two spatially close photons from the π^0 decay. Due to its high granularity, the ES also improves the position measurement of electrons and photons.

3.2.3 Hadron calorimeters

Hadron calorimeters are important for the reconstruction of hadronic jets and missing transverse energy. Figure 3.5 shows the layout of the CMS Hadron calorimeter. The barrel (HB) and endcap (HE) regions are located between the electromagnetic calorimeter and the magnet coil, which limits the total amount of material that absorbs the hadronic shower. Therefore, the outer hadron calorimeter (HO) is installed outside the solenoid complementing the HB.

The HB covers the pseudorapidity range $|\eta| < 1.3$. Each half of the HB consists of 18 azimuthal wedges, each covering 20° in ϕ. The wedges are constructed out of flat brass absorber plates aligned parallel to the beam axis. The absorber consists of a 40-mm-thick front steel plate, followed by eight 50.5-mm-thick and six 56.5-mm-thick brass plates, and a 75-mm-thick steel back plates.

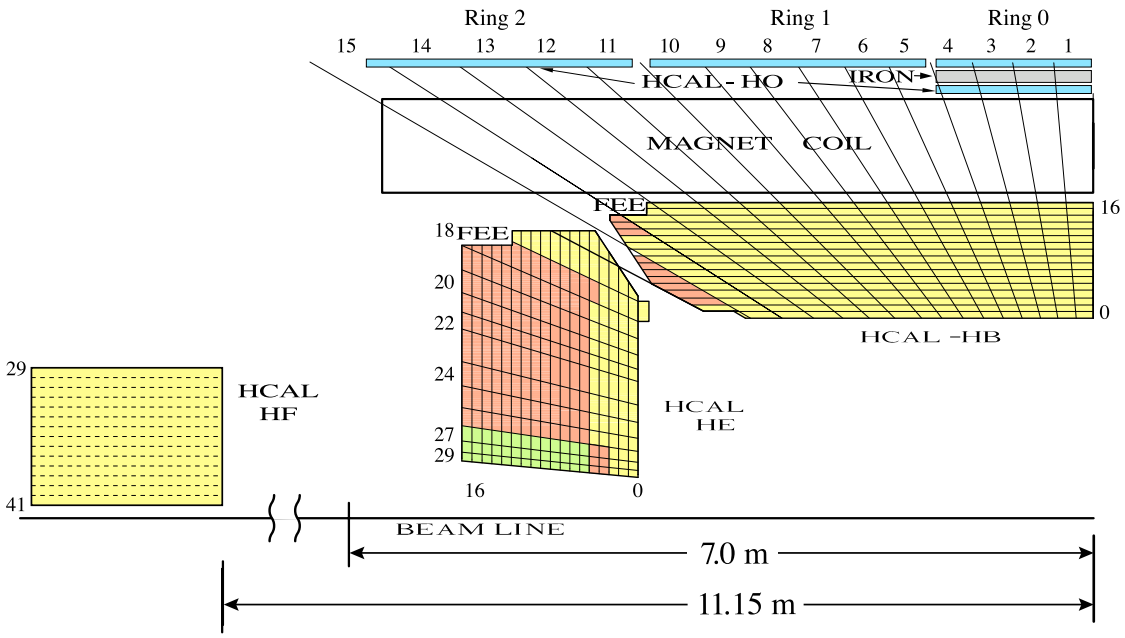

Figure 3.5: Layout of the CMS hadronic calorimeter [38].

The innermost and outermost steel plates are for structural strength. The total absorber thickness at the central angle is 5.8 interaction lengths, increasing with the polar angle to about 10.6 interaction lengths at $\eta = 1.3$. The HB active material consists of 15 3.7-mm-thick SCSN81 plastic scintillator layers, chosen for its long-term stability and moderate radiation hardness. In addition, the first 9-mm-thick layer of Bicron BC408 scintillator is located in front of the steel support plate to sample hadronic showers developing between the EB and HB. The last layer is also relatively thick, 9 mm, and serves to correct for late developing showers leaking out of the back of the HB. The scintillation light is converted by wavelength-shifting fibers and detected by hybrid photodiodes that can provide gain and can operate in high magnetic fields.

The HCAL endcaps (HE) cover the pseudorapidity region between 1.3 and 3. Since the HE is inserted into the end of a high magnetic field the absorber

is made of a nonmagnetic C26000 cartridge material, which has, in addition, a small interaction length and good mechanical properties. The active scintillator materials in the HE are the same as those in the HB. The granularity of the HB and HE calorimeters is $(\Delta\eta, \Delta\phi) = (0.087, 0.087)$ for $|\eta| < 1.6$ and $(\Delta\eta, \Delta\phi) = (0.17, 0.17)$ for $|\eta| > 1.6$.

The forward hadronic calorimeter (HF) is placed at 11.2 m from the interaction point and covers the pseudorapidity region $3 < |\eta| < 5$. It uses quartz fibers as an active medium to effectively deal with the intense particle fluxes it experiences. The signal is generated when charged particles from a shower generate Cherenkov light. Therefore the calorimeter is mostly sensitive to the electromagnetic component of a shower. The absorber is made of 5-mm-thick grooved steel plates. The detector is functionally divided into two longitudinal segments. Half of the fibers run over the full depth of the absorber (10 interaction lengths), while the other half starts at a depth of 22 cm from the front of the detector. This arrangement facilitates discrimination of the showers generated by electrons and photons, which deposit a large fraction of their energy in the first 22 cm, from those generated by hadrons, which generate nearly equal signals in both segments on average.

3.2.4 Muon system

The muon system is a key component of the CMS detector. It provides, together with the tracking system, high quality muon identification and high precision momentum measurement over a wide range of the transverse momentum and full pseudorapidity coverage.

The layout of the muon system is shown in Fig. 3.6. The barrel part of the muon detector has a cylindrical form and covers the pseudorapidity region up to $|\eta| < 1.2$. For muon identification the system uses drift tube (DT) chambers, organized into four stations. Each of the first three stations contains 8 chambers that measure muon coordinates in the $r - \phi$ plane, and 4 chambers that provide a measurement in z direction. The fourth station provides the only two-dimensional $r - \phi$ measurement. Drift cells of each chamber are offset by a half-cell width with respect to their neighbors to eliminate dead spots and to measure time with excellent resolution.

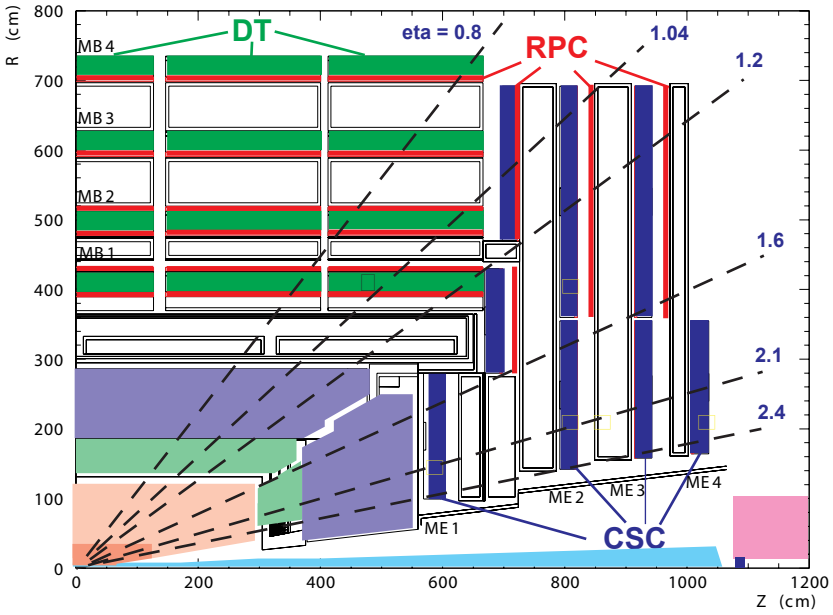

Figure 3.6: Layout of the CMS muon system [37].

In the endcap regions, where the background levels are high and the magnetic field is large and non-uniform, the muon system uses cathode strip chambers (CSC), characterized by their fast response time, fine segmentation, and radiation resistance. The endcaps cover the pseudorapidity region between 0.9 and 2.4 and are also organized into four stations with chambers positioned per-

pendicular to the beam line and interspersed between flux return plates. The cathode strips of each chamber run radially outward and provide a precision measurement in the $r-\phi$ plane. The anode wires run approximately perpendicular to the strips and provide measurements of η and the beam-crossing time of a muon. Each 6-layer CSC provides robust pattern recognition for rejection of backgrounds and efficient matching of hits to those in other stations and to the CMS inner tracker.

Due to multiple-scattering of muons in the detector material before they reach the first muon station, muon momentum resolution of the standalone muon system is about 9% for small values of η and for transverse momenta up to 200 GeV. At 1 TeV the standalone momentum resolution varies between 15% and 40%, depending on the pseudorapidity. A global muon fit, which also uses information from the inner tracker, improves the momentum resolution by an order of magnitude at low momenta and to about 5% at the 1 TeV scale.

The DT's and CSC's are complemented by a dedicated trigger system consisting of resistive plate chambers (RPC) which provide fast, independent and highly segmented triggers with a sharp p_T threshold covering the pseudorapidity range up to 1.6. RPC's produce fast response with good time resolution but coarser position precision compared to DT's and CSC's.

Finally, in order to optimize the muon momentum resolution, a complex alignment system measures the positions of the muon detectors with respect to each other and to the inner tracker.

3.2.5 Trigger system

With a beam crossing frequency of 40 MHz and more than 20 interactions per bunch crossing at the design luminosity, the LHC provides unprecedented interaction rates of 10^9 interactions per second. Since it is impossible to store and process all events, a trigger system is deployed, which reduces the event rate by six orders of magnitude in two steps: the Level-1 (L1) trigger and the High-Level Trigger (HLT). The Level-1 trigger consists of custom-designed, programmable electronics, whereas the HLT is a software system implemented in a filter farm of about one thousand commercial processors.

The L1 trigger has local, regional and global components and is based on the calorimetry and muon systems. The architecture is displayed in Fig. 3.7. The local triggers generate individual trigger primitives based on energy deposits in calorimeter trigger towers and hit patterns in muon chambers. The regional triggers combine their information and use pattern recognition logic to identify ranked and sorted trigger objects, such as electron and muon candidates. The global calorimeter and global muon triggers determine the highest-rank calorimeter and muon objects and transfer them to the global trigger, the top entity of the L1 hierarchy, which makes a decision whether to reject the event or accept it for further evaluation by a high level trigger. This decision is communicated to the sub-detectors through the Timing, Trigger and Control (TTC) system.

The L1 local muon trigger subsystems represent three muon detectors: the DT trigger in the barrel ($|\eta| < 1.2$), the CSC trigger in the endcap ($|\eta| > 1.2$) and the RPC trigger covering both regions ($|\eta| < 1.6$). Each of these trigger subsystems has its own trigger logic. The DT and CSC electronics first process the

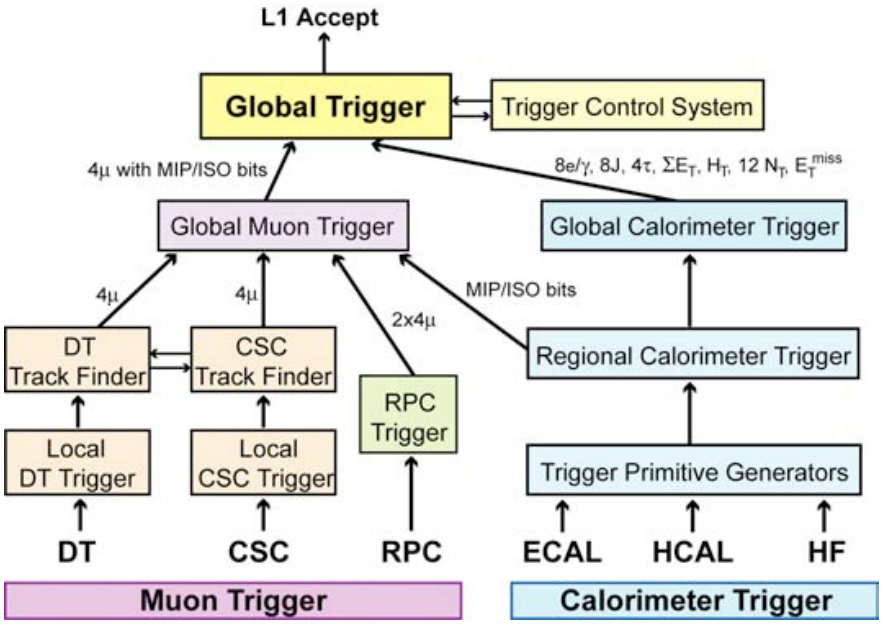

Figure 3.7: CMS Level-1 trigger architecture [3].

information from each chamber locally, delivering one trigger-primitive (track-segment) per muon per station, which includes the information on position, direction, bunch crossing, and quality.

The trigger primitives from all stations are sent to the regional Track Finder, which applies a pattern recognition algorithm to build the regional muon candidates. The three regional track-finders from each sub-detector rank the muon candidates; and up to the four DT, four CSC, and eight RPC candidates are then transferred to the Global Muon Trigger (GMT) for further analysis.

The GMT performs matching based on the proximity of the candidates in the $\eta - \phi$ plane. A selected ensemble of muons is sorted based on their quality, transverse momentum and the pseudorapidity and up to four best muon candidates are then transmitted to the Global Trigger, including ISO (isolation) and MIP (compatibility with a minimum ionizing particle in $\Delta\eta \times \Delta\phi = 0.35 \times 0.35$)

bits, based on the information received from the Global Calorimeter Trigger.

The Global Trigger is the final step in the CMS Level-1 architecture, which implements a pre-defined list (or "menu") of triggers based on the selection criteria, such as minimum transverse momentum or energy, for the final list of objects. The corresponding output L1 trigger objects will serve as seeds in further processing of events by the HLT.

The design output rate limit of the L1 trigger is 100 kHz. The latency between the bunch-crossing and the distribution of the trigger decision to the detector front-end electronics is 3.2 μs. During this time all high-resolution data are held in pipe-lined memories to be analyzed later by the more sophisticated algorithms of the HLT.

The purpose of the HLT is to reduce the output event rate down to about 100 Hz, selecting only the interesting events for saving in mass storage. At this point, the full granularity of the CMS detector is available and algorithms are similar to those in the offline reconstruction. In order to optimize the speed of the HLT reconstruction, the final trigger objects are normally reconstructed at several levels, to allow discarding events as early as possible before running more CPU consuming algorithms.

The total HLT rate gets contributions from many different individual trigger paths which are dedicated to reconstructing the types of individual particles or particle topologies that characterize the various SM or BSM processes. For each trigger path, there exist a number of configurations designed for different luminosity levels. Figure 3.8 shows the typical trigger rates for various trigger paths in one of the trigger configurations.

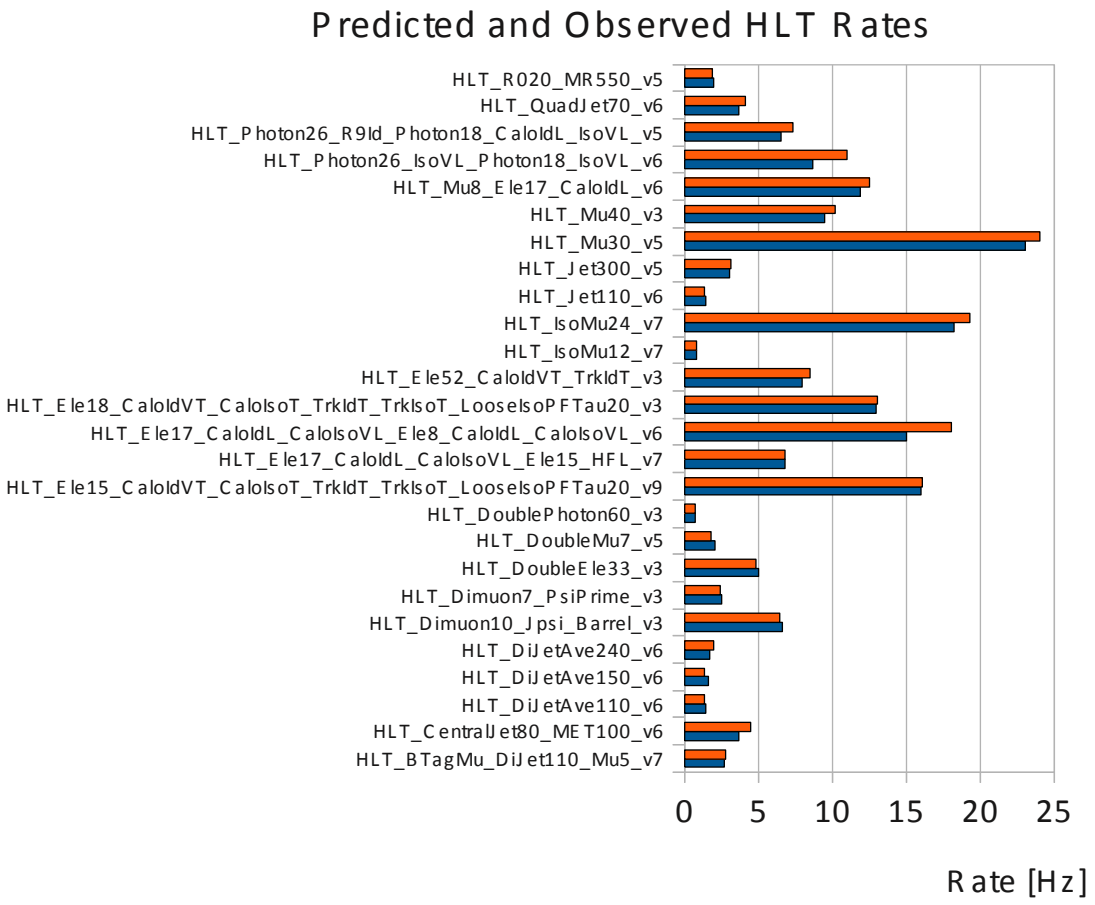

Figure 3.8: Typical predicted and observed rates of various HLT paths in one of the CMS HLT menu configurations in 2011 [39].

To keep the rate of events with a certain topology — say, with at least one muon in the output — at a manageable level, one can either put a high threshold on its transverse momentum or apply tighter quality criteria to the muons. For background studies, it is often required to have both low quality and small transverse momentum objects saved for later analysis. In such cases, to keep the rate low, the system saves only a fraction of the events passing the trigger selection. Such trigger paths are referred to as being *prescaled*. The prescale factor of 10, for example, means that only 1 event out of 10 is recorded for analysis. The

prescale factors of a given trigger path normally change in different versions, or within a single version depending on the current luminosity.

Each event can pass several HLT paths. Various HLT paths are grouped together to define a *primary dataset*, which combines all events that fire at least one of the triggers it contains. For example the *SingleMu* primary dataset, used in this analysis, is a unification of about 25 different HLT paths with different combinations of muon quality, transverse momentum and prescale factors (most of these paths are prescaled).

Events that fire at least one of the online trigger paths are then passed through the pre-defined streams for monitoring data quality and stored for further analysis.

CHAPTER 4

CMS EVENT RECONSTRUCTION

Particles, produced during the inelastic proton-proton scattering at the CMS interaction region, leave signals in different subsystems of the CMS detector. CMS event reconstruction algorithms use these signals to try to identify primary particles, evaluate their momenta, and determine the positions of interaction points. Some particles, e.g. muons, can be uniquely identified and their full momenta can be measured. Others are only characterized by their typical experimental signature, e.g. all charged particles are experimentally reconstructed as *tracks*; quarks and gluons are reconstructed as *jets* etc. Events that involve weakly interacting particles, such as neutrinos, that leave no trace in the detector are characterized by missing transverse energy — the total momentum imbalance of the reconstructed event in the transverse plane.

In this Chapter we review the reconstruction algorithms for objects which are relevant to our analysis. We start with reconstruction of *tracks*, i.e. measurement of the charge and the momentum of charged particles; and primary vertices, i.e. positions of interaction points. We then describe the reconstruction of muons based on the combined information from the inner tracker and the muon detectors. At the end we review the algorithm of Global Event Description, also called Particle Flow (PF), which uses full information from all the CMS sub-detectors in order to coherently reconstruct and identify all stable particles in the event. These particles, which we will refer to as PF-candidates, are then used to construct jets and missing transverse energy.

4.1 Tracks and vertices

Tracks in the CMS are produced by applying several iterations of the Combinatorial Track Finder (CTF) sequence [40]. During the first iterations, tracks with relatively high transverse momenta, originating from near the interaction point, are produced. After each iteration, detector hits associated with the previously reconstructed tracks are removed from the collection of tracker hits, and the remainder is used to reconstruct lower p_T and more displaced tracks in the subsequent iteration.

Each iteration proceeds in four steps: seed generation, track finding, track fitting, and track selection. In the first step, seeds are generated based on three hits in the pixel tracker (or two hits and the beam spot). These seeds provide the first estimate of the trajectory parameters and their uncertainties. The choice of the pixel detector for seed generation is driven by the detector's high granularity, which, regardless of its proximity to an interaction point, ensures a much lower average layer occupancy compared with the outer strip layers. In addition, pixel layers, as described in Section 3.2.1, provide accurate three-dimensional space point measurements, which allow better estimation of the track parameters.

The track-finding algorithm builds a track trajectory using the Kalman filter method [41]. The algorithm starts from the generated track seeds and adds hits from subsequent layers one by one. Each layer includes information on the location of the hit, its uncertainty, and the amount of material passed. When a compatible hit (according to the χ^2 test) is found in a tracker layer, it is included in the track and the track's trajectory parameters and uncertainties are updated. The search for compatible hits continues until the algorithm reaches the last

tracker layer.

Once the track-finding step is finished, the entire track fit is repeated to improve the trajectory. This time, non-uniformity of the magnetic field is taken into account. At the end, "smoothing" is performed by reverting the direction of extrapolation, i.e. starting with the outermost hits and progressing towards the beam spot.

At the end of each iteration, a set of quality criteria is applied to reject poorly reconstructed tracks. The selection criteria are based on the normalized χ^2 value of the trajectory fit, the number of tracker layers, and the impact parameter significance.

The momentum resolution of reconstructed tracks with p_T = 1 (100) GeV is about 0.7% (1.5%) in the central pseudorapidity region and degrades to about 2% (7%) at η = 2.4 (Fig. 4.1). For isolated muons up to 100 GeV, the tracking efficiency is over 99% across the entire tracker coverage, and has no dependence on the transverse momentum. For charged pions the tracking efficiency is lower, mainly due to nuclear interactions with the tracker material, but it is 80% or above, depending on the pseudorapidity. Tracking efficiency for charged pions also depends on their p_T's, since the cross section for nuclear interaction is higher for low-energy hadrons.

Reconstructed tracks are used to determine the locations of all proton-proton interaction vertices in the event. The vertex reconstruction proceeds in three steps [42]. First, from all track candidates, high-quality tracks are selected, based on each track's normalized χ^2, the number of hits on each track from the pixel and silicon strip detectors, and the significance of the track's trans-

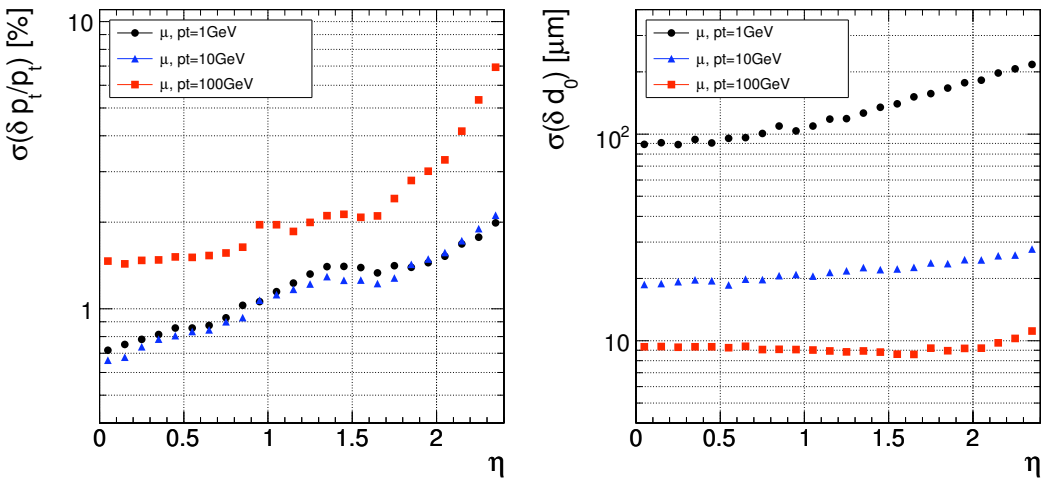

Figure 4.1: Transverse momentum (left) and transverse impact parameter (right) resolutions for single muons with p_T's of 1, 10 and 100 GeV [3].

verse impact parameter. Second, the selected tracks are clustered into groups, based on the z coordinates of their closest approach to the beam spot, to assign tracks within the same group to the same interaction vertex. Track clustering is performed using the deterministic annealing (DA) algorithm [43]. In the third step, the vertex location parameters are found with the adaptive vertex filter algorithm [44]. This algorithm also assigns a weight factor w to each track within a cluster, which determines the likelihood of the track belonging to its corresponding vertex. The sum of all track $w's$ of a given vertex is then used to evaluate the number of degrees of freedom of a vertex, $n_{\text{dof}} = 2 \times \sum_{k=1}^{n_{\text{tracks}}} w_k - 3$, which is one of the quality parameters of the reconstructed vertex. The collection of all vertices that pass the quality criteria are sorted based on the $\sum_{k=1}^{n_{\text{tracks}}} p_{T,k}^2$ and the first one is identified as the primary vertex of the hard interaction.

4.2 Muons

Reconstruction of muons relies on tracks reconstructed in the silicon tracker, as described in the previous Section, and *Standalone Muon* tracks, reconstructed using the muon system detectors alone [45]. The tracks in the muon system are reconstructed using the Kalman-filter technique, extrapolating from the innermost chambers out. The state of the track is propagated from one muon station to the next, taking into account the interaction of the muon with the material and the non-uniform magnetic field in the detector. Once the iteration reaches the outermost station, a reversed Kalman filter is then applied, propagating the trajectory towards the innermost muon station. At the end, the vertex-constrained fit is performed to extrapolate the track to the nominal interaction point.

Global Muons are reconstructed by extending the standalone muon tracks inwards to include the hits in the silicon strip and pixel tracker iteratively using the Kalman filter. At large transverse momenta, $p_T > 200$ GeV, the global muon fit significantly improves the momentum resolution, up to a factor of two, compared with the tracker-only fit.

Another approach to muon reconstruction is to extrapolate tracks reconstructed in the inner tracker outwards to include the hits in the muon system, taking into account the non-uniform magnetic field, muon energy losses and multiple scattering in the detector material. If at least one muon segment matches the extrapolated track, the corresponding track is referred as the *Tracker Muon*.

Tracker Muon reconstruction is more efficient than Global Muon reconstruction at low momenta, $p < 5$ GeV, since it requires only one segment in the

muon system. Most of the high momentum genuine muons, however, are reconstructed with both algorithms. Tracker Muons and Global Muons that share the same tracker track are combined into a single muon object, with the momentum determined from the tracker-only fit for lower transverse momentum muons (up to 200 GeV) or by the global fit, when both fits give a transverse momentum greater than 200 GeV.

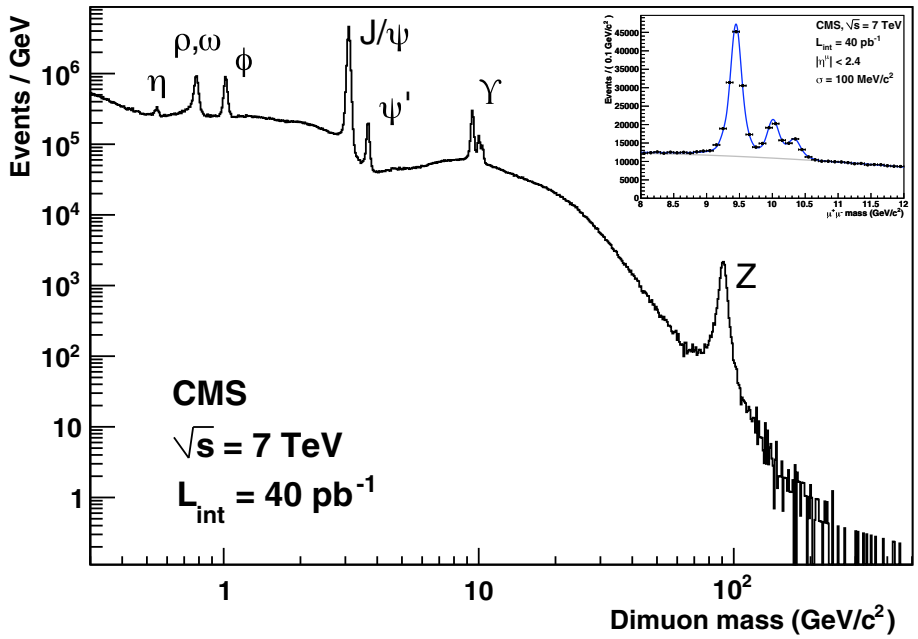

Figure 4.2: Invariant mass spectrum of dimuons in events collected with the loose double-muon trigger in 2010. The inset is a zoom of the 8-12 GeV region, showing the three $\Upsilon(nS)$ peaks, clearly resolved owing to a good mass resolution, about 100 MeV in the entire pseudorapidity range and 70 MeV when both muons are within the range $|\eta| < 1$ [45].

Figure 4.2 shows dimuon mass distribution in the events collected with the loose double-muon trigger in 2010, demonstrating excellent mass resolution over three orders of magnitude.

4.3 Global Event Description

The purpose of the Global Event Description is to reconstruct and identify all stable particles in the event [46]. The algorithm, called *Particle Flow*, combines the information from all CMS sub-detectors to reconstruct and identify muons, electrons, photons, charged hadrons, and neutral hadrons up to $|\eta| < 3$. It takes advantage of the high granularity and energy resolution of the CMS electromagnetic calorimeter and the high efficiency, low-fake rate, and excellent momentum resolution of the CMS tracker in a wide transverse momentum range. The reconstructed stable particles are then clustered into jets and are used to calculate an event's missing transverse momentum.

4.3.1 Particle Flow algorithm

The building blocks ("elements") of the Particle Flow algorithm are tracks from the inner tracker, calorimeter clusters, and tracks from the muon system. In order to achieve the high performance of the Particle Flow algorithm, reconstruction of genuine tracks at close to 100% efficiency is essential, which is achieved by applying an iterative tracking procedure.

The purposes of clustering energy deposits in calorimeter cells are 1) to measure the energy and direction of stable neutral particles, such as photons and neutral hadrons, 2) to separate energy deposits from neutral particles and charged hadrons, 3) to reconstruct and identify electrons with accompanying radiated photons, and 4) to help with the energy measurement of charged hadrons that have poorly reconstructed tracks. Thus, a specific clustering algorithm was

developed to achieve a high detection efficiency for low energy particles and an effective separation of energy deposits from spatially close particles. The clustering of calorimeter cells is performed separately in each sub-detector: EB, EE, ES, HB, and HE.

Since in general a given particle generates several particle flow elements, a linking algorithm is used to remove possible double counting across different detectors and also to combine the elements into particle flow blocks that will be used to reconstruct individual particles. A link between the tracker track and the muon system track is established if the corresponding global fit returns an acceptable χ^2. Tracks are linked to a given calorimeter cluster if the extrapolated trajectory falls within the cluster boundaries. Similarly, the clusters in two calorimeters, e.g. ECAL and HCAL, or PS and ECAL are linked if the position of the cluster in more granular calorimeter (ECAL or PS) is within the envelope of a less granular one (HCAL or ECAL).

After linking all the particle-flow elements to produce blocks, the PF algorithm reconstructs individual PF particles. First it produces PF-muons from all global muons with a combined momentum that is within three standard deviations of the tracker measurement. Then corresponding tracks are removed from the block and the expected energy deposit in the calorimeters is subtracted from the calorimeter clusters. PF electron candidates are reconstructed by applying the Gaussian-Sum Filter (GSF) [47] fit to the pre-identified, high-purity tracks and ECAL clusters. The algorithm takes into account the possible radiation of photons by the electrons in the tracker layers. The electron candidates are then identified by a number of tracking and calorimeter variables to produce the PF-electron objects. The corresponding ECAL clusters from the electron and from

the Bremsstrahlung photons are removed from the block for further analysis. Each of the remaining tracks gives rise to a PF-charged hadron, and the possible energy excesses in the ECAL and HCAL give rise to photons and neutral hadrons. The energy reconstruction of the neutral hadrons is improved with a dedicated calibration technique, which accounts for the non-linearity of the HCAL response to hadrons, as well as for the difference in the ECAL responses to hadrons and photons.

4.3.2 PF jets and $\not{E}_{\mathrm{T}}$

The PF algorithm describes the content of each physics event as a collection of different types of physics objects: PF muons, electrons, charged hadrons, photons and neutral hadrons, complemented with the electromagnetic and hadronic energy deposits in the forward calorimeter beyond $|\eta| = 3$. These objects are then used to reconstruct PF-jets by clustering them using the anti-kt algorithm [48] with a cone size of $R = 0.5$. Because the PF algorithm uses the full set of CMS detector information coherently when reconstructing individual PF-candidates, jets made from these PF-candidates perform better in terms of both response and resolution, when compared with ones based on energy deposits in the calorimetry, or on tracks reconstructed by the CMS tracking system.

The presence of weakly interacting particles in the event, such as neutrinos, introduces momentum imbalance in the transverse plane. The missing transverse momentum is defined as a negative vector sum of transverse momenta of all reconstructed PF-particles:

$$\vec{\not{E}}_T = -\sum_{PF-particles} \vec{p}_T \tag{4.1}$$

Missing Transverse Energy ($\not{E}_{\mathrm{T}}$), which is the magnitude of the above vector, is a powerful variable to identify events involving weakly interacting particles. As we describe in the next Chapter, in this analysis we use $\not{E}_{\mathrm{T}}$ distribution to extract the $W \to \mu\nu$ signal yield from the selected data sample of W candidates. $\not{E}_{\mathrm{T}}$ in $W \to \mu\nu$ events is introduced by the neutrino with a typical transverse momentum of ~40 GeV. The data sample will be contaminated with QCD multi-jet and $Z/\gamma^* \to \mu^+\mu^-$ events, which have either no, or small genuine $\not{E}_{\mathrm{T}}$. The measured non-zero values of $\not{E}_{\mathrm{T}}$ (~15 GeV in 2011) in these background events arise predominantly from the finite resolution effects. In the next Section we describe another variable, $\not{E}_{\mathrm{T}}$ significance, which provides a likelihood that the measured non-zero $\not{E}_{\mathrm{T}}$ in a given event can be attributed to the measurement resolutions.

As is the case with jets, $\not{E}_{\mathrm{T}}$, based on the PF algorithm (pf$\not{E}_{\mathrm{T}}$) has demonstrated superior performance in terms of both response and resolution as compared with $\not{E}_{\mathrm{T}}$ based solely on the calorimeter or the tracker information. Figure 4.3 shows the calibrated $\not{E}_{\mathrm{T}}$ resolution in multi-jet events for three $\not{E}_{\mathrm{T}}$ calculation algorithms originally developed in the CMS [1]. Calorimeter-based $\not{E}_{\mathrm{T}}$ (type2 calo$\not{E}_{\mathrm{T}}$) is a negative vector sum over the calorimeter deposits and momenta of reconstructed muons (taking into account the average energy deposit of muons in the calorimeters), corrected for the jet energy scale and the average unclustered energy response. Track-corrected $\not{E}_{\mathrm{T}}$ (tc$\not{E}_{\mathrm{T}}$) also starts from the calorimeter deposits and, in addition to the reconstructed muons, also corrects for well reconstructed tracks, taking into account the average energy deposits of

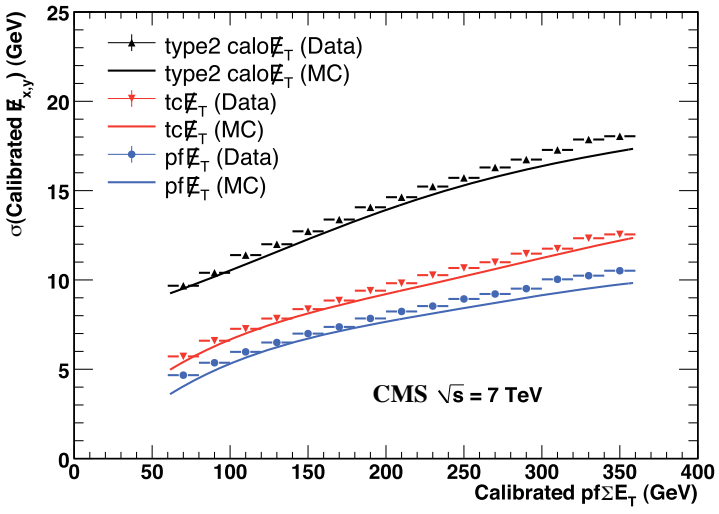

Figure 4.3: Calibrated $\not\!\!E_{X,Y}$ resolution versus calibrated pf$\sum E_T$ for Type2 calo$\not\!\!E_T$, tc$\not\!\!E_T$ and pf$\not\!\!E_T$ in multijet events for data and simulation [1].

charged π-mesons in the calorimeters. As one can see, pf$\not\!\!E_T$ outperforms other $\not\!\!E_T$ algorithms in terms of resolution.

4.4 $\not\!\!E_T$ Significance [1]

[1] A spurious nonzero $\vec{\not\!\!E}_T$ in an event can have contributions from many sources, including measurement resolution, reconstruction inefficiencies, instrumental defects, and improper pattern recognition. Events in which the reconstructed $\vec{\not\!\!E}_T$ is consistent with contributions solely from particle-measurement resolutions and efficiencies can be identified by evaluating the $\vec{\not\!\!E}_T$ significance, $\mathcal{S}$. The significance offers an event-by-event assessment of the likelihood that the observed $\not\!\!E_T$ is consistent with zero given the reconstructed content of the event

[1] $\not\!\!E_T$ significance section is a reproduction of the section previously published in [1]

and known measurement resolutions.

4.4.1 Definition

The significance requires evaluation of the uncertainty in the total measured transverse momentum, which is given by

$$\vec{E}_{\mathrm{T}}^{\,\mathrm{total}} = \sum_{i \in X} \vec{E}_{\mathrm{T}_i} = -\vec{\not{E}}_{\mathrm{T}}, \tag{4.2}$$

where $\vec{E}_{\mathrm{T}_i} = (E_{x_i}, E_{y_i})$ is the measured transverse momentum of the i^{th} reconstructed object. X is the set of reconstructed objects, such as calorimeter towers (for Calo $\not{E}_{\mathrm{T}}$) or PF particles (for PF $\not{E}_{\mathrm{T}}$), used to calculate $\not{E}_{\mathrm{T}}$. In the derivation of the significance, three quantities are relevant for each object in the sum. The first of these is $\vec{e}_{\mathrm{T}_i}$, the true transverse momentum of the object. Under the null hypothesis of zero genuine total transverse momentum, $\sum_{i \in X} \vec{e}_{\mathrm{T}_i} = 0$. The second is $\vec{E}_{\mathrm{T}_i}$, the measured transverse momentum of the object, which is distributed according to $P_i(\vec{E}_{\mathrm{T}_i} | \vec{e}_{\mathrm{T}_i})$, the probability density function (pdf) for observing the measured transverse momentum given the true transverse momentum of the object. The third is $\vec{\varepsilon}_i = \vec{E}_{\mathrm{T}_i} - \vec{e}_{\mathrm{T}_i}$. For convenience, we define an equivalent pdf in terms of this difference: $p_i(\vec{\varepsilon}_i | \vec{e}_{\mathrm{T}_i}) \equiv P_i(\vec{\varepsilon}_i + \vec{e}_{\mathrm{T}_i} | \vec{e}_{\mathrm{T}_i})$. Given the null hypothesis, $\sum \vec{E}_{\mathrm{T}_i} = \sum \vec{\varepsilon}_i$, so that the i^{th} reconstructed object contributes $\vec{\varepsilon}_i$ to the measured total transverse momentum.

We first introduce the likelihood that we would observe a total transverse momentum $\vec{\varepsilon}$ under our null hypothesis. For the two-object case, the likelihood

function is given by

$$\begin{aligned}\mathcal{L}(\vec{\varepsilon}) &= \int P_1(\vec{E}_{\mathrm{T}_1}|\vec{e}_{\mathrm{T}_1})P_2(\vec{E}_{\mathrm{T}_2}|\vec{e}_{\mathrm{T}_2})\delta(\vec{\varepsilon}-(\vec{E}_{\mathrm{T}_1}+\vec{E}_{\mathrm{T}_2}))\,d\vec{E}_{\mathrm{T}_1}\,d\vec{E}_{\mathrm{T}_2} \\ &= \int p_1(\vec{\varepsilon}_1|\vec{e}_{\mathrm{T}_1})p_2(\vec{\varepsilon}_2|\vec{e}_{\mathrm{T}_2})\delta(\vec{\varepsilon}-(\vec{\varepsilon}_1+\vec{e}_{\mathrm{T}_1}+\vec{\varepsilon}_2+\vec{e}_{\mathrm{T}_2}))\,d\vec{\varepsilon}_1\,d\vec{\varepsilon}_2 \\ &= \int p_1(\vec{\varepsilon}_1|\vec{e}_{\mathrm{T}_1})p_2(\vec{\varepsilon}_2|\vec{e}_{\mathrm{T}_2})\delta(\vec{\varepsilon}-(\vec{\varepsilon}_1+\vec{\varepsilon}_2))\,d\vec{\varepsilon}_1\,d\vec{\varepsilon}_2, \end{aligned} \tag{4.3}$$

since $0 = \sum_i \vec{e}_{\mathrm{T}_i} = \vec{e}_{\mathrm{T}_1} + \vec{e}_{\mathrm{T}_2}$. For an arbitrary number of input objects, the full likelihood function can be generated by a recursive application of Eq. (4.3). The significance is defined as the log-likelihood ratio

$$\mathcal{S} \equiv 2\ln\left(\frac{\mathcal{L}(\vec{\varepsilon}=\sum\vec{\varepsilon}_i)}{\mathcal{L}(\vec{\varepsilon}=0)}\right), \tag{4.4}$$

which compares the likelihood of measuring the total observed $\vec{E}_{\mathrm{T}}^{\,\mathrm{total}} = \sum \vec{E}_{\mathrm{T}_i} = \sum \vec{\varepsilon}_i$ to the likelihood of the null hypothesis, $\vec{E}_{\mathrm{T}}^{\,\mathrm{total}} = 0$.

This formulation is completely general and accommodates any probability distribution function. In practice, however, we often employ Gaussian uncertainties for measured quantities, for which the integrals of Eq. (4.3) can be done analytically. The Gaussian probability density function is given by

$$p_i(\vec{\varepsilon}_i|\vec{e}_{\mathrm{T}_i}) \sim \exp\left(-\frac{1}{2}(\vec{\varepsilon}_i)^{\dagger}\,\mathbf{V}_i^{-1}\,(\vec{\varepsilon}_i)\right),$$

where $\mathbf{V}_i$ is the 2×2 covariance matrix associated with the i^{th} measurement. The integration of Eq. (4.3) yields

$$\mathcal{L}(\vec{\varepsilon}) \sim \exp\left(-\frac{1}{2}(\vec{\varepsilon})^{\dagger}\,\mathbf{V}^{-1}\,(\vec{\varepsilon})\right)$$

with $\mathbf{V} = \mathbf{V}_1 + \mathbf{V}_2$. When many measurements contribute, the expression generalizes to

$$\mathcal{L}(\vec{\varepsilon}) \sim \exp\left(-\frac{1}{2}(\vec{\varepsilon})^{\dagger}\left(\sum_i \mathbf{V}_i\right)^{-1}(\vec{\varepsilon})\right). \tag{4.5}$$

The covariance matrix $\mathbf{U}_i$ for each reconstructed object in the $\vec{E}_{\mathrm{T}}$ sum is initially specified in a natural coordinate system having one axis aligned with the measured $\vec{E}_{\mathrm{T}_i}$ vector, $\vec{E}_{\mathrm{T}_i} \equiv (E_{\mathrm{T}_i} \cos\phi_i,\ E_{\mathrm{T}_i} \sin\phi_i)$:

$$\mathbf{U}_i = \begin{pmatrix} \sigma^2_{E_{\mathrm{T}_i}} & 0 \\ 0 & E^2_{\mathrm{T}_i}\,\sigma^2_{\phi_i} \end{pmatrix}. \tag{4.6}$$

This matrix is rotated into the standard CMS x-y reference frame to give the error matrix

$$\mathbf{V}_i = R(\phi_i)\mathbf{U}_i R^{-1}(\phi_i), \tag{4.7}$$

where $R(\phi_i)$ is the rotation matrix. The matrix summation is then performed in this common reference frame. Combining Eqs. (4.4), (4.5), and (4.7) yields

$$\mathcal{S} = \left(\sum_{i\in X} \vec{E}_{\mathrm{T}_i}\right)^{\dagger} \left(\sum_{i\in X} R(\phi_i)\mathbf{U}_i R^{-1}(\phi_i)\right)^{-1} \left(\sum_{i\in X} \vec{E}_{\mathrm{T}_i}\right). \tag{4.8}$$

Equation (4.8) makes explicit the dependence of $\mathcal{S}$ and $\vec{\not{E}}_{\mathrm{T}}$ on the set of objects X over which the vectors and matrices are summed. In general $\mathcal{S}$ is small when the $\not{E}_{\mathrm{T}}$ can be attributed to measurement resolution, and large otherwise.

In the Gaussian case, $\mathcal{S}$ is simply a χ^2 with two degrees of freedom. If we rotate into a coordinate system with the x axis parallel to the $\vec{\not{E}}_{\mathrm{T}}$ axis, instead of the CMS horizontal axis, then Eq. (4.8) is simplified to $\mathcal{S} = E^2_{\mathrm{T}}/(\sigma^2_{E_{\mathrm{T}}}(1-\rho^2))$, where $\sigma^2_{E_{\mathrm{T}}}$ is the variance of the magnitude of $\vec{\not{E}}_{\mathrm{T}}$, and ρ is the correlation coefficient between the variances parallel to and perpendicular to the measured $\vec{\not{E}}_{\mathrm{T}}$. This form emphasizes the essential meaning of $\mathcal{S}$, but obscures the important feature that, through its denominator, $\mathcal{S}$ embodies the full topological information in the event. Essential features such as the angles between the measured $\vec{\not{E}}_{\mathrm{T}}$ and the reconstructed objects in the event are embedded in the definition of the denominator. This form also makes apparent the relationship between the true significance (in the Gaussian limit) and the more naive measure $\Sigma = \not{E}_{\mathrm{T}}/\sqrt{\sum E_T}$.

The specialization to a Gaussian probability density function is less restrictive than it may appear, as any probability density function expressible as a linear combination of Gaussians is accommodated by the formalism presented here.

To apply Eq. (4.8) to PF $\not\!\!E_{\mathrm{T}}$ significance, we note that the Gaussian probability distribution function only accommodates measurement resolution. Using only reconstructed PF particles to determine the covariance matrix would neglect fluctuations in the measured PF particle content itself. These fluctuations arise from detection and reconstruction efficiencies, and provide a nonnegligible contribution to the PF $\not\!\!E_{\mathrm{T}}$ resolution. These fluctuations, however, also affect the PF jet resolutions. We can therefore substitute the PF jet resolutions for the combined measurement resolutions of the PF particles that have been clustered into jets. The sum of covariance matrices in Eq. (4.8) thus includes contributions from PF jets, PF particles that were not considered during jet finding (e.g. isolated leptons), and PF particles that are not clustered into any jet. This approach inherently takes into account the contributions both from measurement resolution and from fluctuations in the reconstructed particle content.

The covariance matrices $\mathbf{U}_i$ of Eq. (4.6) are obtained from the known response of each type of PF particle or jet as a function of p_{T} and η. The charged hadron and muon resolutions are obtained on a particle-by-particle basis from the error matrix from the final track fit, and the resolutions for electrons are those obtained from studies of data samples of known resonances such as neutral pions, Z bosons, etc. The jet and photon resolutions are from simulation. No input resolutions were tuned based on the behaviour of the significance distribution itself.

4.4.2 Performance of $\mathcal{S}_{\mathrm{PF}}$ in dijet events

Because $\mathcal{S}$ is χ^2 distributed, it should exhibit a flat probability of χ^2, $\mathcal{P}(\chi^2)$, for two degrees of freedom in an event sample that nominally has no genuine $\not\!\!E_{\mathrm{T}}$. (That is, $1-\mathcal{P}(\chi^2)$ is the standard cumulative distribution function of the χ^2 statistic for two degrees of freedom.) Dijet samples from pp collisions are dominated by such events.

We select dijet events by requiring at least two jets satisfying $|\eta| < 2.3$ and $p_{\mathrm{T}} > p_{\mathrm{T}}^{\mathrm{min}}$, with thresholds $p_{\mathrm{T}}^{\mathrm{min}}$ of 30 or 60 GeV. One of the jets above threshold must have been responsible for the event passing an HLT single-jet trigger. We use data collected with a 15 GeV trigger threshold for our 30 GeV dijet sample, and a 30 GeV trigger threshold for the 60 GeV dijet sample. (Because of different prescale factors applied to the two trigger streams, the 60 GeV dijet sample is not a direct subset of the 30 GeV sample.)

We compare the distributions of the PF significance, $\mathcal{S}_{\mathrm{PF}}$, as well as the corresponding $\mathcal{P}(\chi^2)$ distributions, in data and simulation in Fig. 4.4 for both values of the $p_{\mathrm{T}}^{\mathrm{min}}$ threshold. The significance distribution very closely follows a pure exponential, and the $\mathcal{P}(\chi^2)$ distribution is populated quite uniformly between zero and unity in both data and simulation. There is a small peak at zero in $\mathcal{P}(\chi^2)$; simulation (Fig. 4.4) indicates that about half of this peak results from genuine $\not\!\!E_{\mathrm{T}}$ in the event sample. This $\not\!\!E_{\mathrm{T}}$ arises from a combination of sources such as the semileptonic decays of heavy quarks and the η acceptance of the detector. The data and simulation distributions match well in the 30 GeV threshold sample. MC studies show that the remainder of the excess of low probability events after accounting for genuine $\not\!\!E_{\mathrm{T}}$ typically have at least one high-p_T jet whose response is in the non-Gaussian tail of the response function.

To probe the stability of the $\mathcal{S}_{\mathrm{PF}}$ behaviour, we have studied dijet samples with different p_T^{min} thresholds, which changes the relative contributions of different detector regions in the covariance matrix calculations. We find that, overall, the $\mathcal{S}_{\mathrm{PF}}$ distributions for the bulk of the data continue to exhibit near-ideal behaviour independent of threshold. As the 60 GeV sample shown here demonstrates, though, the higher threshold data does begin to develop a larger tail in the significance, and a correspondingly larger peak at zero in $\mathcal{P}(\chi^2)$, than we find in the simulation. The discrepancy between data and MC is below the 0.2% level. Visual examination of the events with low probability reveal that the discrepancy arises from a combination of events with a residual anomalous energy contamination and other events with a high-p_T jet with activity straddling the endcap (HE) and forward (HF) calorimetry, for which the non-Gaussian tails are not yet perfectly modeled.

For the $\mathcal{S}_{\mathrm{PF}}$ distributions shown here, the transition point for use of resolutions based on PF jets rather than resolutions from unclustered PF particles in the $\mathcal{S}_{\mathrm{PF}}$ calculation (Eq. (4.8)) occurs at a jet p_T of 3 GeV. The $\mathcal{S}_{\mathrm{PF}}$ distributions are insensitive to the variation of this transition point between jets and individual particles over the range of 1 to approximately 6 GeV. By 10 GeV, a slope in the $\mathcal{P}(\chi^2)$ distribution clearly appears, indicating that we no longer account sufficiently for contributions to the $\not\!\!E_{\mathrm{T}}$ resolution from fluctuations in the reconstructed particle content.

A powerful feature of the $\not\!\!E_{\mathrm{T}}$ significance is that its distribution is insensitive to pileup (for events with no genuine $\not\!\!E_{\mathrm{T}}$). As long as the correct resolutions are input, the significance should still have a purely exponential behaviour with a uniformly distributed $\mathcal{P}(\chi^2)$. In Fig. 4.4, no restrictions were made on the num-

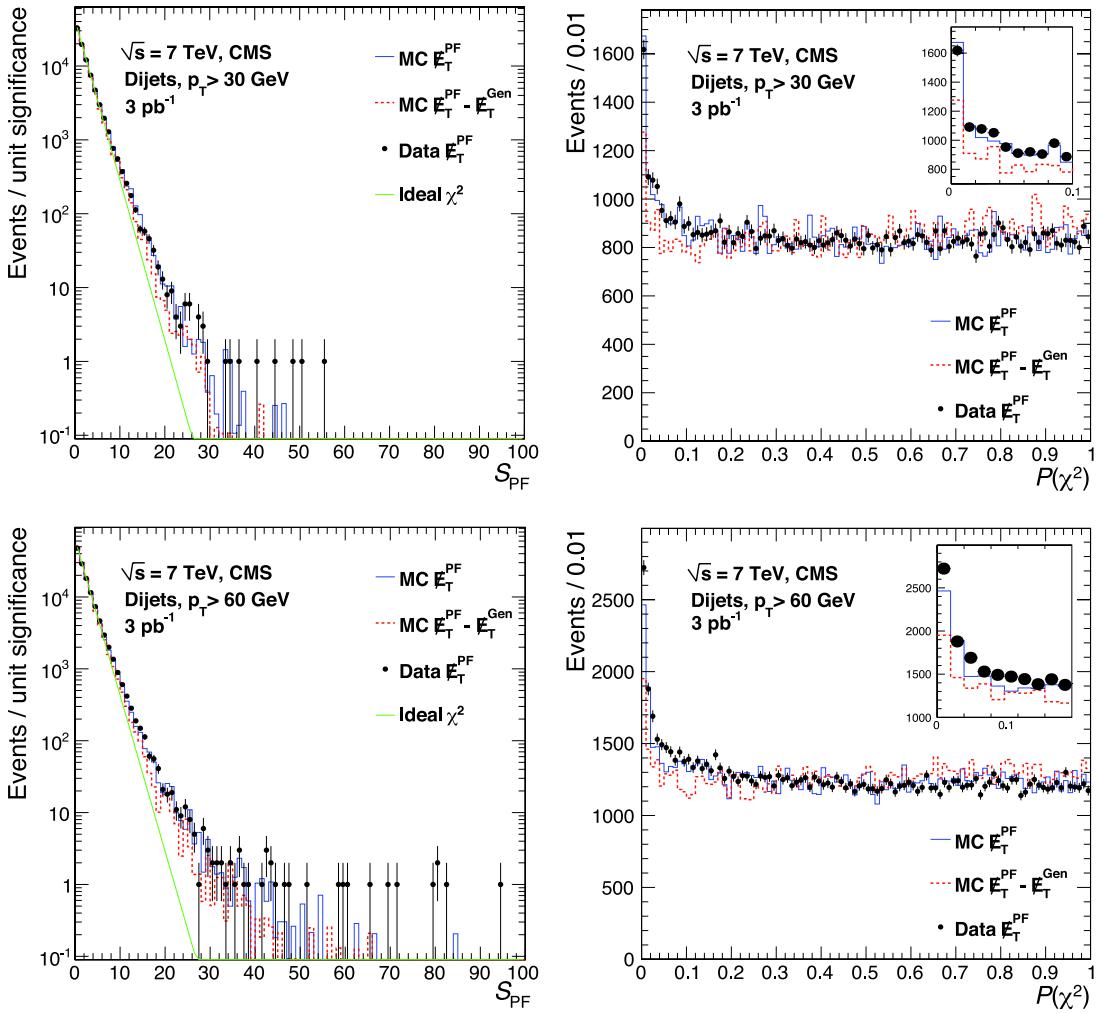

Figure 4.4: Distributions of the $\not\!\!E_{\mathrm{T}}$ significance $\mathcal{S}_{\mathrm{PF}}$ (left) and the corresponding probability of χ^2, $\mathcal{P}(\chi^2)$ (right), for dijet event samples in data (points) and simulation (solid histograms) with 30 GeV (top) and 60 GeV (bottom) jet p_T thresholds. The dashed histograms show the simulation distributions with true $\not\!\!E_{\mathrm{T}}$ contributions, from physics and acceptance effects, subtracted event-by-event. The dotted line overlaid on the $\mathcal{S}_{\mathrm{PF}}$ distributions shows a reference pure exponential function. Each inset expands the small $\mathcal{P}(\chi^2)$ region.

ber of interaction vertices in the data, while the simulation has no pileup. In Fig. 4.5, we compare the shapes of the single-vertex and multiple-vertex significance and $\mathcal{P}(\chi^2)$ distributions in data. The shapes are very similar, as expected. The main difference arises in the low probability region, where the multiple interaction data exhibits behaviour closer to the ideal—an example of the central limit theorem. With the additional contributions to the $\not\!\!E_{\mathrm{T}}$ resolution, the roles of the non-Gaussian response tails and genuine $\not\!\!E_{\mathrm{T}}$ are diminished. The overall insensitivity can be useful, for example, when extrapolating backgrounds dominated by samples with nominally zero genuine $\not\!\!E_{\mathrm{T}}$.

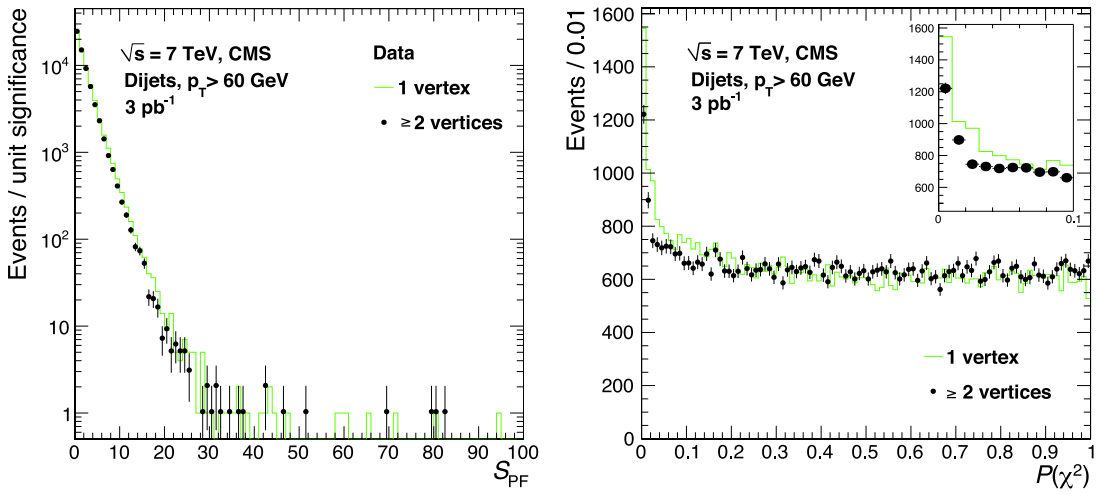

Figure 4.5: Distributions of the $\not\!\!E_{\mathrm{T}}$ significance (left) and $\mathcal{P}(\chi^2)$ (right) for events with a single interaction vertex (histogram) and multiple interaction vertices (points) in the 60 GeV threshold dijet sample. The inset expands the small $\mathcal{P}(\chi^2)$ region.

4.4.3 Application to $W \to e\nu$ events

As a case study, we examine the potential gain of introducing the significance variable into the selection criteria for $W \to e\nu$ analyses. The set of criteria em-

ployed is that of the recent measurement by the CMS Collaboration of the W cross section [49], for which backgrounds were reduced by means of a stringent, 80% efficient, electron isolation criterion. Signal and background yields in that analysis were determined by a fit to the reconstructed $\not\!\!E_{\mathrm{T}}$ distribution, though because of the large backgrounds at small values of $\not\!\!E_{\mathrm{T}}$, the signal level is largely determined from the $\not\!\!E_{\mathrm{T}} > 20$ GeV region.

One analysis option would be to relax the electron isolation from an 80% to a 95% efficient criterion and introduce $\not\!\!E_{\mathrm{T}}$ significance to help reduce backgrounds. Figure 4.6 compares the efficiency for signal versus background in simulation for increasing minimum thresholds on $\not\!\!E_{\mathrm{T}}$, with both the 80% and 95% electron isolation criteria applied; $\mathcal{S}_{\mathrm{PF}}$, again with both isolation criteria; and $\not\!\!E_{\mathrm{T}}/\sqrt{\sum E_{\mathrm{T}_i}}$ with the 95% isolation criterion. All efficiencies are measured relative to the signal or background yield obtained with the looser 95% electron isolation criterion applied. (As a result, the tighter 80% criterion has an asymptotic efficiency value of approximately 84%.) Application of the tighter criterion changes the relative signal and background distributions for $\not\!\!E_{\mathrm{T}}$ and $\not\!\!E_{\mathrm{T}}$ significance compared to the looser criterion. When a minimum $\not\!\!E_{\mathrm{T}}$ threshold is applied, the tighter isolation criterion provides a better signal to background ratio at low background levels than the looser criterion. Application of a minimum $\mathcal{S}_{\mathrm{PF}}$ threshold with the looser criterion, however, outperforms all the other combinations for background rejection at a given signal efficiency.

We note that in the calculation of the significance, the isolated signal electron candidate enters as an electron, and in particular with the resolution associated with an electron. This approach was found to outperform the option where each event was treated as electron-free (as is the case for the dominant background).

Figure 4.6 also shows that the $\mathcal{S}_{\mathrm{PF}}$ distributions for $W \to e\nu$ in data and simulation agree well. As expected, the backgrounds without genuine $\not\!\!E_{\mathrm{T}}$ are compressed towards low values of $\mathcal{S}_{\mathrm{PF}}$ while signal events having real $\not\!\!E_{\mathrm{T}}$ extend to high values of $\mathcal{S}_{\mathrm{PF}}$.

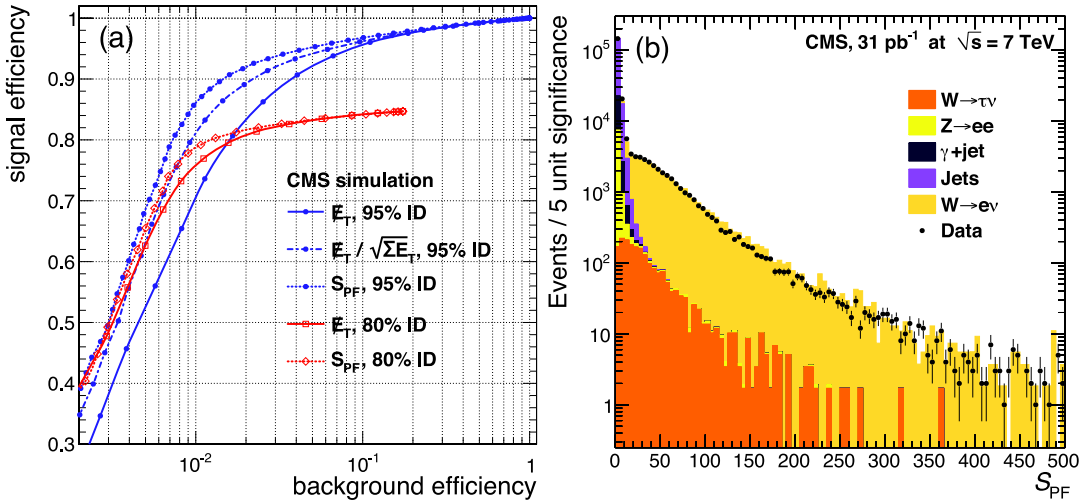

Figure 4.6: (left) Efficiency curves for $W \to e\nu$ signal versus backgrounds varying the minimum value of $\not\!\!E_{\mathrm{T}}$ (solid lines), of $\mathcal{S}_{\mathrm{PF}}$ (dotted lines), and of $\not\!\!E_{\mathrm{T}}/\sqrt{\sum E_{T_i}}$ (dot-dash line), with the 95% efficient (blue) or 80% efficient (red) electron isolation criterion applied. (right) Distributions of $\mathcal{S}_{\mathrm{PF}}$ in candidate $W \to e\nu$ events from data (points) and simulation (stacked histograms). The simulation components, from top to bottom, are signal (mustard) and backgrounds from jets (purple), γ+jets (black), $Z \to ee$ (yellow), and $W \to \tau\nu_\tau$ (orange). The simulation is scaled by a fit to the data with floating normalizations for the signal and the total background.

Figures 4.7 and 4.8 contrast the behaviour of signal and total background efficiencies for minimum $\not\!\!E_{\mathrm{T}}$ or $\mathcal{S}_{\mathrm{PF}}$ thresholds for different numbers of interaction vertices (pileup) in simulation. The jets and γ+jets backgrounds, which have no genuine $\not\!\!E_{\mathrm{T}}$, dominate. As pileup increases, the background contribution at higher $\not\!\!E_{\mathrm{T}}$ grows, while that at high $\mathcal{S}_{\mathrm{PF}}$ remains quite stable. As a result, a background subtraction based on extrapolation of $\not\!\!E_{\mathrm{T}}$ will be sensitive

to the modeling of pileup, while one based on extrapolation of $\mathcal{S}_{\mathrm{PF}}$ would not. As one can see from the signal versus background efficiency curves shown in Fig. 4.8, differentiation of signal from background degrades for both $\not\!\!E_{\mathrm{T}}$ and $\mathcal{S}_{\mathrm{PF}}$ as pileup increases. Regardless of the amount of pileup, however, $\mathcal{S}_{\mathrm{PF}}$ always provides a superior signal to background ratio compared to $\not\!\!E_{\mathrm{T}}$.

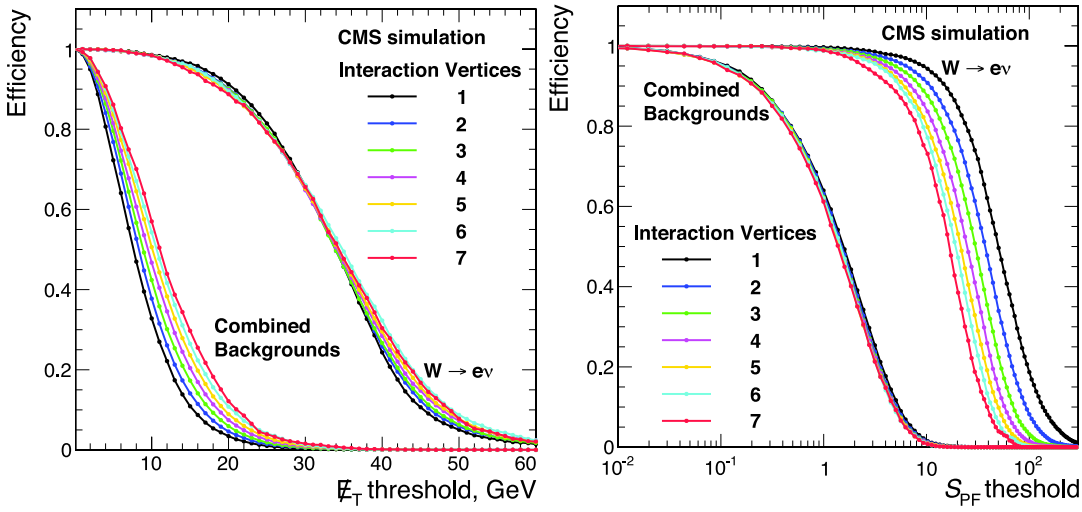

Figure 4.7: Efficiency versus minimum threshold curves for $W \rightarrow e\nu$ signal and for total background for different numbers of interaction vertices with a minimum applied $\not\!\!E_{\mathrm{T}}$ threshold (left) and a minimum applied $\mathcal{S}_{\mathrm{PF}}$ threshold (right).

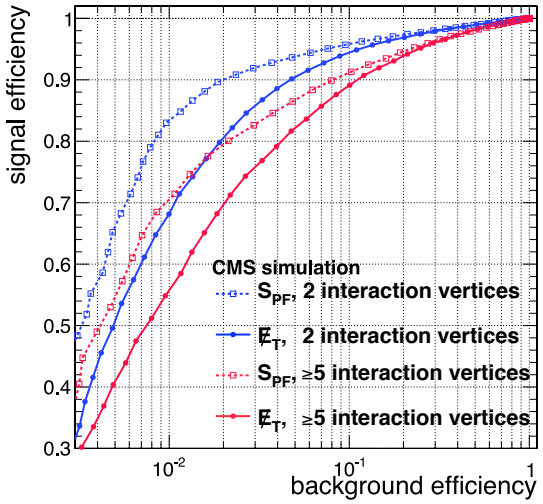

Figure 4.8: Efficiency curves for $W \to e\nu$ signal versus backgrounds, varying the minimum value of $\not\!\!E_T$ (solid lines) and of $\mathcal{S}_{PF}$ (dotted lines) for events with two interaction vertices (blue) or at least five interaction vertices (red).

CHAPTER 5

MEASUREMENT OF MUON CHARGE ASYMMETRY

In this Chapter we describe the measurement of muon charge asymmetry in inclusive $pp \to W + X \to \mu\nu + X$ production at $\sqrt{s} = 7$ TeV of colliding protons. The charge asymmetry is measured in 11 bins of absolute muon pseudorapidity $|\eta|$:

$$
\begin{array}{llll}
[0.00, 0.20], & [0.20, 0.40], & [0.40, 0.60], & [0.60, 0.80], \\
[0.80, 1.00], & [1.00, 1.20], & [1.20, 1.40], & [1.40, 1.60], \\
[1.60, 1.85], & [1.85, 2.10], & [2.10, 2.40]. &
\end{array}
$$

The measurement phase-space is restricted to $p_T > 25$ GeV for the muon, limited by the trigger. As a cross-check analysis, we also perform the measurement with a $p_T > 35$ GeV requirement on the muon.

The data sample used in this analysis was collected by the CMS during its 2011 operation with proton-proton collisions. $W \to \mu\nu$ candidates were selected from an isolated single muon trigger stream by applying tight offline muon identification criteria to remove the background events. A detailed review of the data and the Monte Carlo (MC) simulated samples, along with offline event selection criteria, is given in Section 5.1.

All the selected $W \to \mu\nu$ candidate events in data and simulated samples are divided into 11×2 sets based on the muon pseudorapidity and charge. In each pseudorapidity bin $W^{\pm} \to \mu^{\pm}\nu$ signal yields are extracted by fitting $\not{E}_{\mathrm{T}}$ distributions in data with the MC signal and background templates. Various corrections are applied to correct the $\not{E}_{\mathrm{T}}$ distribution in the data, the template shapes, and normalizations in the simulation. The extracted charge asymmetry in each

pseudorapidity bin is corrected at the end for different selection efficiencies of positive and negative muons. The details are described in Section 5.2.

Section 5.3 discusses the binned maximum likelihood fit technique with finite MC simulated templates, originally developed by Barlow and Beeston [50]. The method in our analysis is adjusted to the multinomial treatment of distributions in simulated templates. We then apply this technique in Section 5.4 to extract the $W^{\pm} \to \mu^{\pm}\nu$ signal and muon charge asymmetry in each pseudorapidity bin, followed by a detailed study of systematic uncertainties in Section 5.5.

At the end, in Section 5.6, we discuss the results of this analysis and their comparison with previous CMS lepton asymmetry measurements and with theoretical predictions. We also present the first PDF analysis of the impact of this measurement on HERA PDFs.

5.1 Analysis samples

In this Section we describe the data sample used in our analysis. We start with an overview of the CMS 2011 dataset and the online trigger, followed by a discussion of the backgrounds and offline event selection. We will then review the MC tools that were used to simulate signal and background events.

5.1.1 CMS 2011 Dataset

During the 7 months of the CMS's 2011 Run with proton-proton collisions, the LHC delivered data corresponding to an integrated luminosity of 6.13 fb^{-1}, of

which 5.55 fb^{-1} was recorded by the experiment. The small data loss is mainly due to malfunctioning of the data acquisition system or the misbehaviour of one or several detector subsystems. The evolution of LHC-delivered and CMS-recorded integrated luminosities during the 2011 operation is displayed in Fig. 5.1.

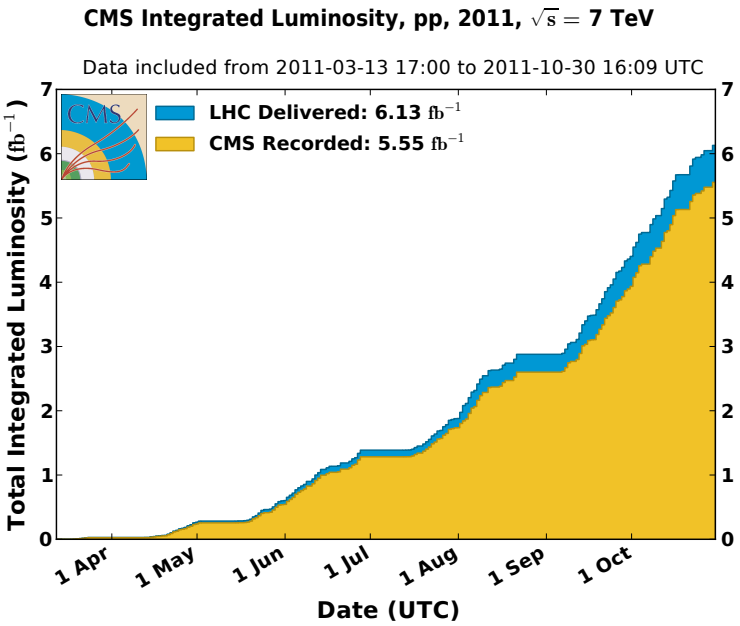

Figure 5.1: Evolution of LHC-delivered and CMS-recorded integrated luminosities during the 2011 data-collection [51].

The primary method of measuring luminosity [52] in the CMS is based on signals from the forward hadronic calorimeter. Two methods for extracting a signal in real time are used. The *zero counting* method, which is based on the average fraction of empty HF towers, determines the mean number of interactions per bunch-crossing. The $\sum E_T$ method exploits the linear relationship between the average transverse energy per tower and the luminosity. The two online algorithms agree within 5%.

Absolute luminosity calibration is performed with Van der Meer scans [53],

where the transverse offset of colliding beams is varied to measure the profile of the detector response as a function of the offset and to determine the effective overlap area of the beams A_{eff}. The peak luminosity $\mathcal{L}_0$ can be then calculated as

$$\mathcal{L}_0 = \frac{N_1 N_2 f_{rev} n_b}{A_{eff}}, \tag{5.1}$$

where N_i is the bunch intensity in beam i, $f_{rev} = 11,246$ Hz is the LHC orbit frequency, and n_b is the number of colliding bunches. The luminosity calibration constant for a detector is determined using its count rate with fully overlapping beams and the corresponding luminosity calculated using the equation above. The measurement is further tuned with offline algorithms that take into account the non-linear detector response to the luminosity by looking at the average number of reconstructed vertices.

The CMS also uses a pixel detector to improve the offline luminosity measurement in each 23.3-s-long data-taking unit, called *luminosity section*. The pixel detector measures luminosity by counting the number of pixel clusters [54]. This algorithm takes advantage of the detector's fine granularity and good linear response to the luminosity. Here again, the calibration constant, or *pixel cross section*, is derived from the Van der Meer scans and this value is then used to infer the instantaneous luminosity in each luminosity section. The final relative uncertainty of the measured luminosity in the CMS 2011 dataset is 2.2%.

$W \to \mu\nu$ candidate events in this analysis are selected from the *SingleMu* primary dataset, which contains events that fire one of about 25 single muon triggers, each with different muon quality criteria, p_T threshold and prescale factors. First, the dataset was cleaned up to select only the luminosity sections where all CMS sub-detectors were performing well. This set of ("golden") luminosity sections is provided centrally by the dedicated CMS data-certification

team. We also discarded luminosity sections recorded towards the end of the 2011 data-collection, where a single isolated muon trigger, as will be discussed in the next Section, was prescaled. Thus in the end we have a data sample corresponding to an integrated luminosity of (4.66 ± 0.10) fb^{-1}.

The total proton-proton interaction cross section is dominated by soft inelastic scattering ("minimum-bias") events that leave a signal in the detector. Due to the large cross section, minimum-bias events contaminate the physics events under study. These soft interactions will be referred to as *pileup*. Given the per-bunch measured instantaneous luminosity $\mathcal{L}$ (corrected on average over each luminosity section with a pixel-detector-based algorithm) and the total inelastic cross section, measured by CMS $\sigma_{inelastic} = 68$ mb, one can calculate the average number of interactions per bunch crossing as:

$$\mu = \frac{\sigma_{inelastic} \times \mathcal{L}}{f_{rev}} \tag{5.2}$$

The distribution of the mean number of interactions during the 2011 dataset is shown in Fig. 5.2. Contributions from each half of the data-collection period are also displayed: *2011A*, which corresponds to total integrated luminosity of 2.3 fb^{-1} with an average pileup value of 6.4, and *2011B*, with an integrated luminosity of 2.4 fb^{-1} and an average pileup value of 11.4.

5.1.2 Noise cleaning

The events in the dataset are first filtered according to a standard set of noise cleaning criteria, provided centrally in CMS and used in most of the analyses. These filters have been developed to remove the events containing beam backgrounds and anomalous signals from the detectors.

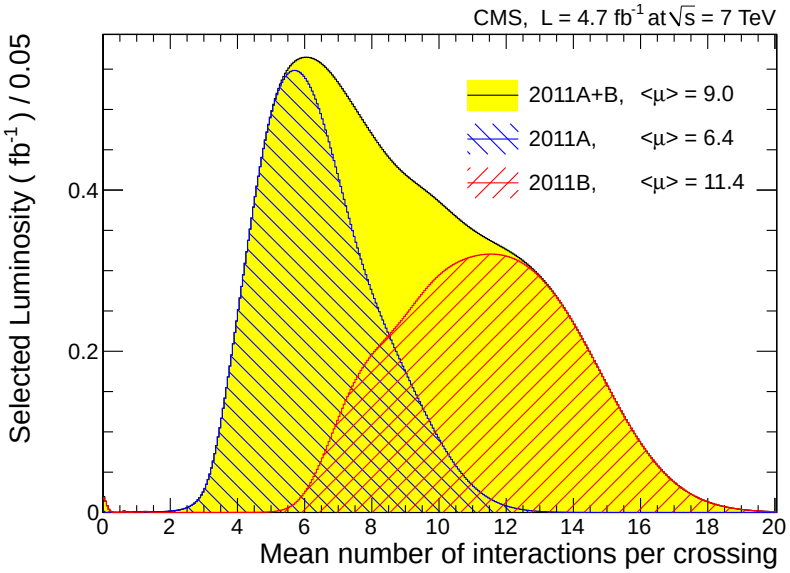

Figure 5.2: Distribution of mean number of interactions per bunch-crossing in CMS 2011 dataset used in this analysis. Contributions from each half of the data-collecting period, 2011A and 2011B, are also shown.

The beam background ("scraping") events produce high occupancy in the tracker detectors and result in the reconstruction of fake tracks. This background is removed by requiring that the fraction of high-purity tracks in the event is at least 25%. To make it into the dataset, an event must have one good primary vertex, with at least 4 degrees of freedom, as defined in Section 4.1, and transverse and longitudinal distance from the nominal collision point of less than 2 cm and 24 cm, respectively. At the end we apply an HCAL noise cleaning algorithm, which identifies and removes the events containing anomalous signals from the hybrid photodiodes and readout boxes.

The effect of the noise cleaning filters on the signal was investigated in the MC sample and was found to be negligible (~100% efficiency).

5.1.3 Isolated Single Muon Trigger

The inclusive W boson production cross section multiplied by its single leptonic decay branching ratio has been measured by the CMS to be $\sigma(pp \rightarrow W + X) \times BR(W \rightarrow l\nu) = (10.31 \pm 0.02_{stat.} \pm 0.09_{syst.} \pm 0.10_{theory} \pm 0.41_{lumi})$ nb [49]. So, a total of about 50 million $W \rightarrow \mu\nu$ events were produced in the pp collisions during the 2011 experiment at the CMS.

$W \rightarrow \mu\nu$ events with low muon transverse momentum are heavily contaminated by the QCD multijet background, where genuine muons are produced from the decay of heavy flavor hadrons (beauty or charmed) or from π's and K's decaying in flight. Fake *punch-through* muons can also be reconstructed from the tail of the hadronic shower that escapes the system of calorimetry. These QCD events are effectively suppressed by applying the transverse momentum cut and the set of identification and isolation criteria on the reconstructed muons both at online and offline selection levels.

In this analysis we use an isolated single muon trigger, *HLT_IsoMu24*, with a transverse momentum threshold of 24 GeV on the reconstructed muon. Online selection of muons in the HLT is performed in two steps. First, Level-2 (L2) standalone muons are reconstructed, using L1 muon candidates as seeds. The HLT trigger path is seeded by the *L1_SingleMu12(16)* muon trigger, with a transverse momentum threshold of 12 (16) GeV on L1 muon candidates. The standalone muon reconstruction, as described in the previous Chapter, uses only information from the muon system. Then the collection of L2-muons is filtered by the transverse momentum and quality requirements. A typical quality requirement is that the standalone muon reconstruction must involve at least two muon stations.

Additional calorimeter-based isolation is required at this point to further clean the muon collection. The isolation variable is calculated using the weighted sum of the energy deposits in the ECAL and HCAL within a certain $\Delta R < \Delta R_{max} = 0.24$ cone around the muon candidate, where $\Delta R = \sqrt{\Delta\phi^2 + \Delta\eta^2}$. The cone axis is defined by the muon direction at the vertex. The muon contribution to the isolation variable is removed by defining the vetoed region $\Delta R < \Delta R_{min}$ from the muon track position at the calorimeter, as shown in Fig. 5.3. The veto region is different for the ECAL and the HCAL. Typical values are $\Delta R_{min}^{HCAL} = 0.1$ and $\Delta R_{min}^{ECAL} = 0.07$. The weighted sum is calculated as $E_T = E_T^{HCAL} + \alpha E_T^{ECAL}$, with $\alpha = 1.5$, which reflects the better discriminating performance of the ECAL compared with the HCAL. Additional cuts against the noise are used at the level of contributing crystals and towers (0.2 GeV for ECAL, 0.5 GeV for HCAL). The threshold value for the isolation variable varies between 2 GeV and 4 GeV, depending on the muon pseudorapidity.

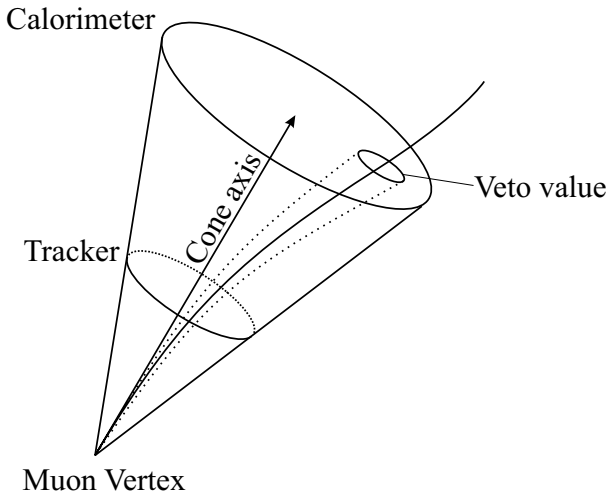

Figure 5.3: Schematic illustration of the muon isolation cone [37].

The muon selection at L2 reduces the rate enough to allow the Level-3 (L3) reconstruction to use the full set of tracker information. L3 reconstruction uses

L2 muon candidates as seeds and extrapolates them into the inner tracker by the global muon reconstruction algorithm, as described in Section 4.2. At this point, minimum transverse momentum requirement of 24 GeV and additional pixel-track based isolation is applied to further clean the L3 muon collection. The pixel track candidates are searched for only in the pixel detector by dedicated pixel-reconstruction software which is based on 3-hit tracks. It is optimized for speed but, due to the small number of hits, has poor momentum resolution and a limited track-finding efficiency of ~90%. The veto cone is defined by $\Delta R_{min} < 0.01$ and the isolation cone size is the same, $\Delta R_{max} = 0.24$. The threshold values depend on muon pseudorapidity and vary between 0.8 GeV and 1.1 GeV.

If at least one muon candidate survives the *HLT_IsoMu24* sequence up to this point, the event is accepted in this HLT path and the collection of filtered L3 muons is saved in the corresponding list of trigger objects. Due to the high luminosity of the colliding beams towards the end of the 2011 data collection, the *HLT_IsoMu24* was prescaled in order to maintain an acceptable trigger rate. In our analysis, the corresponding luminosity sections are discarded up-front.

Table 5.1 shows the single muon HLT configuration versions used in different physics runs during the 2011 data collection period, along with corresponding integrated luminosities.

5.1.4 Backgrounds and event selection

To remove background events containing fake and cosmic muons, and reduce the contamination by QCD multi-jet events containing genuine muons, a set of additional tight quality criteria, listed in Table 5.2, is applied to the recon-

Table 5.1: Dataset runs and isolated muon triggers with corresponding integrated luminosities.

Runs	HLT Path	L_{int} (fb^{-1})
2011A		2.31
160404 – 163261	HLT_IsoMu15_v5	0.047
163269 – 163869	HLT_IsoMu24_v2	0.169
165088 – 165633	HLT_IsoMu24_v4	0.142
165970 – 167043	HLT_IsoMu24_v5	0.560
166346	HLT_IsoMu24_v6	0.004
167078 – 167913	HLT_IsoMu24_v7	0.254
170249 – 173198	HLT_IsoMu24_v8	0.869
173236 – 173692	HLT_IsoMu24_v9	0.264
2011B		2.35
175832 – 178380	HLT_IsoMu24_v9	1.617
178420 – 179889	HLT_IsoMu24_v12	0.634
179959 – 180252	HLT_IsoMu24_v13	0.093
2011 Total		4.66

structed muons. First, the pseudorapidity coverage of offline muons is restricted to $|\eta| < 2.4$ to remove the poorly reconstructed muons near the edge of the tracker. We then require that the muons are reconstructed with both *Global* and *Tracker* muon reconstruction algorithms, as described in Section 4.2. A set of quality selections is applied to corresponding global and inner track candidates. At the end we require the muon track to be isolated.

$W \to \mu\nu$ candidate events then are selected as follows. First, the momentum of each muon in the cleaned collection is corrected for detector misalignment and mis-modeling of the magnetic field, and then the collection is sorted by decreasing corrected transverse momentum (p_T). This muon momentum correction is described in Section 5.2.1. Then the leading muon, with maximum p_T, is identified as the signal muon from the W decay, and a transverse momentum

Table 5.2: Offline muon identification and isolation criteria.

Description	Selection
Pseudorapidity coverage	• $\|\eta\| < 2.4$
Muon is reconstructed as a *Global Muon*, with a set of quality criteria applied to the corresponding global track.	• is Global Muon • normalized $\chi^2 < 10.0$ • valid hit in the muon chamber • segments in at least two stations
Muon is reconstructed as a *Tracker Muon*, with a set of quality criteria applied to the corresponding inner track.	• is Tracker Muon • at least one hit in the pixel detector • at least 8 tracker layers with hits • small transverse impact $\|d_{xy}\| < 0.2$
Offline relative tracker isolation	• $\sum_{\Delta R<0.3} p_T^{tracks}/p_T^{muon} < 0.1$

cut of $p_T > 25$ GeV is applied. To ensure that the offline signal muon was also reconstructed using the HLT algorithm, we require the closest trigger object in $\eta - \phi$ plane to be within the $\Delta R < 0.1$ cone around the muon. To reduce the background from Drell-Yan dimuon production, we veto the events that have a second identified muon with $p_T > 15$ GeV. The vetoed events are selected as a Drell-Yan control sample, which will be used to derive various corrections to $\not\!\!E_{\mathrm{T}}$ distribution in the data and in the MC simulation.

After all selections are made, the $W \to \mu\nu$ events remain contaminated with a background that contains a genuine muon with high p_T. The dominant processes contributing to the total background are:

- QCD multi-jet production, with genuine high-p_T muons from heavy flavor hadron decays. The QCD multi-jet background also gets a small contribution from π and K decays in flight. This is one of the dominant backgrounds and makes up 6–9% of all W candidates depending on the muon pseudorapidity bin.

- A Drell-Yan dimuon production, $pp \rightarrow Z/\gamma^* \rightarrow \mu^+\mu^-$, where one of the muons either falls outside the tracker fiducial region, has low p_T, or fails one of the identification or isolation criteria. This is also one of the dominant backgrounds, and its contribution ranges from 3% in the central region to 8% in high η bins.
- $W \rightarrow \tau\nu$ background, with the τ subsequently decaying into a muon, makes up about 3% of the total selected sample. This process has to be treated as background, since the asymmetry is measured as a function of muon η and the acceptance region is also defined by muon p_T.
- The contribution from other backgrounds is small, $\lesssim 1\%$. The main sources are $Z/\gamma^* \rightarrow \tau^+\tau^-$ decays, followed by τ(s) decaying into the muon(s), and $t\bar{t}$ production, followed by their semi-leptonic decays through Ws. The contribution from single-top and diboson production backgrounds was estimated and found to be negligible ($< 0.1\%$).

5.1.5 MC Simulated Datasets

In order to model the signal and electroweak background processes, a POWHEG [55] MC event generator is used, which is based on matrix element calculations in the next-to-leading order of QCD. It is interfaced with PYTHIA [56] which provides parton showering and hadronization. To properly take into account the spin-correlations in processes involving τ lepton decays, such as $W \rightarrow \tau\nu$ and $Z/\gamma^* \rightarrow \tau^+\tau^-$, the TAUOLA [57] package is used. The POWHEG-generated samples use a CT10 model for PDFs. The detector response to all generated particles is then simulated by a GIANT4 [58] package, and final events are produced using the same event reconstruction algorithms as were used on

the data.

QCD events are generated with PYTHIA; the CTEQ6l [59] PDF model is used to describe parton distributions. In order to avoid running a highly CPU-intensive detector simulation on all QCD generated events, a muon-enriched sample is produced by selecting only the events which contain a true $p_T > 15$ GeV muon.

Pileup is modeled by adding a certain number of simulated minimum-bias events to the hard-scatter event content, prior to running the final event-reconstriction. Two types of pileup are distinguished. *In-time* pileup refers to additional interactions in the same bunch-crossing as the main interaction. Soft particles, produced in these interactions contaminate the physics events under study. In addition, since the detector's response-time is of the same order as the bunch-spacing, hard-scatter events are also contaminated by late and early signal tails arriving from the soft interactions in previous and subsequent bunch crossings, respectively. This type of pileup will be called *out-of-time* pileup.

Table 5.3: Signal and background processes and Monte-Carlo tools used to produce them, along with the theoretical cross sections and effective integrated luminosities.

Process	Generator	Region	σ (pb)	L_{int}^{equiv} (fb^{-1})
$W^+ \to \mu\nu$	POWHEG	–	6152	3.1
$W^- \to \mu\nu$	POWHEG	–	4286	3.0
$W^+ \to \tau\nu$	POWHEG	–	6152	0.5
$W^- \to \tau\nu$	POWHEG	–	4286	0.7
$Z/\gamma^* \to \mu^+\mu-$	POWHEG	$M > 20$ GeV	1666	9.8
$Z/\gamma^* \to \mu^+\mu-$	POWHEG	10 GeV $< M <$ 20 GeV	3400	1.9
$Z/\gamma^* \to \tau^+\tau-$	POWHEG	$M > 20$ GeV	1666	7.8
$t\bar{t}$	POWHEG	–	158	6.1
QCD	PYTHIA	$p_T^\mu > 15$ GeV	79700	0.6

Table 5.3 shows a list of signal and background processes, along with the tools used to generate them. Signal and electroweak background cross sections are calculated at NNLO QCD with the FEWZ [28] package, while the $t\bar{t}$ cross section is evaluated at NLO QCD with the MCFM tool [60]. One should note that we will only rely on $t\bar{t}$ theoretical cross section in this analysis, since normalization of all other backgrounds will be assessed by data-driven techniques. The equivalent integrated luminosity is calculated as $L_{int}^{equiv} = N_{events}/\sigma$, where N_{events} is the number of generated events after matching the pileup distribution to data, as described in Section 5.2.3.

5.2 Corrections

In this Section we describe corrections we need to apply to the reconstructed muon momentum and $\vec{\not{E}}_T$, in order to prepare $\not{E}_{\mathrm{T}}$ templates in data and simulation. These templates will be used later for $W^{\pm} \to \mu^{\pm}\nu$ signal yield and charge asymmetry extraction. We will also review the measurement of muon selection efficiencies using the *Tag-and-Probe* method in $Z \to \mu^{+}\mu^{-}$ events and normalization of electroweak background templates.

5.2.1 Muon momentum scale correction

The momentum of the reconstructed muon critically depends on the correct alignment of the tracker system and the details of the magnetic field. However, after the alignment of the tracker detector, a residual misalignment remains that is not perfectly reproduced in the MC simulation. This misalignment leads to

a charge-dependent bias in the reconstruction of muon momenta, which is removed with a muon momentum correction. The detailed description of the method for extraction of the muon correction factors using $Z/\gamma^* \rightarrow \mu^+\mu^-$ events is given in reference [61].

First, corrections to muon momentum in bins of η and ϕ are extracted separately for positive and negative muons using the average values of the $1/p_T$ distributions of muons in $Z/\gamma^* \rightarrow \mu^+\mu^-$ events. The $1/p_T$ spectra at the MC generator-level, smeared by the reconstruction resolution, are used as "Reference" to which the reconstructed spectra in both data and MC simulation are tuned to match. Second, the correction factors derived in the previous step are tuned by comparing the dimuon invariant mass in each bin of muon charge Q and η to the "Reference". By comparing the correction factors for positively and negatively charged muons in each bin, we can determine relative corrections for misalignment and for uncertainties of the magnetic field in the tracker system. We found that the bias resulted predominantly from misalignment. The same procedure was performed for both the data and for the reconstructed MC events; correction factors were determined separately.

The average of the Z mass (mass profile) as a function of muon Q and η before and after the $1/p_T$ tuning is shown in Fig. 5.4. The Z mass profiles after the correction are compared to the reference mass profile for the data and for the reconstructed MC events, respectively. Z mass profiles agree well with the reference, so the muon momentum bias was largely removed. Note that the reference mass profile is expected to be a function of η because of the p_T cuts on the two daughter muons. Correction factors are extracted using the same η binning defined for the charge asymmetry analysis in order to avoid correlations

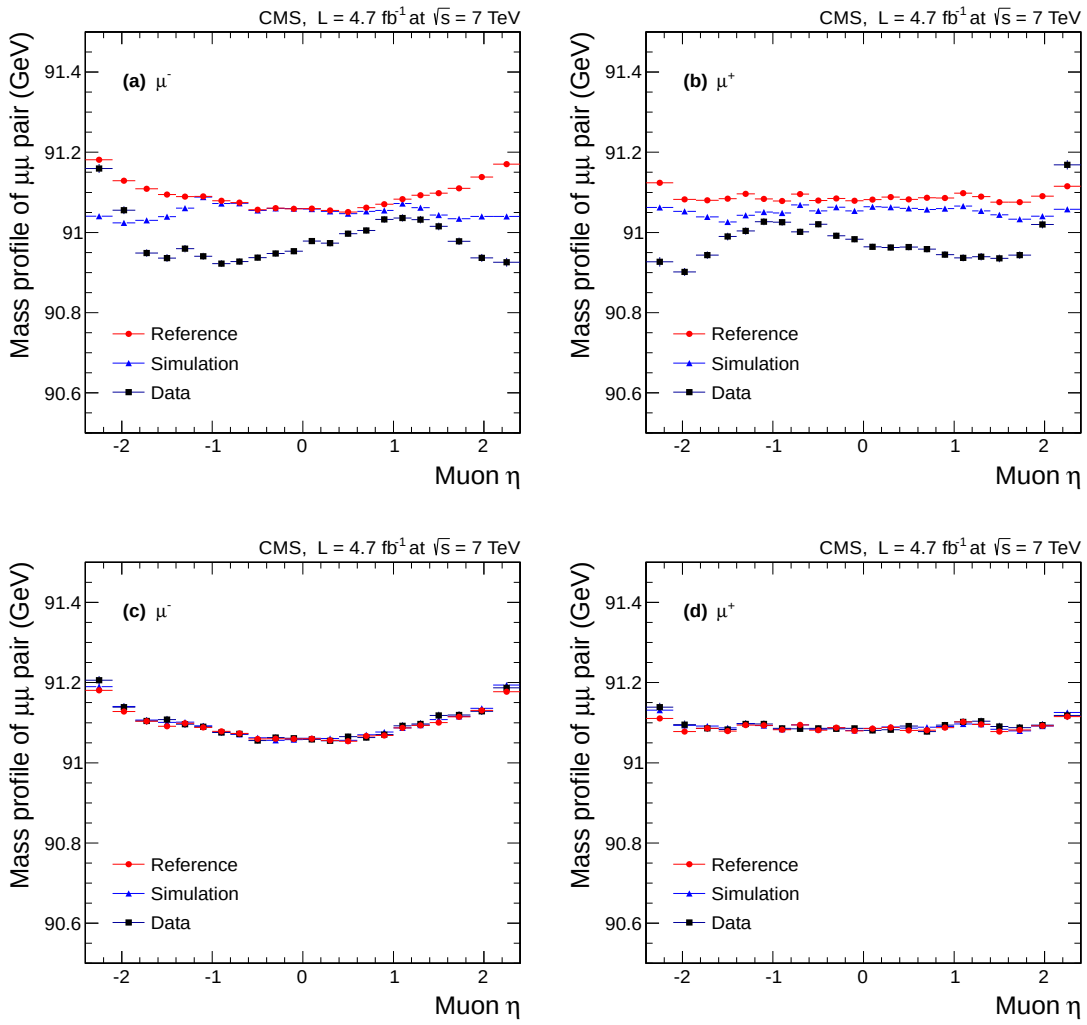

Figure 5.4: Dimuon mass profile before (top) and after (bottom) muon momentum correction.

between different η bins.

5.2.2 W and Z transverse momentum re-weighting

The POWHEG MC generator, used in this analysis to model all electroweak processes, does not accurately describe the transverse momentum distribution of

vector bosons in data. To improve the description we use weight-factors provided in the muon momentum correction package [61]. The weight factors are derived by comparing the p_T distribution in data and simulated $Z \to \mu^+\mu^-$ events. Several iterations are performed to unfold the weight factors to the generator level p_T^{gen}.

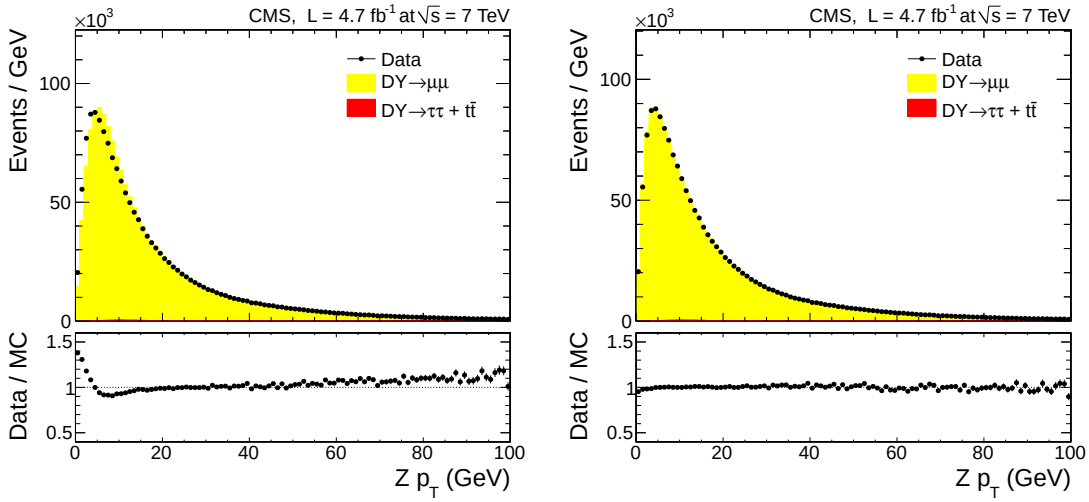

Figure 5.5: Comparison of boson p_T distributions between data and MC in Drell-Yan control region before (left) and after (right) weighting.

Figure 5.5 shows a comparison of the p_T distribution in data and simulated $Z \to \mu^+\mu^-$ events in our control region before and after applying $w = w(p_T^{gen})$ weight factors, showing that the weight-factors improve the description of the boson p_T. The mismodeling of the boson transverse momentum is primarly due to missing soft gluon radiation terms in the perturbation series, which should be similar in W and Z events. Therefore we also apply the same weight factors to our generated W events. Systematic uncertainty associated with this assumption will be discussed in Section 5.5.

5.2.3 Pileup re-weighting

MC samples in the CMS are normally produced centrally before the data-collection is finished. Therefore, the pileup distribution in simulation does not exactly match but roughly covers the expected luminosity conditions in data. To match the pileup distribution in data, all simulated samples are re-weighted event-by-event.

In this analysis we employ the *3D* pileup re-weighting technique. Based on the distribution of the mean number of interactions in data, shown in Fig. 5.2, and the distribution of the true number of interactions in simulation, triplet distributions of (N_{-1}, N_0, N_1) (early, in-time, and late pileup) are generated by randomly sampling the above distributions and generating the triplet of numbers with Poisson probability around this mean. The cumulative 3-dimensional distributions for data and simulation are then used to derive the MC weights, based on the triplet of early, in-time, and late pileup values in a given event.

We check the performance of the pileup re-weighting algorithm by looking at the distribution of the number of reconstructed primary vertices in the Drell-Yan control region. Figure 5.6 shows good agreement between the data and MC simulation.

For the MC simulation templates in the W fit, instead of weighting all events with the pileup 3D weights, discussed above, we filter them using an *accept-reject* technique based on the same weights. This is done to avoid a large spread of event weights, which degrades the Barlow-Beeston fit performance because it relies on the raw number of entries and average weights in MC template bins [1].

[1] If we performed the pileup re-weighting of all events, many events would end up having very small weights. Consequently, MC template bins would have many entries, which would

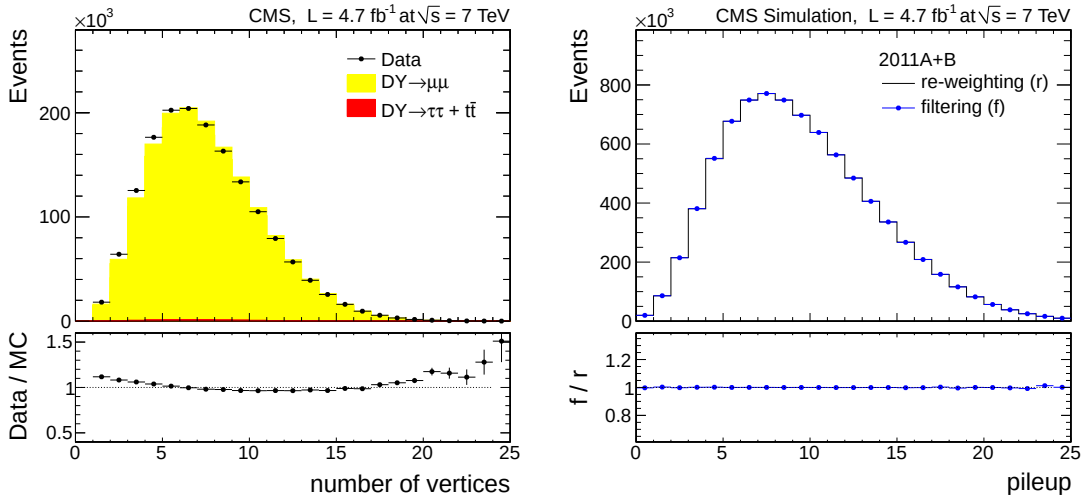

Figure 5.6: (left) Distribution of number of recontructed primary vertices in $Z/\gamma^* \rightarrow \mu^+\mu^-$ events in data (points) and simulation (histogram). (right) In-time pileup distribution in $W \rightarrow \mu\nu$ simulated events after re-weighting all events with pileup *3D* weights and the same distribution after filtering events based on the same weights.

In Fig. 5.6 (right) we verify that the two methods give the same in-time pileup distributions in the W signal MC sample. By filtering the events, we effectively lose an extra 10% of each sample in terms of the statistical uncertainties, compared to re-weighting.

5.2.4 Muon selection efficiency

Overall efficiency in the selection of muon candidates gets contributions from reconstruction, identification (including isolation), and trigger efficiencies. The

not contribute much to their contents, but would artificially make them more precise. As a result, BB fit would underestimate the uncertainties of floating parameters and overestimate the corresponding best-fit $\chi^2 = -2 \ln \mathcal{L}$ value.

muon reconstruction efficiency includes contributions from the reconstruction efficiency in the inner tracker system and in the outer muon system. The muon *offline efficiency* is the product of reconstruction and identification efficiencies. The contribution of each component to the overall efficiency (tracking, outer muon reconstruction, identification and trigger) is measured from the $Z/\gamma^* \rightarrow \mu^+\mu^-$ events using the *Tag-and-Probe* (T&P) method. In the T&P method, one of the daughter muons is used to tag the $Z/\gamma^* \rightarrow \mu^+\mu^-$ event and the other muon candidate is used as a probe to study the muon efficiencies as a function of charge Q, η and p_T. For every event a positively (negatively) charged muon is selected as the tag, which is required to satisfy all offline and trigger selection criteria; and a negatively (positively) charged probe candidate is used to study the efficiencies of negatively (positively) charged muons.

Each individual efficiency is determined for each charge Q of the muon in 22 η and 7 p_T bins. The same procedure is done for both data and MC simulation. The η binning is the same as one in our charge asymmetry analysis (but $+\eta$ and $-\eta$ bins are considered separately), and the p_T bins have the following boundaries (in GeV): 15, 20, 25, 30, 35, 40, 45, ∞. For the offline efficiency measurement, a binned likelihood fit is performed over the Z mass spectrum to estimate the signal and background yields in both *passed* and *failed* categories. The trigger efficiencies are measured by *counting* events in these two categories[2], which allows each η bin to be further divided into 2 or 3 bins to allow efficiency measurements in finer η bins.

Figure 5.2.4 shows example fits to $m_{\mu\mu}$ distributions in *passed* and *failed* categories which are used to determine the global muon reconstruction efficien-

[2]The tag-muon is always required to be matched with a trigger object. The two categories are based on whether or not the probe muon also has the corresponding reconstructed trigger object.

cies. The signal shape is modeled with a generator level dimuon mass spectrum convoluted with the Gaussian resolution function. The background is modeled with an exponential function.

Figure 5.8 summarizes muon "offline" and "trigger" efficiencies in data.

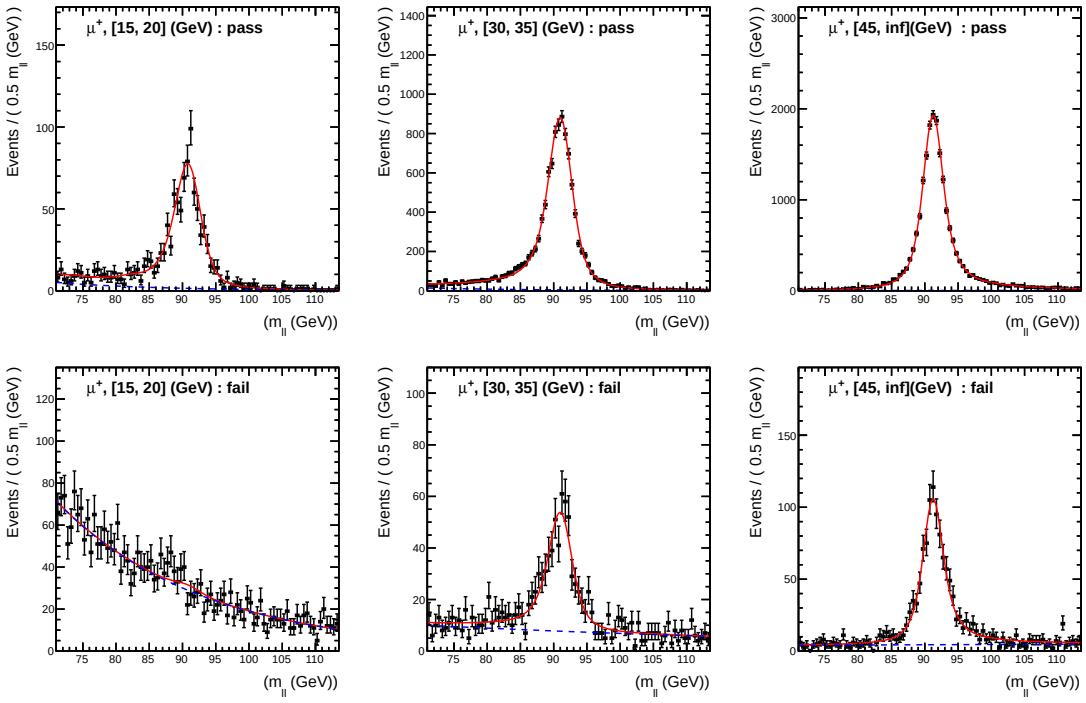

Figure 5.7: Example fits to the $m_{\mu\mu}$ distributions in *passed* and *failed* categories to determine the positive muon reconstruction efficiency in $0 < \eta < 0.2$ and three different p_T bins.

Muon selection efficiency affects the asymmetry measurement in two ways. First, all MC simulated samples, after having been normalized to theoretical cross sections, are corrected for the mismodeling of muon selection efficiency by weighting each event with $\epsilon_{data}(Q, p_T, \eta)/\epsilon_{mc}(Q, p_T, \eta)$. In addition, $Z/\gamma^* \to \mu^+\mu^-$ events are further corrected for the second muon efficiency both in the control region and the W signal region by $\epsilon^{offline}_{data}(Q, p_T, \eta)/\epsilon^{offline}_{mc}(Q, p_T, \eta)$

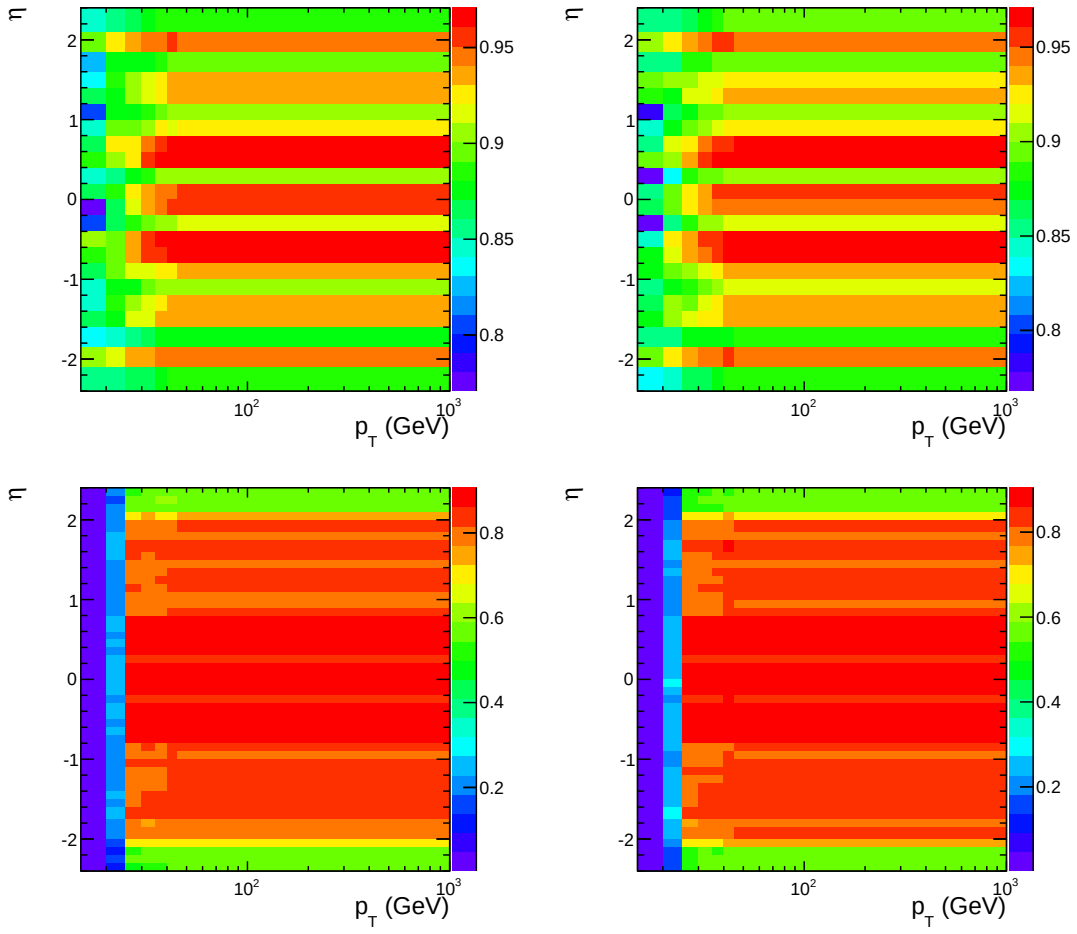

Figure 5.8: Offline (top) and trigger (bottom) selection efficiencies for μ^+ (left) and μ^- (right) in data as a function of muon p_T and η.

and $(1 - \epsilon_{data}^{offline}(Q, p_T, \eta))/(1 - \epsilon_{mc}^{offline}(Q, p_T, \eta))$, respectively. In the W signal region, only events where the second generated muon falls inside the acceptance region, $p_T > 25$ GeV and $|\eta| < 2.4$, are weighted and those Q, p_T and η values are used to evaluate the weight factors.

Because of the CMS detector's imperfect uniformity, both in terms of material distribution and alignment, it is possible to have different selection efficiencies for positive and negative muons. If this is the case, the observed charge

asymmetry in selected events will be biased and needs to be corrected. If the average selection efficiency of positive and negative muons is $\epsilon^{\pm}_{data}(\eta)$, then one can use the following equation,

$$A = \frac{A_0 - 0.5(1 - A_0)\delta}{1 + 0.5(1 - A_0)\delta} \approx A_0 - 0.5(1 - A_0^2)\delta, \tag{5.3}$$

where $\delta = \epsilon^{+}(\eta)/\epsilon^{-}(\eta) - 1$, to correct the observed asymmetry A_0 to the true value A in each pseudorapidity bin. Given the 2-dimensional $p_T - \eta$ efficiency tables, displayed in Fig. 5.8, we calculate the average data efficiency in each pseudorapidity bin with the selected signal MC events using

$$\epsilon^{Q}(\eta) = \frac{\sum w}{\sum w/\epsilon_{data}(Q, \eta, p_T)} = \frac{\sum \omega\epsilon_{data}(Q, \eta, p_T)/\epsilon_{mc}(Q, \eta, p_T)}{\sum \omega/\epsilon_{mc}(Q, \eta, p_T)}, \tag{5.4}$$

where $w = \omega\epsilon_{data}(Q, \eta, p_T)/\epsilon_{mc}(Q, \eta, p_T)$ includes all weight factors applied to W signal events, and ω is the remaining factor, which in the default scenario is the boson q_T weight.

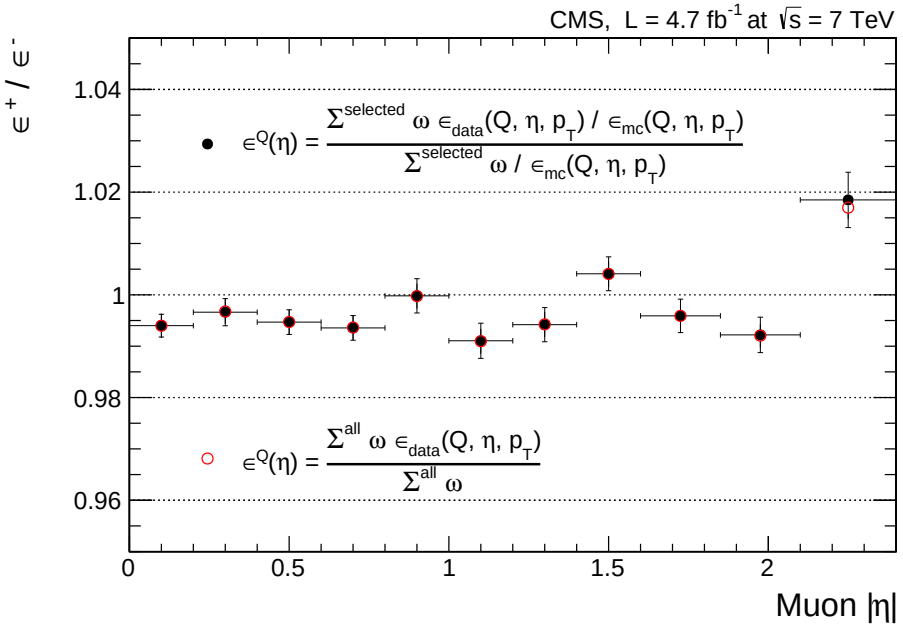

Figure 5.9: Ratio of positive and negative muon selection efficiencies.

The corresponding ϵ^+/ϵ^- values in 11 pseudorapidity bins are displayed in Fig. 5.9 as solid circles. One can see that this ratio deviates from unity in certain pseudorapidity bins. These deviations are primarily caused by the online trigger selection efficiency. As a cross-check we also calculate the average efficiencies by looping over all generated $W \to \mu\nu$ events with $p_T > 25$ GeV and calculating $\epsilon(Q,\eta) = \sum \omega\epsilon_{data}(Q,\eta,p_T)/\sum \omega$. As expected, the two methods yield consistent values for the ratio of positive and negative muon selection efficiencies.

5.2.5 Tuning of the Missing Transverse Energy

This Section describes the corrections that we must apply to the PF-$\vec{\not{E}}_T$ determination of the missing transverse momentum before we can use it in our analysis. There are three main corrections that we can derive from and test with our Drell-Yan control sample:

- correction for the muon $\vec{p}_T$ bias described in Section 5.2.1,
- correction for the $\phi(\vec{\not{E}}_T)$ modulation observed in both data and simulation,
- correction for the hadronic recoil response and resolution in simulation to match those in data.

Recoil definition

Recoil is defined as the vector sum of the transverse momenta of all PF candidates, excluding the identified muons. In the Drell-Yan control sample it can be

written as:

$$\vec{u} = -\vec{\not{E}}_T - \vec{q}_T, \tag{5.5}$$

where $\vec{q}_T$ is the transverse momentum of the dimuon system. In $W \to \mu\nu$ events it is defined as:

$$\vec{u} = -\vec{\not{E}}_T - \vec{p}_T^{\,\mu}. \tag{5.6}$$

We then define the parallel and perpendicular components of this vector relative to the boson direction as $u_\parallel$ and $u_\perp$, respectively. In order to define the boson q_T and direction, we use the reconstructed muon whenever possible. So, in the Drell-Yan control sample, we define the boson momentum as that of a reconstructed dimuon system. In simulated $W \to \mu\nu$ events we define it as $\vec{q}_W = \vec{p}_\mu^{\,reco} + \vec{p}_\nu^{\,gen}$, while in $W \to \tau\nu$ events we use the generated W momentum directly. The $Z/\gamma^* \to \mu^+\mu^-$ MC background events in the W-signal region are split into two categories based on the direction of the "missing" generated muon that failed the DY veto.

- If the "missing" generated muon falls within the tracker fiducial (failing some of the muon quality criteria, e.g. isolation), we define the recoil and recoil axes as in the Drell-Yan control sample, using the generated muon instead of the reconstructed one.
- When the "missing" generated muon falls outside of the trackers coverage, it behaves like a neutrino. Therefore, the recoil and recoil axes are defined as in the W signal, replacing neutrino momentum with the momentum of the second generated muon.

Φ modulation correction

The reconstructed $\vec{\not{E}}_T$ distribution is not isotropic in ϕ. The main sources of this modulation are the non-uniform reconstruction efficiency of low-p_T tracks and the non-uniform response of the HCAL and ECAL to the soft particles. Since a significant fraction of low-p_T particles comes from the additional minimum-bias interactions, it is expected that this ϕ modulation will be more pronounced in events with larger pileup. We also observe that the effect of modulation is larger in the data than in the simulation, and that the phase of the modulation is different. So, instead of matching the MC simulation to the data, we apply a correction to remove this modulation and make the $\phi(\vec{\not{E}}_T)$ distribution flat in both.

We derive the correction for ϕ modulation by studying the average perpendicular recoil as a function of boson ϕ for a different number of reconstructed vertices in both the data and the MC simulation. We first correct the $\vec{\not{E}}_T$ for muon momentum scale in both samples. Then we look at the average $u_\parallel$ profile as a function of boson q_T and fit it with the function

$$-\tilde{u}_\parallel(q_T) = (c_0 + c_1 q_T)\left(1 + \mathrm{erf}(\alpha q_T^\beta)\right). \tag{5.7}$$

This step is only needed to check that the amplitude of $\langle u_\parallel - \tilde{u}_\parallel(q_T)\rangle(\phi)$ variation is consistent with the amplitude of the $\langle u_\perp\rangle(\phi)$ variation. The phase difference should be $\pi/2$.

Figure 5.10 shows the profile of $\langle u_\parallel - \tilde{u}_\parallel(q_T)\rangle(\phi)$ and $\langle u_\perp\rangle(\phi)$ for 7 interaction vertices. Each such profile is fitted with $A_j(n)\cos(\phi - \phi_{0,j}(n))$, where n is the number of reconstructed vertices, and j denotes whether it is a perpendicular or parallel component. Then, in Fig. 5.11, we fit the amplitude of the perpendicu-

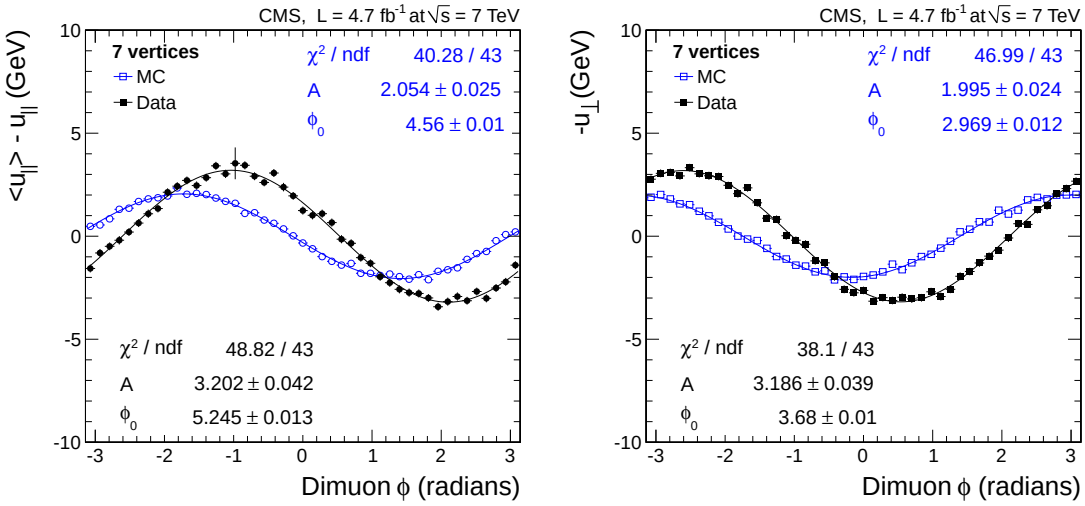

Figure 5.10: Parallel (left) and perpendicular (right) recoil profile as a function of boson ϕ for 7 reconstructed interaction vertices.

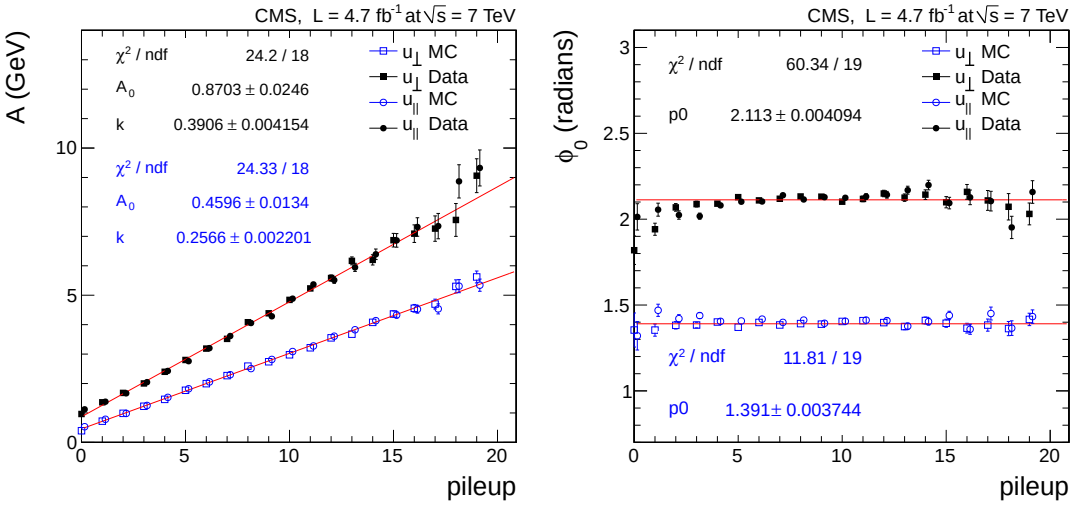

Figure 5.11: Amplitude (left) and phase (right) of recoil ϕ modulation as a function of reconstructed pileup.

lar recoil as a linear function of pileup and fit the phase ($\phi_{0,\perp} - \pi/2$ for the parallel component, and $\phi_{0,\parallel} - \pi$ for the perpendicular component) with a constant. The fits are only performed for the perpendicular component. The parallel components are overlaid only to check the consistency. To remove the ϕ modulation from $\vec{\not{E}}_T$, we add a 2d-vector to $\vec{\not{E}}_T$, whose direction is independent of pileup (but different in the data and in the simulation), and the amplitude is a linear function of pileup:

$$\begin{aligned} \not{E}_{\mathrm{X}} &= \not{E}_{\mathrm{X}} + (A_0 + k n_{pu}) \cos(\phi_0) \\ \not{E}_{\mathrm{Y}} &= \not{E}_{\mathrm{Y}} + (A_0 + k n_{pu}) \sin(\phi_0). \end{aligned} \tag{5.8}$$

Note, this correction is independent of the recoil axis and will be applied in all MC simulated and data events.

Average parallel recoil

After having corrected $\vec{\not{E}}_T$ for muon scale and ϕ modulation, we derive the average recoil as a function of boson q_T in 4 bins of the leading jet $|\eta|$: [0.0–1.2], [1.2–2.4], [2.4–3.0], [3.0–5.0]. Jets are formed by clustering all PF-candidates, except for identified PF-muons, with the anti-kt algorithm with cone size of $R = 0.5$. Each recoil profile is fitted with the following function:

$$-\tilde{u}_{\parallel}(q_T) = (c_0 + c_1 q_T)\left(1 + \mathrm{erf}(\alpha q_T^{\beta})\right). \tag{5.9}$$

As one can see from Fig. 5.12, the difference between average recoil in the data and in the MC simulation is quite sensitive to η of the jet against which the boson is recoiling.

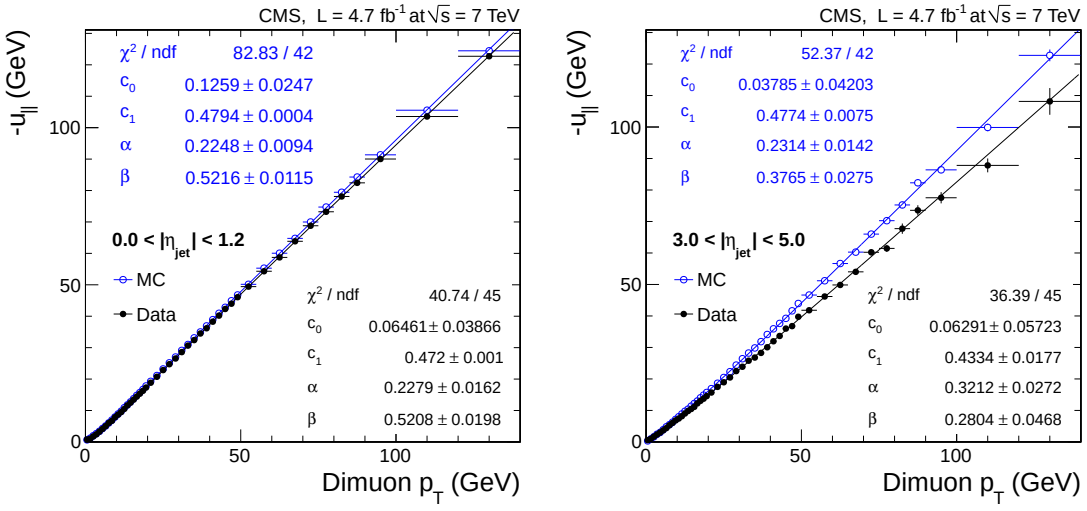

Figure 5.12: Profile of the recoil distribution in data (solid circles) and simulation (open circles) for two pseudorapidity bins of the leading jet, $0.0 < |\eta| < 1.2$ (left) and $3.0 < |\eta| < 5.0$ (right).

Resolution of perpendicular and parallel recoils

The resolution of the parallel and perpendicular recoil is measured as a function of q_T for different numbers of reconstructed vertices. Figure 5.13 shows an example distribution of $u_\perp$ and $(u_\parallel - \tilde{u}_\parallel(q_T; \eta_{jet}))$ for 10 GeV $< q_T <$ 12 GeV and 7 interaction vertices. Each such distribution is fitted with a Gaussian function. Figure 5.14 shows the σ of the result function from the previous step, parametrized as a function of q_T with the expression

$$\sigma(q_T; n) = \sqrt{N_n^2 + S_n^2 q_T}. \tag{5.10}$$

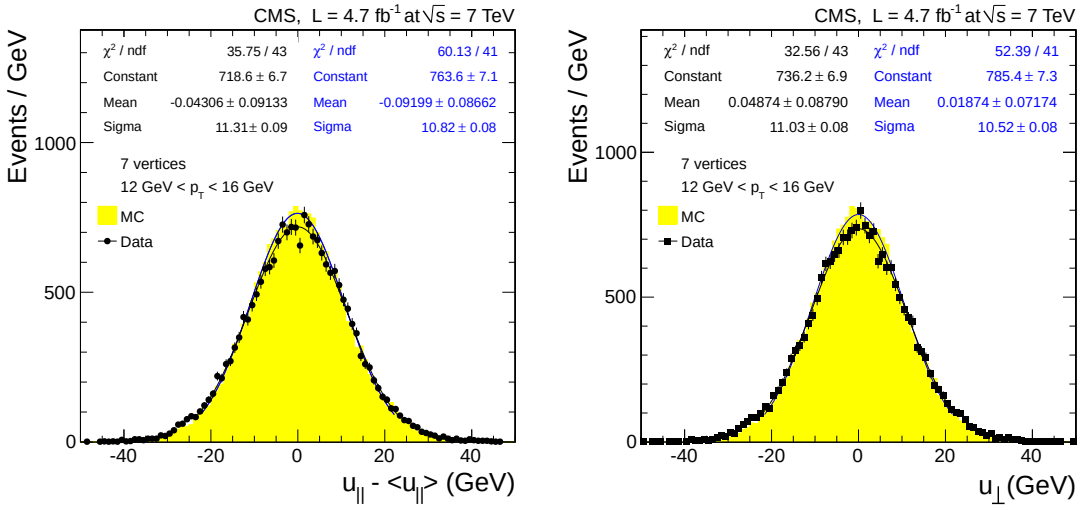

Figure 5.13: Distribution of the parallel (left) and the perpendicular (right) recoil for 10 GeV $< q_T <$ 12 GeV and 7 interaction vertices.

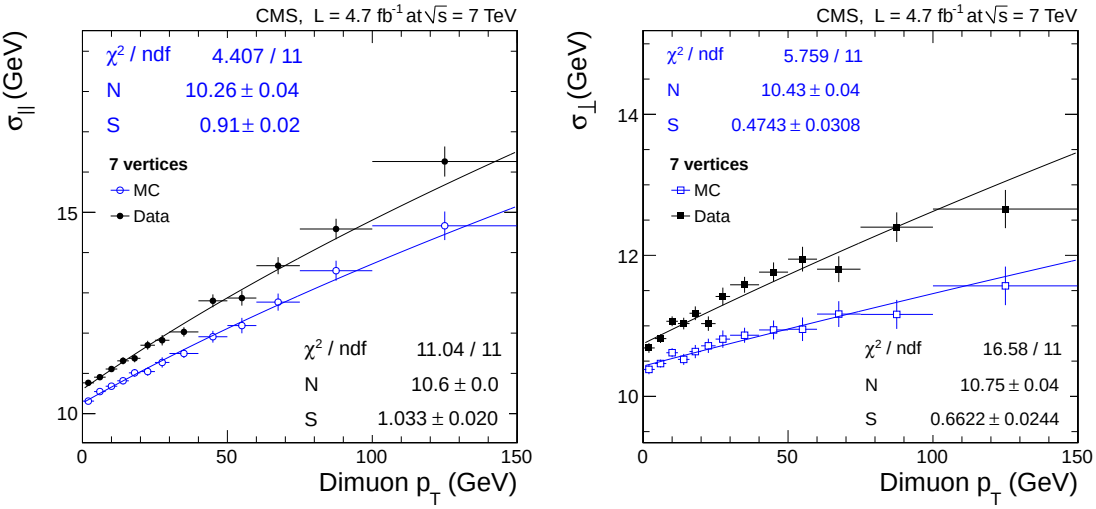

Figure 5.14: Resolution of the parallel (left) and the perpendicular (right) recoil as a function of boson q_T for 7 interaction vertices for data (solid circles) and MC simulation (open circles).

Closure Test

We test the performance of the $\vec{\not{E}}_T$ tuning procedure in our Drell-Yan control sample itself ("closure test"). All $\vec{\not{E}}_T$ correction steps can be summarized as follows:

1. Correct $\vec{\not{E}}_T$ for the muon scale bias in both the data and the MC simulation.
2. Remove the ϕ modulation (Eq. 5.8) in both the data and the MC simulation.
3. Shift the average and scale the resolution of recoil components in the simulation to match the values in data:

$$u_{\parallel} = \left(u_{\parallel} - \tilde{u_{\parallel}}^{MC}\right) \frac{\sigma_{\parallel}^{DA}}{\sigma_{\parallel}^{MC}} + \tilde{u_{\parallel}}^{DA}, \tag{5.11}$$

$$u_{\perp} = u_{\perp} \frac{\sigma_{\perp}^{DA}}{\sigma_{\perp}^{MC}}, \tag{5.12}$$

   where $\tilde{u_{\parallel}}$ and $\sigma_{\parallel,\perp}$ are calculated with Eqs. 5.9 and 5.10, respectively.
4. Recalculate the $\vec{\not{E}}_T$ in the MC simulation with the corrected recoil.

Figure 5.15 shows that $\vec{\not{E}}_T$ corrections improve the agreement between data and MC simulation and remove $\phi(\vec{\not{E}}_T)$ modulations from both.

5.2.6 Drell-Yan normalization correction

The Drell-Yan $Z/\gamma^* \to \mu^+\mu^-$ process is one of the dominant backgrounds in the selected sample and makes up about 3–8% of all events depending on the pseudorapidity bin. When extracting the $W^{\pm} \to \mu^{\pm}\nu$ signal yields in each pseudora-

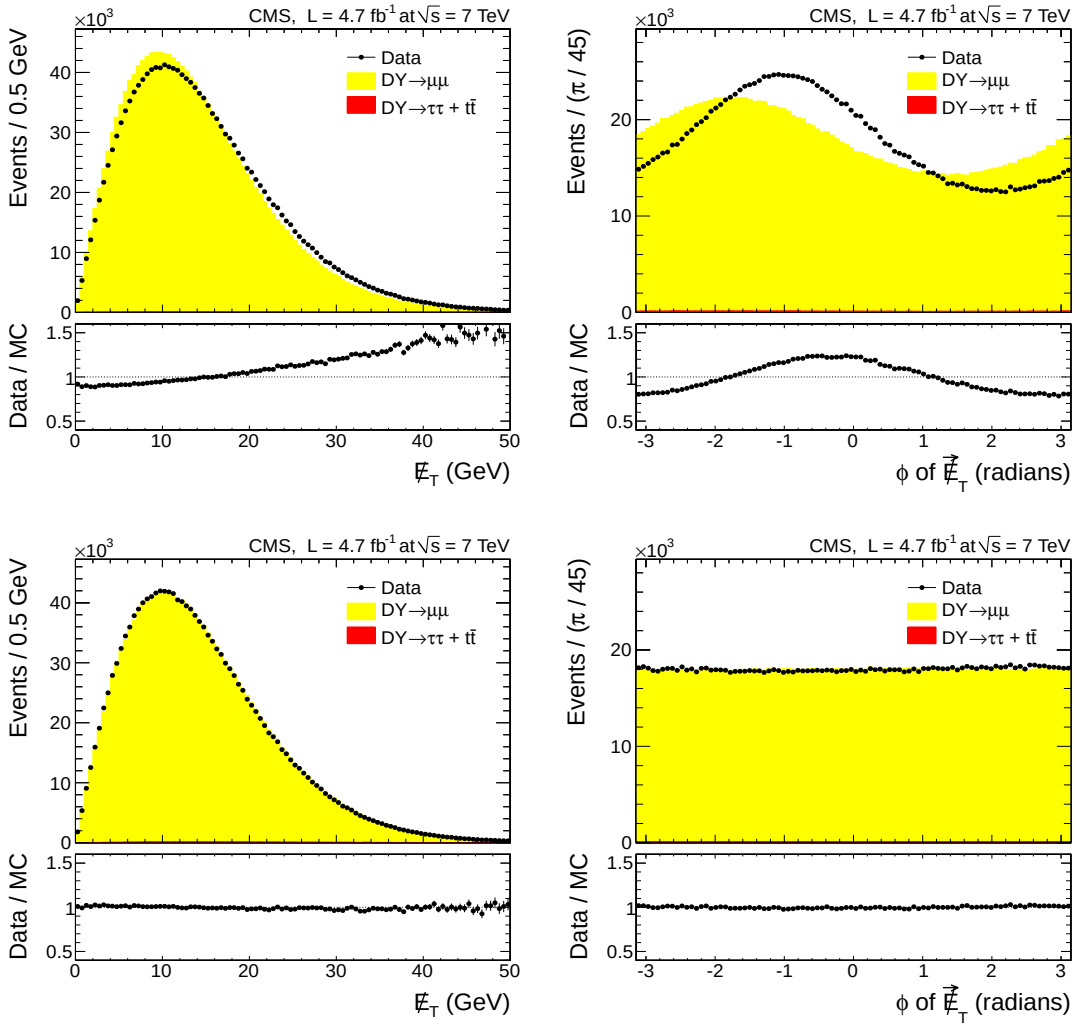

Figure 5.15: Uncorrected (top) and corrected (bottom), $\not{E}_{\mathrm{T}}$ (left) and $\phi(\vec{\not{E}}_T)$ (right) distributions in Drell-Yan control sample.

pidity bin with the maximum likelihood fit, the normalization of $Z/\gamma^* \to \mu^+\mu^-$ background is fixed. It is determined as follows.

The entire generated POWHEG sample is first normalized using the theoretical cross section, calculated at NNLO of QCD, to the measured integrated luminosity. Then, to take into account mismodeling of the muon selection ef-

ficiencies, all simulated $Z/\gamma^* \to \mu^+\mu^-$ events in the Drell-Yan control region are weighted with the following factors:

$$w = \frac{\epsilon^{full}_{data}(Q_1, p_{T1}, \eta_1)}{\epsilon^{full}_{MC}(Q_1, p_{T1}, \eta_1)} \times \frac{\epsilon^{offline}_{data}(Q_2, p_{T2}, \eta_2)}{\epsilon^{offline}_{MC}(Q_2, p_{T2}, \eta_2)}. \tag{5.13}$$

At the end, the residual k-factors are derived in the six dimuon mass bins listed in Table 5.4, which fix the normalization of simulated events to the data. These k-factors are by default applied to correct the $Z/\gamma^* \to \mu^+\mu^-$ background normalization in the W signal region, on top of the efficiency corrections, described in Section 5.2.4. When evaluating systematic uncertainties, the full correction is included in the variation of $Z/\gamma^* \to \mu^+\mu^-$ background normalization. The details will be discussed in Section 5.5.

Table 5.4: $Z/\gamma^* \to \mu^+\mu^-$ normalization k-factors in six mass bins.

Mass bin(GeV)	15 – 30	30 – 40	40 – 60	60 – 120	120 – 150	150 – ∞
k-factor	1.637	1.265	1.040	1.027	1.081	1.159

Figure 5.16 shows the distribution of leading muon η in data and simulated $Z/\gamma^* \to \mu^+\mu^-$ events for positive and negative muons. The normalization of the MC simulation has been fixed with the efficiency correction factors from Eq. 5.13 and the residual mass-dependent k-factors described above. The uncertainty band includes the full k-factor values in addition to uncertainties of the PDFs, muon momentum, and selection efficiencies.

5.2.7 QCD $\not{E}_{\mathrm{T}}$ shape

By default, all $\vec{\not{E}}_T$ corrections described in the previous Sections are also applied to QCD MC simulated events. Although the event topology of QCD events is

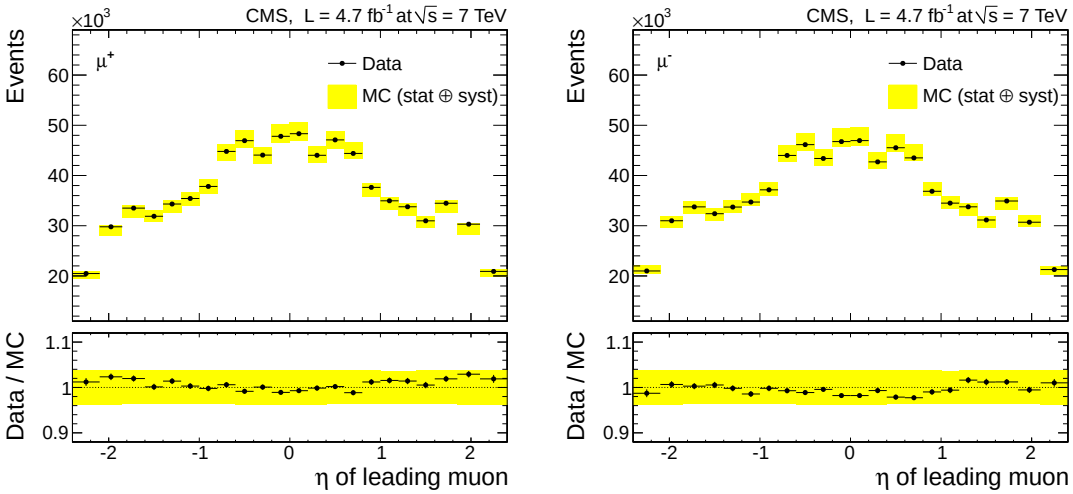

Figure 5.16: Leading positive (left) and negative (right) muon pseudo-rapidity distributions.

quite different from that of $Z/\gamma^* \to \mu^+\mu^-$ and $W \to \mu\nu$ events, there are common sources of disagreement between the data and the simulation, such as pileup, which we want to take into account. In QCD events we define the recoil axes to be oriented along the reconstructed muon's $\vec{p}_T$ and calculate the relevant $\vec{\not{E}}_T$ correction parameters using its magnitude.

In this Section we test our $\vec{\not{E}}_T$ correction technique in a QCD control region. Events selected for the QCD-enriched sample fail the default isolated single muon HLT, but pass the corresponding non-isolated single muon trigger. We also invert the offline tracker isolation. The non-isolated trigger was prescaled and the prescale factor was increasing during the 2011 data-collection period. Our sample is largely dominated by the very first segment of the 2011A data, consisting of a total integrated luminosity of 0.28 fb^{-1}.

Figure 5.17 shows good agreement between the $\not{E}_{\mathrm{T}}$ distributions of the data

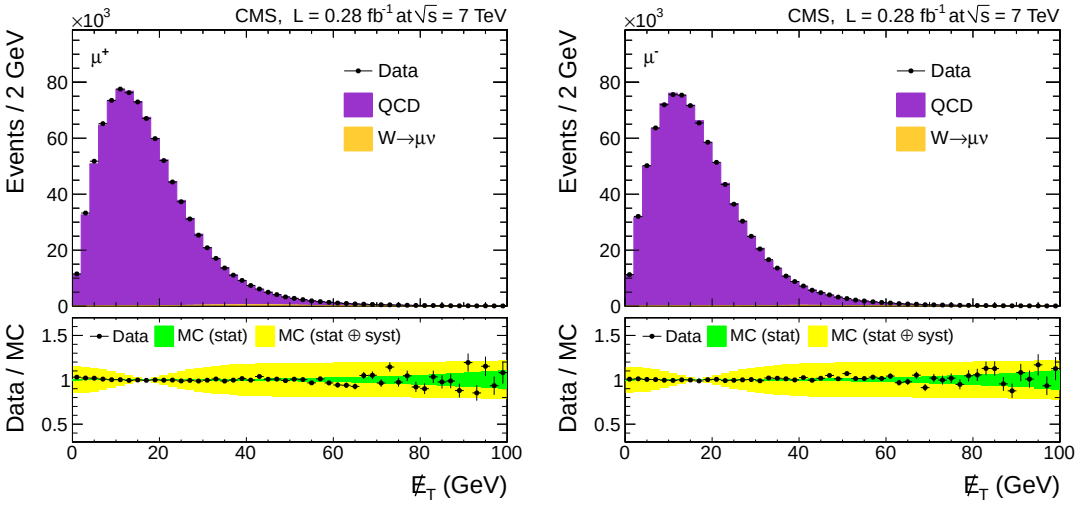

Figure 5.17: The $\not\!\!E_T$ distribution in the QCD-enriched sample, containing positively (left) and negatively (right) charged reconstructed muon. $\vec{\not\!\!E}_T$ corrections have been applied in both the data and the simulation. The $W \to \mu\nu$ contribution is normalized to the measured luminosity and the QCD MC sample is normalized to the data. The green shaded band in each ratio plot shows the statistical uncertainty of the QCD MC $\not\!\!E_T$ shape and the yellow shaded band shows the total uncertainty, including the systematic error.

and the MC simulation after all the corrections were applied. Because the QCD events are quite different from the $Z/\gamma^* \to \mu^+\mu^-$ events and the recoil axes (as well as the recoil itself) is not well defined, we apply the conservative variation of the QCD $\not\!\!E_T$ shape when evaluating systematic uncertainty. To do so, we remove the recoil correction and the smearing part from the $\vec{\not\!\!E}_T$ corrections and fit the ratio of the resulting $\not\!\!E_T$ distribution to the fully corrected distribution, using the $p_0 + p_1 Gaus(0, p_3)$ function. Then we re-weight the fully corrected $\not\!\!E_T$ distribution. The corresponding variations are shown by the yellow bands on the bottom parts in Fig. 5.17.

5.3 Fitting with finite MC samples

The $W^{\pm} \to \mu^{\pm}\nu$ signal yields in each pseudorapidity bin are extracted by fitting the $\not\!\!E_{\mathrm{T}}$ distribution in data with the signal and the background templates. As described in the previous Section, all templates are derived from the MC simulation and are corrected with the data-driven techniques.

In our analysis we employ the binned maximum likelihood fit technique developed by Barlow and Beeston (BB), which takes into account statistical uncertainties in both data and simulation. As described in reference [50], this method assumes that the bin-contents of all simulated histograms are smeared according to a Poisson distribution around their corresponding true values. However, since the total number of events in each MC source is a deterministic number, the template distributions should be treated as multinomials[3]. If the number of simulated events is much larger than the number of events in data, which is normally the case, then the BB approximation works well[4]. However, the total number of generated signal and QCD events in our analysis is less than what we expected given our data sample (Table 5.3). In such a case, BB approximation can lead to a notable overestimation of statistical errors.

In the following Sections we first describe the BB technique, then we show two ways of calculating the correct error matrix of floating parameters, regardless of the generated MC samples size.

[3]Even if one does not want the total number of events in a given template to be deterministic (e.g. to take the statistical uncertainty of the event selection efficiency into account), if its normalization is floating in the fit, then its distribution must be treated as a multinomial.

[4]Of course, if the number of simulated events is sufficiently large, then the statistical errors in MC templates can be neglected altogether.

5.3.1 Barlow-Beeston Technique

A typical problem in many High Energy Physics analyses is to estimate the composition of a data sample based on the MC simulations of the various sources. A commonly accepted approach is to fit some distribution (generally of more than one dimension) in data events to simulated templates.

Suppose we have a binned distribution d_i ($1 \leq i \leq N_B$) of some variable in our data sample, which we want to use to estimate its composition. We also have N_S simulated template histograms with the same binning for all processes that we expect to contribute to our data sample. The total number of events in a simulated source j we will denote by $M_j = \sum_{j=1}^{N_S} a_{ji}$, where a_{ji} is the number of events it contributes to bin i. The corresponding total expected number of events in our data sample we will denote by D_j. The key variables in the BB formalism are the *strength-factors*, $p_j = D_j/M_j$, indicating the factor by which the source j should be scaled to yield the corresponding expected number of events in data. In our analysis we will be interested in the total number of events D_j in data for each source j.

In the nominal (i.e. without BB) approach, ignoring the statistical fluctuations in simulated templates, the total predicted number of events in a bin i can be then written as:

$$g_i = \sum_{j=1}^{N_S} p_j a_{ji}. \tag{5.14}$$

To find the most probable values for p_j, or equivalently, for D_j, one would maximize the log-likelihood

$$\ln \mathcal{L} = \sum_{i=1}^{N_B} d_i \ln \frac{g_i}{d_i} - g_i. \tag{5.15}$$

In the BB technique, statistical uncertainties in simulated templates are also

taken into account. Namely, it is acknowledged that the observed a_{ji} counts are in fact smeared around their corresponding true values, A_{ji}, which are in general unknown. The total predicted number of events in a bin i is thus expressed as

$$f_i = \sum_{j=1}^{N_S} p_j A_{ji}, \tag{5.16}$$

and the likelihood 5.15 is extended to include the fluctuations in the MC templates:

$$\ln \mathcal{L} = \sum_{i=1}^{N_B} \left(d_i \ln \frac{f_i}{d_i} - f_i + \sum_{j=1}^{N_S} \left(a_{ji} \ln \frac{A_{ji}}{a_{ji}} - A_{ji} \right) \right). \tag{5.17}$$

The likelihood 5.17 has N_S unknown parameters of interest p_j and $N_S \times N_B$ unknown variables A_{ji}, which we are not really interested in. Differentiation of this likelihood with respect to p_j's leads to the following set of N_S equations,

$$\sum_{i=1}^{N_B} \frac{d_i A_{ji}}{f_i} - A_{ji} = 0 \qquad \forall j, \tag{5.18}$$

and differentiation with respect to A_{ji}'s leads to the following set of $N_S \times N_B$ equations,

$$\frac{d_i p_j}{f_i} - p_j + \frac{a_{ji}}{A_{ji}} - 1 = 0 \qquad \forall i, j \tag{5.19}$$

Then the variable $t_i = 1 - d_i/f_i$ is introduced, which significantly simplifies the Eq. 5.19. Its value equals unity if d_i is zero, otherwise it can be found by solving its corresponding equation,

$$\frac{d_i}{1 - t_i} = \sum_j \frac{p_j a_{ji}}{1 + p_j t_i}, \qquad \forall i, \tag{5.20}$$

for a given set of $\{p_j\}$. The predicted number of events from each source can then be calculated as

$$A_{ji} = \frac{a_{ji}}{1 + p_j t_i}. \tag{5.21}$$

Special considerations apply in a bin if the number of events a_{ki} for one or more MC sources is zero. For a source k with a zero count in a bin i, $a_{ki} = 0$, the

predicted A_{ki} can be non-zero, only if p_k is the largest of all strength-factors and its expression,

$$A_{ki} = \frac{d_i}{1 + p_k} - \sum_{j \neq k} \frac{p_j a_{ji}}{p_k - p_j} \tag{5.22}$$

yields a positive value.

To summarize, for a given set of parameters of interest $\{p_j\}$ one can numerically calculate the optimal values of A_{ji}, that maximize the likelihood 5.17, either by using the Eqs. 5.20 and 5.21, or the Eq. 5.22. The optimal values for $\{p_j\}$ are then typically found by minimizing the $-2 \ln \mathcal{L}$, using one of the standard minimization tools, e.g. MINUIT [62].

5.3.2 Adjusting the error matrix after the fit

The BB formalism, described above, assumes that a_{ji}'s are smeared around the true values, A_{ji}'s, according to the Poisson distribution. Since the total number of events in each MC source is a deterministic number, however, the distributions are in fact multinomial. The Poisson treatment of these distributions leads to overestimated uncertainties of corresponding strength factors p_j (or, equivalently, of D_j). In this Section we discuss a simple way of adjusting the error matrix for $\{D_j\}$.

Let's assume that the BB fit, described in the previous Section, reports the optimal strength-factors $\{p_j\}$ along with the corresponding uncertainties $\{\delta p_j\}$ and the correlations $\rho(\delta p_j, \delta p_k)$. The corresponding optimal values for D_j can then be calculated as

$$D_j = p_j \times M_j \tag{5.23}$$

Since the MC distributions in the BB likelihood are treated as Poisson, the total predicted number of events $\sum_i A_{ji}$ in each MC source is floating in the fit. Therefore, the reported statistical uncertainty of the strength factors will contain the uncertainty of both the template shapes and the normalizations. This can be quantified as follows:

$$\frac{\delta p_j^2}{p_j^2} = \frac{\delta D_j^2}{D_j^2} + \frac{\delta M_j^2}{M_j^2}, \tag{5.24}$$

where $\delta D_j / M_j$ would be the statistical error of the strength factor p_j, if the total expected number of events from the corresponding MC source, $\sum_i A_{ji}$, were not allowed to float. So, given the optimal values and errors of p_j, corresponding to the likelihood 5.17, we can adjust the uncertainties of D_j after the fit, as

$$\delta D_j = \sqrt{M_j^2 \delta p_j^2 - p_j^2 \delta M_j^2}. \tag{5.25}$$

Since there are no correlations between the statistical uncertainties of the total numbers of events in the different MC sources, off-diagonal elements of the covariance matrix do not need to be corrected. Therefore one can adjust the correlation factors as

$$\rho(\delta D_j, \delta D_k) = \frac{M_j \delta p_j M_k \delta p_k}{\delta D_j \delta D_k} \rho(\delta p_j, \delta p_k), \tag{5.26}$$

where δD_j and δD_k are calculated according to the Eq. 5.25.

The Eqs. 5.25 and 5.26 provide a simple way to adjust the error matrix on $\{D_j\}$ using the optimal values and uncertainties of the strength factors in BB likelihood. If, however, different MC sources are linked in a certain complicated way, or one wants to extract a certain combination of various sources directly from the fit, this approach might be not applicable (or the correction procedure might get too involved). In the next Section we describe an alternative approach, where the fit directly returns the correct error matrix without the need for any adjustments.

5.3.3 Constrained Barlow-Beeston likelihood fit

An alternative way to extract the correct error matrix of floating parameters from the fit is to maximize the likelihood 5.17 in the constrained parameter-space, where the total number of predicted events in each MC source is fixed to the corresponding observed value:

$$\sum_i A_{ji} = \sum_i a_{ji} \qquad \forall j \tag{5.27}$$

As described in the reference [50], these normalization conditions are satisfied automatically at the maximum of the original BB likelihood. Therefore these constraints should not change the optimal values for the strength-factors. However, since the allowed space for free parameters is now limited, the reported error matrix will be different.

To implement the above constraints, we add the Lagrange-Multiplier terms for each MC source to the likelihood 5.17,

$$\ln \mathcal{L} = \sum_{i=1}^{N_B} \left(d_i \ln \frac{f_i}{d_i} - f_i + \sum_{j=1}^{N_S} \left(a_{ji} \ln \frac{A_{ji}}{a_{ji}} - A_{ji} + \lambda_j (A_{ji} - a_{ji}) \right) \right), \tag{5.28}$$

and rewrite the math accordingly. Taking the differentials with respect to p_j leads to the same Eq. 5.18. The differentials with respect to A_{ji} now depend on λ_j,

$$\frac{d_i p_j}{f_i} - p_j + \frac{a_{ji}}{A_{ji}} - 1 + \lambda_j = 0 \qquad \forall i, j. \tag{5.29}$$

And differentials with respect to λ_j lead to the constraining Eq. 5.27. Following the same steps and introducing $t_i = 1 - d_i/f_i$, we get the following two sets of equations:

$$\frac{d_i}{1 - t_i} = \sum_j \frac{p_j a_{ji}}{1 + p_j t_i - \lambda_j}, \qquad \forall i \tag{5.30}$$

$$\sum_i \frac{a_{ji}(\lambda_j - p_j t_i)}{1 + p_j t_i - \lambda_j} = 0, \qquad \forall j \tag{5.31}$$

So, instead of N_B independent Eqs. 5.20 for t_i, now we have N_B equations for t_i which depend on $\{\lambda_j\}$; and N_S equations for λ_j, which depend on $\{t_i\}$, which is a slight technical complication. The two sets of equations are solved iteratively. In each iteration a current set of values $\{t_i\}$ is used to solve all N_S Eqs. 5.31 for λ_j; then the result set of $\{\lambda_j\}$ is used to solve all N_B Eqs. 5.30 for t_i; and so on, until the required precision is reached. Each equation is solved numerically using Newton's method.

Having found optimal $\{t_i\}$ and $\{\lambda_j\}$ values for a given set of $\{p_j\}$, the predicted number of events from each MC source in each bin is calculated as

$$A_{ji} = \frac{a_{ji}}{1 + p_j t_i - \lambda_j}. \tag{5.32}$$

We also re-write the equations concerning the zero bin content case in the MC templates. For a given source k, which has a zero count in bin i, $a_{ki} = 0$, the corresponding predicted number of events A_{ki} can be non-zero only if this MC source has a maximum value for $p_k/(1 - \lambda_k)$ and its final expression, which now reads,

$$A_{ki} = \frac{d_i}{1 - \lambda_k + p_k} - \sum_{j \neq k} \frac{p_j a_{ji}}{p_k(1 - \lambda_j) - p_j(1 - \lambda_k)} \tag{5.33}$$

returns a positive value.

The advantage of this method is that the uncertainties in the floating parameters of the fit do not need to be adjusted. Therefore, one can replace the strength-factors in the likelihood 5.28 by the parameters of ultimate interest (e.g. $\{N_j\}$, or various combinations between them, such as sums and asymmetries); and directly retrieve the correct covariance matrix of their uncertainties from the fit.

5.3.4 Toy MC Studies

We use a toy study to examine the performance of each method described in the previous Sections. We generate distributions similar to the $\not\!\!E_{\mathrm{T}}$ distributions in signal and background events. In the toy study $W^{\pm} \to \mu^{\pm}\nu$, signal events in data are contaminated by a QCD background. The total number of generated signal (QCD) events in the MC simulation is ~1.5 (10) times less than in "data". Table 5.5 shows the details of the toy setup.

Table 5.5: The setup for toy studies with maximum likelihood fit.

	W^+	W^-
true number of events in data D^T	550,000	350,000
true number of signal events in data D_S^T	500,000	300,000
true number of QCD events in data D_Q^T	50,000	50,000
number of signal events in MC M_S	300,000	200,000
number of QCD events in MC M_Q	5,000	5,000

The $\not\!\!E_{\mathrm{T}}$ shapes in signal (f_S) and QCD (f_Q) events are defined as follows:

$$\begin{aligned} f_S(x) &= x \times \mathrm{Gaus}(x; m = 40, \sigma = 15), & 0 < x < 100 \\ f_Q(x) &= x \times \mathrm{Gaus}(x; m = 0, \sigma = 17), & 0 < x < 100 \end{aligned} \tag{5.34}$$

The shapes are identical for two charges, both in data and in the MC templates. All histograms have 100 bins of width equal to 1.0.

We generate 10,000 pseudo-experiments with the parameters listed above. In each round we smear the total number of $W^{\pm} \to \mu^{\pm}\nu$ and QCD events according to the Poisson distribution around the true values listed in Table 5.5. We fill the corresponding histograms by randomly sampling the shapes in Eqs. 5.34. Then we perform the simultaneous fit of the $\not\!\!E_{\mathrm{T}}$ distributions in W^+ and W^- candidate events with MC templates, floating three parameters:

1. the strength-factor for $W^+ \to \mu^+\nu$ events, p_+
2. the strength factor for $W^- \to \mu^-\nu$ events, p_-
3. the common strenth-factor for the QCD$^+$ and QCD$^-$ events, p_Q.

The example $\not{E}_T$ distributions in W^+ and W^- events are depicted in Fig. 5.18.

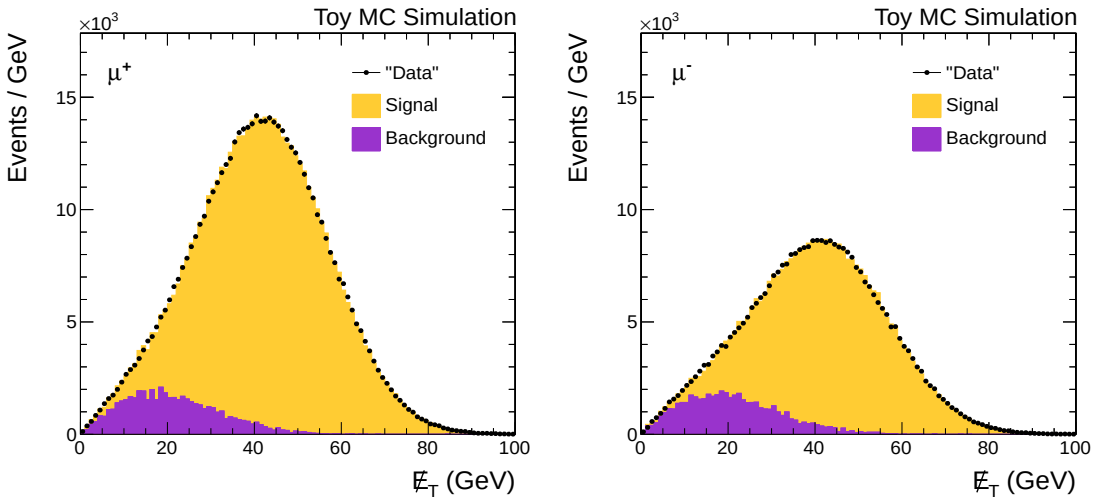

Figure 5.18: Example $\not{E}_T$ distributions in W^+ (left) and W^- (right) candidate events in one of the toy experiments. Each MC source is scaled by the strength-factor evaluated from the fit.

In each pseudo-experiment, we calculate the predicted number of events in data for each source as $N_j = p_j \times M_j$. The fit is performed and the uncertainties and correlations are evaluated in three different ways:

1. Nominal BB fit, $\delta N_j = M_j \delta p_j$; $\rho(\delta N_j, \delta N_k) = \rho(\delta p_j, \delta p_k)$
2. Nominal BB fit, adjusted uncertainties and correlations (Eq. 5.25 and 5.26)
3. Constrained BB fit, $\delta N_j = M_j \delta p_j$; $\rho(\delta N_j, \delta N_k) = \rho(\delta p_j, \delta p_k)$

Table 5.12 shows the uncertainties and correlations calculated with the three methods listed above in one of the toy experiments. The asymmetry and its uncertainty is calculated using the Eqs. 5.36 and 5.37. One can see that while the constrained BB fit and the adjusted errors give the same results, the raw uncertainties from the BB fit are overestimated by about 40%.

Table 5.6: The statistical uncertainties and correlations calculated with the three fit methods in one of the toy experiments. The central values in all three cases are the same: $N_+ = 499015$, $N_- = 300944$, $N_Q = 101176$ and $A = 0.2476$.

	δN_+	δN_-	δN_Q	$\rho_{-,Q}$	$\rho_{+,Q}$	$\rho_{+,-}$	$\delta A(\%)$
Nominal fit, raw unc.	1321	1038	1443	-28.8	-27.6	8.0	0.20
Nominal fit, adjusted unc.	957	790	1029	-53.1	-53.4	14.4	0.14
Constrained fit, raw unc.	957	790	1029	-53.1	-53.4	14.4	0.14

Figure 5.19 shows the results from the toy study with the constrained BB fits. The average values of calculated correlation factors over the 10,000 pseudo-experiments between the uncertainties are $\langle\rho(\delta N_-, \delta N_Q)\rangle = -53.8$, $\langle\rho(\delta N_+, \delta N_Q)\rangle = -53.2$, and $\langle\rho(\delta N_+, \delta N_-)\rangle = 14.8$. These values are consistent with the values displayed in the 2-dimensional distributions in Fig. 5.19. All pull distributions in Fig. 5.19 have a mean consistent with zero and a width consistent with unity. Figure 5.20 shows that the nominal Likelihood fit using Eq. 5.15 (i.e. ignoring uncertainties in MC templates) returns biased results and underestimates the uncertainties by about ~30% in our toy setup; the nominal BB approach yields unbiased results but overestimates the uncertainties by about the same amount; while the constrained BB fit returns unbiased results with correct uncertainties.

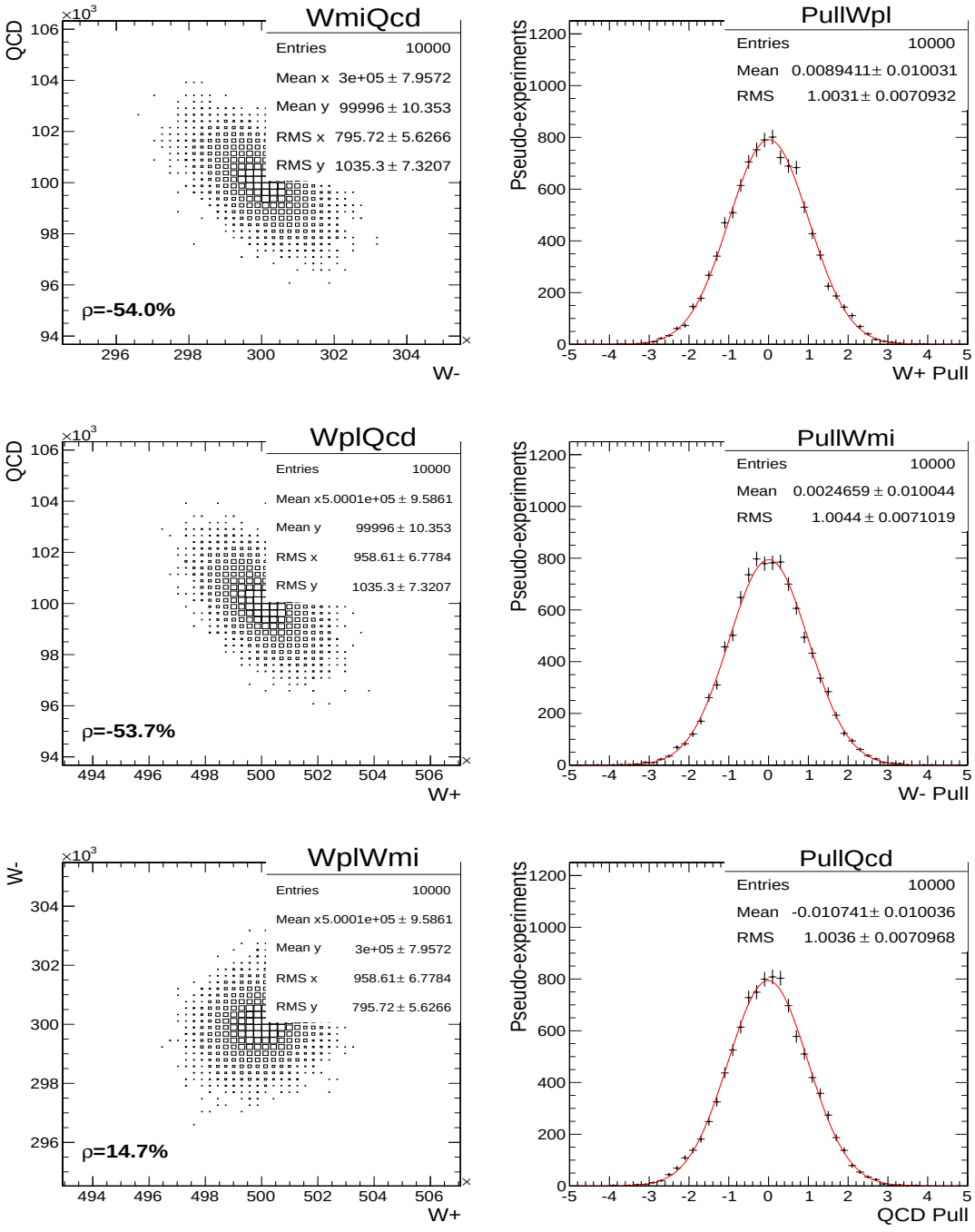

Figure 5.19: Results from the toy study with constrained fits. The left plots show the two-dimensional distributions of N_Q vs. N_-, N_Q vs. N_+ and N_- vs. N_+, along with the corresponding correlation factors. The right plots show the distributions of the pulls for N_+, N_- and N_Q.

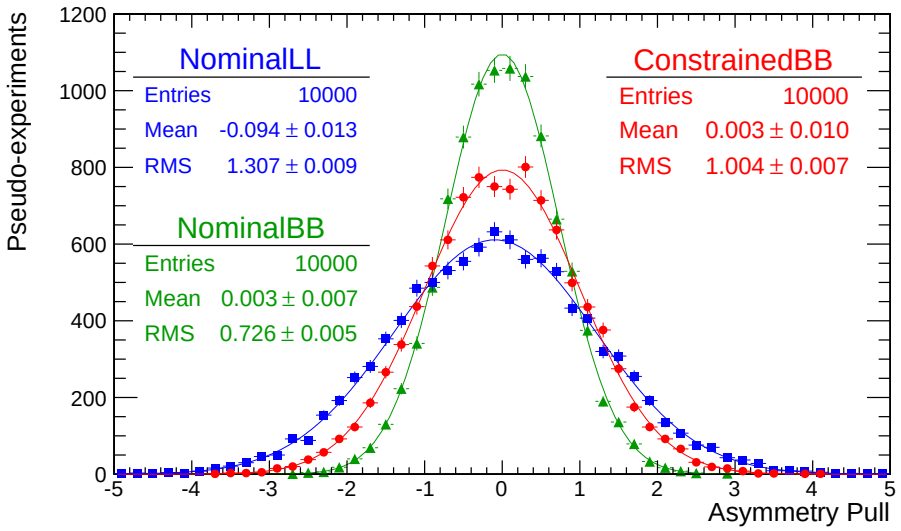

Figure 5.20: Distribution of the asymmetry pull in toy experiments for the nominal likelihood fits with Eq. 5.15 (blue squares), the nominal BB fits (green triangles), and the constrained BB fits (red circles).

5.4 Extraction of the signal and charge asymmetry

Having applied all the online and offline muon selection criteria described in Section 5.1, our selected data sample consisted of about 12.9 million W^+ and 9.1 million W^- candidate events, of which about 84% were $W^\pm \to \mu^\pm \nu$ signal events, 8% were QCD background and the remaining 8% were electroweak and $t\bar{t}$ background events. The signal and background compositions differ across different pseudorapidity bins. To extract the number of $W^\pm \to \mu^\pm \nu$ events and calculate the charge asymmetry in each of the 11 pseudorapidity bins, we fit the $\not\!\!E_{\mathrm{T}}$ distributions simultaneously in W^+ and W^- candidate events with the MC simulated templates, using the constrained BB maximum likelihood technique described in Section 5.3.3.

The total likelihood for the simultaneous fit is written as

$$\ln \mathcal{L} = \sum_{q=+,-} \sum_{i=1}^{N_B} \left(d_{qi} \ln \frac{f_{qi}}{d_{qi}} - f_{qi} + d_{qi} + \sum_{j=1}^{N_S} \left(a_{qji} \ln \frac{A_{qji}}{a_{qji}} + (\lambda_j - 1)(A_{qji} - a_{qji}) \right) \right), \tag{5.35}$$

where

- d_{qi} is the data count in bin i for charge q;
- a_{qji} is the raw count of MC source j with charge q in bin i;
- A_{qji} is the expected count of MC source j with charge q in bin i;
- $f_{qi} = \sum_{j=1}^{N_{sources}} p_j w_{qji} A_{qji}$ is the total predicted content of bin i in data for charge q, where p_j's are strength-factors and w_{qji} is the average weight for MC source j with charge q in bin i; and
- λ_j is the Lagrange multiplier for source j.

In this likelihood the constant terms have been added such that in the large statistics limit, $-2 \ln \mathcal{L}$ returns the χ^2 value. This value will be used to check the goodness of each fit.

All MC templates are first normalized to the theoretical cross sections. Then they are corrected for the different muon selection efficiencies in the data and in the simulation. Additional mass-dependent k-factors are applied to the $Z/\gamma^* \to \mu^+\mu^-$ background events. The normalizations of the QCD templates with positive (QCD^+) and negative (QCD^-) reconstructed muons are corrected up-front, such that the ratio between them equals the value measured in the QCD control region. Relative QCD^+/QCD^- normalization will be discussed in more detail in the systematics Section. The template shapes are derived from the MC simulation and are corrected with data-driven techniques. All initial correction

factors for the normalization and the shape of each MC simulated template are contained in w_{qji} weights.

The floating parameters in the fits are the total number of $W^+ \to \mu^+\nu$ events (N^+), the total number of $W^- \to \mu^-\nu$ events (N^-), and the strength factor for QCD events, which is common for the two charges. The strength factor for the $W^\pm \to \tau^\pm\nu$ background is equal to that for the $W^\pm \to \mu^\pm\nu$ signal for each charge. The normalization of other electroweak and $t\bar{t}$ backgrounds remains fixed, with the strength factors equal to unity.

After the fit we calculate the "raw" charge asymmetry and its error in each pseudorapidity bin with the following equations:

$$A_0 = \frac{N_+ - N_-}{N_+ + N_-} \tag{5.36}$$

$$\delta A_0 = \sqrt{f_+^2 \delta N_+^2 + f_-^2 \delta N_-^2 + 2\rho f_+ f_- \delta N_+ \delta N_-}, \tag{5.37}$$

where $f_\pm = \pm 2N_\mp/(N_+ + N_-)^2$.

Figure 5.21 shows the example $\not\!\!E_{\rm T}$ distributions for W^+ and W^- candidate events in three muon pseudorapidity bins for $p_T > 25$ GeV. The $W^\pm \to \mu^\pm\nu$ and QCD templates have been scaled according to the corresponding fit results. Table 5.7 summarizes the results of all fits for $p_T > 25$ GeV and $p_T > 35$ GeV. The second and third columns show the expected number of W^+ and W^- events. The correlations between them are about 15%. These correlations are induced by common QCD strength factors for the two charges. The χ^2 values indicate a good quality fit in all pseudorapidity bins.

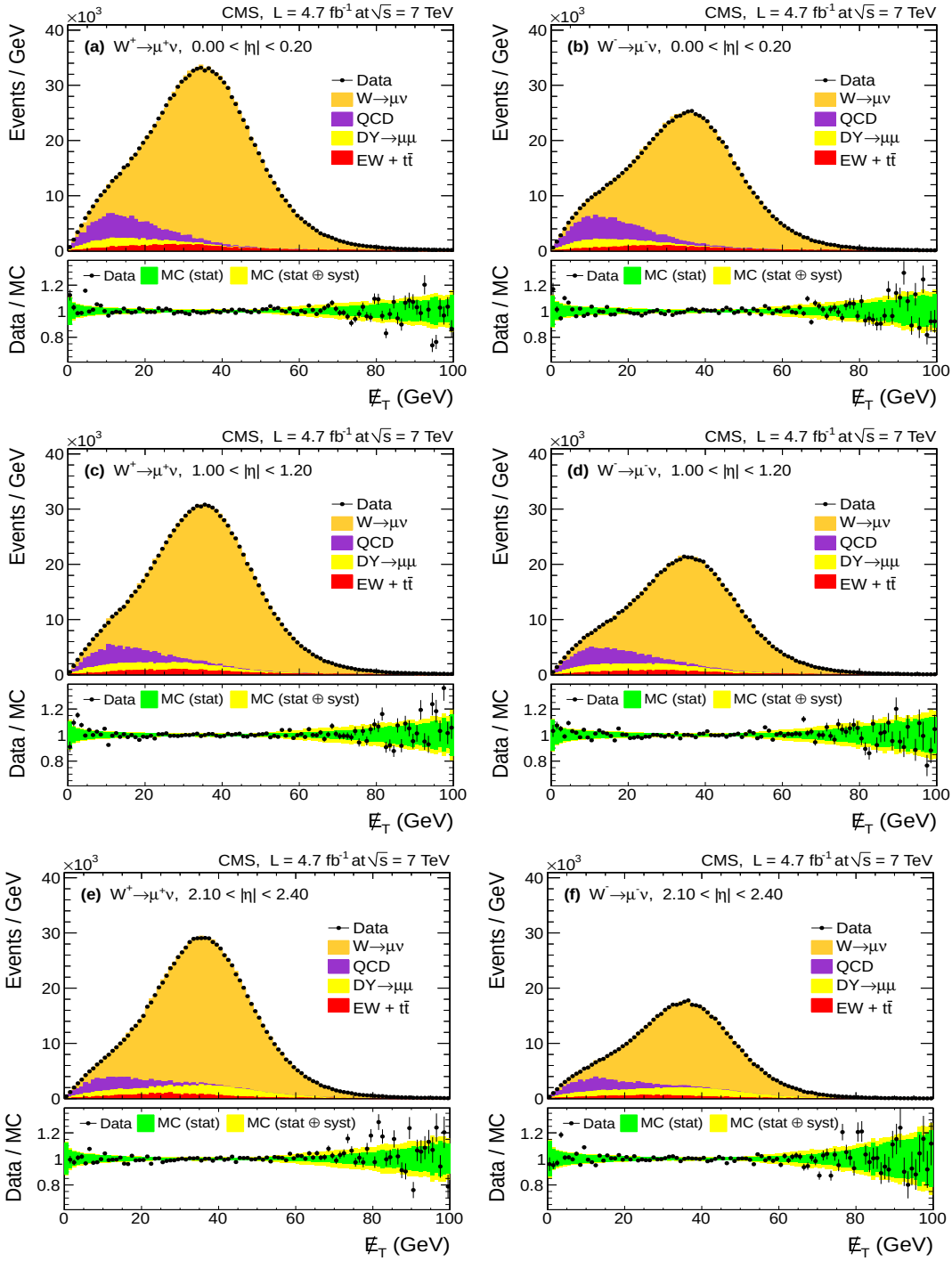

Figure 5.21: $\not\!\!E_T$ distributions in $W^{\pm} \to \mu^{\pm}\nu$ candidates with $p_T > 25$ GeV and $0.0 \leq |\eta| < 0.2$ (a, b), $1.0 \leq |\eta| < 1.2$ (c, d), and $2.1 \leq |\eta| < 2.4$ (e, f). The ratios between the data points and the total MC predictions are shown on the bottom of each panel. The green shaded band shows the statistical uncertainty; and the yellow shaded band shows the total uncertainty, including all systematic errors discussed in Section 5.5.

Table 5.7: Summary of fitted N^+ and N^-, their correlation coefficients, the χ^2 values, and the extracted raw charge asymmetries A_0. Here the correlations and A_0 are in units of percent.

η bin	$N_+/10^3$	$N_-/10^3$	$\rho(\delta N_+, \delta N_-)$	$\chi^2_{NDF=197}$	$A_0 \times 100$
$p_T > 25$ GeV					
0.00 – 0.20	1033.0 ± 1.4	764.9 ± 1.2	14.5	255	14.912 ± 0.096
0.20 – 0.40	970.2 ± 1.3	713.9 ± 1.2	14.9	190	15.216 ± 0.098
0.40 – 0.60	1060.3 ± 1.4	771.5 ± 1.2	14.7	220	15.766 ± 0.094
0.60 – 0.80	1055.1 ± 1.4	752.4 ± 1.2	14.6	213	16.745 ± 0.093
0.80 – 1.00	935.8 ± 1.3	652.1 ± 1.1	14.5	245	17.866 ± 0.098
1.00 – 1.20	931.0 ± 1.3	625.4 ± 1.1	13.9	231	19.636 ± 0.099
1.20 – 1.40	949.0 ± 1.3	621.6 ± 1.1	14.2	209	20.848 ± 0.099
1.40 – 1.60	957.1 ± 1.3	607.3 ± 1.1	13.7	202	22.365 ± 0.099
1.60 – 1.85	1131.8 ± 1.4	687.6 ± 1.2	14.7	225	24.417 ± 0.093
1.85 – 2.10	1113.4 ± 1.4	656.8 ± 1.1	12.9	237	25.797 ± 0.094
2.10 – 2.40	843.6 ± 1.2	481.3 ± 1.0	11.8	244	27.341 ± 0.106
$p_T > 35$ GeV					
0.00 – 0.20	574.3 ± 1.0	459.7 ± 0.9	18.9	203	11.083 ± 0.116
0.20 – 0.40	538.9 ± 0.9	428.9 ± 0.9	17.4	202	11.371 ± 0.119
0.40 – 0.60	588.3 ± 1.0	462.8 ± 0.9	18.5	187	11.935 ± 0.114
0.60 – 0.80	582.9 ± 1.0	453.7 ± 0.9	18.7	205	12.472 ± 0.114
0.80 – 1.00	513.7 ± 0.9	392.3 ± 0.8	18.7	218	13.406 ± 0.124
1.00 – 1.20	509.1 ± 0.9	379.2 ± 0.8	15.7	226	14.620 ± 0.121
1.20 – 1.40	520.2 ± 0.9	376.9 ± 0.8	16.2	191	15.970 ± 0.123
1.40 – 1.60	522.7 ± 0.9	370.2 ± 0.8	14.7	195	17.074 ± 0.123
1.60 – 1.85	614.6 ± 1.0	418.8 ± 0.9	17.5	239	18.945 ± 0.118
1.85 – 2.10	604.7 ± 1.0	395.8 ± 0.9	15.0	192	20.885 ± 0.123
2.10 – 2.40	464.3 ± 0.9	288.5 ± 0.8	14.7	234	23.357 ± 0.141

5.5 Systematic uncertainties

In this Section we discuss the systematic uncertainties in the measured muon charge asymmetries. Since the $W^\pm \to \mu^\pm \nu$ signal yields and the asymmetries are extracted by fitting $\not\!\!E_{\mathrm{T}}$ distributions, we consider all systematic sources that

could affect the $\not\!\!E_T$ shapes in the data and in the MC templates. The normalizations of some of the background sources are fixed in the fits. We therefore also study the effect of systematic uncertainties on background source normalization. In addition, we discuss possible sources of bias in the observed charge asymmetries in the selected data sample; and we look at systematic uncertainties associated with the corrections that remove these biases. All values of systematic uncertainties will be summarized in Section 5.5.7.

5.5.1 Muon selection efficiency

The uncertainty of the muon selection efficiency is a dominant source of systematics in both $p_T > 25$ GeV and $p_T > 35$ GeV analyses. The efficiencies are measured using the $Z/\gamma^* \to \mu^+\mu^-$ events in the control sample with the Tag-and-Probe method. The same technique is applied in the data and in the MC simulation.

As described in Section 5.2.4, the measured efficiencies enter the muon charge asymmetry analysis in two ways. First, the extracted raw charge asymmetry is corrected for the difference in selection efficiencies of positive and negative muons using the Eq. 5.3. These correction factors depend only on the ratios $\epsilon^+(\eta)/\epsilon^-(\eta)$. The uncertainties of these ratios are dominated by the statistical uncertainties in the $Z/\gamma^* \to \mu^+\mu^-$ control sample. Second, the normalization of each MC template is corrected for any mis-modeling of the selection efficiencies in the simulation. The potential biases of the charge asymmetries from the two effects are correlated (~70%). However the systematic error of the asymmetry due to the uncertainty of $\epsilon^+(\eta)/\epsilon^-(\eta)$ is about 10 times larger than the error

introduced through the uncertainty of the background normalization.

The systematic error of the measured charge asymmetry in each pseudorapidity bin, resulting from the uncertainties of the muon selection efficiencies, is evaluated as follows. All offline and online selection efficiency values, measured in each $\eta-\phi$ bin, are smeared 400 times within their corresponding statistical uncertainties. The $\epsilon^{+}(\eta)/\epsilon^{-}(\eta)$ values, along with their resulting statistical uncertainties are displayed in Fig. 5.9. In each round, the background normalization and the extracted raw charge asymmetry is corrected using the current set of smeared efficiency values with the procedure, described in Section 5.2.4. In the end, the systematic uncertainty is calculated as a spread (Root Mean Square) of the corrected asymmetry distribution in the 400 pseudo-experiments.

Since the efficiencies are measured in the same muon pseudorapidity bins, the correlations between systematic uncertainties in different $|\eta|$ bins are zero.

5.5.2 Muon momentum

The measurement phase-space in this analysis is defined by the transverse momentum of the muon, $p_T > 25(35)$ GeV. Therefore, the uncertainty of the muon transverse momentum directly affects the yields of the $W^{\pm} \to \mu^{\pm}\nu$ candidates in the selected sample in both, data and simulation. In addition the muon $\vec{p}_T$ is naturally included in the calculation of $\vec{\not{E}}_T$ in all $W^{\pm} \to \mu^{\pm}\nu$ candidate events, therefore its uncertainty also affects the shapes of the $\not{E}_{\mathrm{T}}$ distributions.

To estimate the systematic error of the charge asymmetry in each pseudorapidity bin, the muon correction parameters in each (η, ϕ) bin, described in Sec-

tion 5.2.1, are smeared within their uncertainties 400 times. In each round, the current set of parameters are used consistently to select $W^{\pm} \to \mu^{\pm}\nu$ candidates, correct $\vec{\not{E}}_T$, perform the fits, and extract the final asymmetry. At the end, the systematic uncertainty is calculated as a spread of the result asymmetry distribution in these pseudo-experiments. Since the muon scale corrections are also extracted in the same $|\eta|$ bins, the correlations between the systematic uncertainties in different bins are zero.

While the muon momentum systematics makes a modest contribution to the total uncertainty in $p_T > 25$ GeV analysis, it is one of the dominant systematics sources in $p_T > 35$ GeV analysis (see Tables 5.8 and 5.9). The reason for this is two-fold. First, the uncertainty of the muon momentum itself increases linearly with its momentum. Second, in $p_T > 35$ GeV analysis the cut on the muon p_T is applied close to the Jacobean peak, where a slight uncertainty in the relative p_T calibration for positive and negative muons can translate into a sizeable error in the observed charge asymmetry.

5.5.3 QCD Background

When extracting the $W^+ \to \mu^+\nu$ and $W^- \to \mu^-\nu$ signal yields in each $|\eta|$ bin with the simultaneous fits, the overall QCD normalization is floating, but the ratio $\mathrm{QCD}^+/\mathrm{QCD}^-$ is taken from the control region. To calculate this ratio, we first count the events with positive and negative reconstructed muons in the QCD-enriched data sample. Then we subtract the small contributions (see Fig. 5.17) from $W^{\pm} \to \mu^{\pm}\nu$ events which are evaluated using the MC simulation normalized with the theoretical cross sections to the corresponding integrated lumi-

nosity (0.28 fb^{-1}). In Fig. 5.22, we compare the values in each pseudorapidity bin to ones predicted by the QCD MC simulation in the signal and in the QCD-enriched regions.

To estimate the systematic uncertainty in each pseudorapidity bin, the QCD^+/QCD^- value in the central 10 $|\eta|$ bins is varied by ±5% in the $p_T > 25$ GeV analysis, and by ±15% in the $p_T > 35$ GeV analysis. In the last pseudorapidity bin we vary this ratio by 10% and by 20%, respectively. These variations of the QCD^+/QCD^- ratio span the maximum range indicated by the QCD MC simulation. The uncertainties in different $|\eta|$ bins are assumed to be uncorrelated.

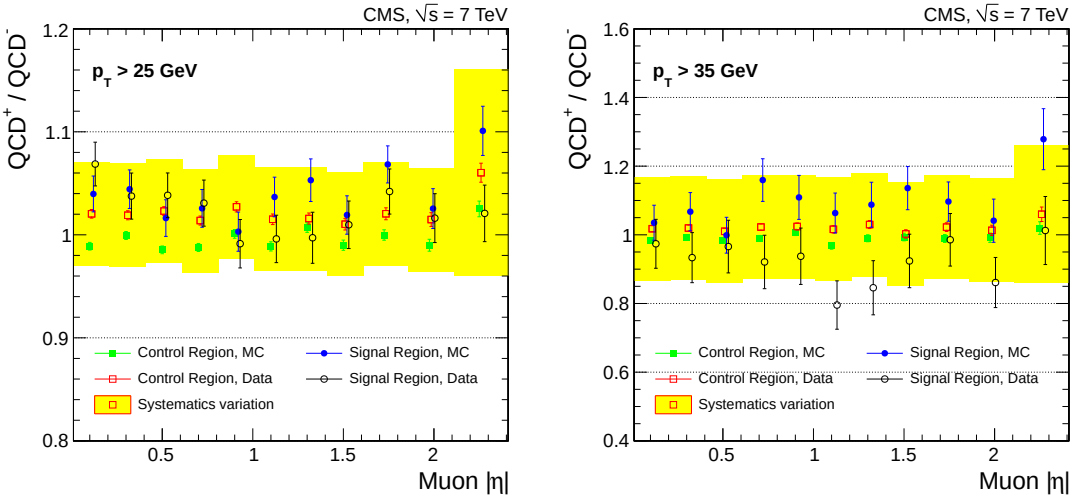

Figure 5.22: Distribution of the QCD^+ / QCD^- ratio in the data and in the simulation in W signal and QCD control regions for $p_T > 25$ GeV (left) and $p_T > 35$ GeV (right) cuts on the muon.

As an additional cross-check, we fit the $\not{E}_T$ distributions in the $W^+ \to \mu^+\nu$ and $W^- \to \mu^-\nu$ events separately. In this case, to reduce statistical fluctuations due to the small size of the simulated QCD sample, we merge the $\not{E}_T$ histograms of the QCD^+ and QCD^- backgrounds and use the same combined QCD template

in both fits. We find that the result QCD^+/QCD^- values are within the variation described above, indicated by the yellow bands in Fig. 5.22.

Another source of systematics, associated with the QCD background, is the mis-modeling of the $\not\!\!E_{\rm T}$ shape in the QCD background templates. As described in Section 5.2.7, the QCD $\not\!\!E_{\rm T}$ shape is derived from the MC simulation and is corrected for the ϕ modulation, the muon momentum bias and the mis-modeling of the hadronic recoil. Two types of variations in the shape of the QCD $\not\!\!E_{\rm T}$ distribution are considered. First, the shape of the QCD $\not\!\!E_{\rm T}$ distribution without the hadronic recoil correction is used in the extraction of the signal. In order to avoid the statistical component in this variation, we fit the ratio of the uncorrected $\not\!\!E_{\rm T}$ distribution to the fully corrected one with $p_0 + p_1 Gaus(0, p_3)$ and use the resulting function to multiply the corrected $\not\!\!E_{\rm T}$ template bin-by-bin, varying the overall shape smoothly. This is done in a correlated way for W^+ and W^- samples.

In addition, we swap the corrected template shapes of the QCD^+ and QCD^- backgrounds in the fits. Here, again, to avoid the statistical component in the variation, we first fit their ratio with a smooth function and use the resulting function and its inverse to effectively swap the overall QCD^+ and QCD^- template shapes.

These two contributions to the systematic uncertainties from the "QCD $\not\!\!E_{\rm T}$" are then added in quadrature. The bin-to-bin correlation of the systematic uncertainties due to each shape variation is assumed to be 100%. In total, the systematic uncertainties of the QCD background are comparable to the uncertainties in the muon selection efficiencies.

5.5.4 Final State Radiation

FSR refers to the radiation of a photon by the final state muon produced in the W boson decay. This radiation, on average, tends to reduce the muon p_T. Therefore, muons before FSR have a higher p_T spectrum than muons after FSR. Since the p_T distribution of positive and negative muons in $W^{\pm} \to \mu^{\pm}\nu$ events is not identical, the $p_T > p_T^{min}$ cut on the muons before and after FSR can result in different charge asymmetry values.

The effect of FSR is estimated with our signal POWHEG MC sample, which is interfaced with PYTHIA for parton showering and hadronization. Photon irradiation by the muons in this framework is implemented in the same way as parton showering. We calculate the muon charge asymmetry in each pseudorapidity bin by applying the $p_T > 25$ (35) GeV cut on the generated muons either before or after they radiate the photon. The difference between the two values varies within 0.07–0.12% for the $p_T > 25$ GeV cut and within 0.03–0.11% for the $p_T > 35$ GeV cut across different $|\eta|$ bins.

For this measurement the central values are not corrected for the FSR effect. However, the full shift predicted by the POWHEG MC is taken as an additional systematic uncertainty, and the bin-to-bin correlations are assumed to be 100%. The FSR effect is small compared to other systematic uncertainties.

5.5.5 Parton Distribution Functions

We follow the PDF4LHC recommendation [25] in evaluating systematic uncertainties that originate from uncertainties in the PDFs. The NLO MSTW2008,

CT10, and NNPDF2.1 PDF sets are used. All simulated events are re-weighted to a given PDF set and the overall normalization is allowed to vary. Different PDF sets predict different Z rapidity shapes, resulting in different normalizations of the $Z/\gamma^* \to \mu^+\mu^-$ background in each pseudorapidity bin. The PDFs also affect the ratio of $W^\pm \to \mu^\pm\nu$ and $W^\pm \to \tau^\pm\nu$ yields in the signal region, defined by the muon p_T cut. The shapes of the $\not\!\!E_{\mathrm{T}}$ distribution corresponding to different PDF sets are also slightly different.

Asymmetry values corresponding to each error-member of each PDF set are used to evaluate the systematic uncertainties. For the CT10 and MSTW PDF sets, we use asymmetric master Eqs. 2.11. For the NNPDF set, we take the RMS of the asymmetry distribution over 100 replicas as the the systematic uncertainty. For CT10, we scale the uncertainties evaluated for a 90% confidence level (C.L.) down to a 68% C.L. by a factor of 1.64485.

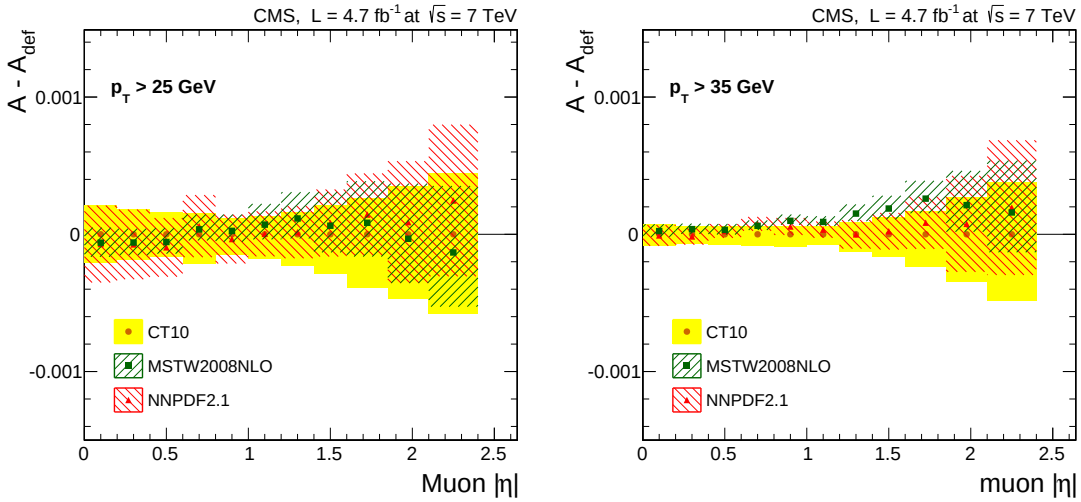

Figure 5.23: PDF systematic bands corresponding to three PDF sets for $p_T > 25$ GeV (left) and $p_T > 35$ GeV (right) analyses. The error bands of the NNPDF and MSTW sets in each $|\eta|$ bin are shifted by the difference between their central predictions and the central prediction of the CT10 set.

Error bands corresponding to three PDF sets are depicted in Fig. 5.23. We take the half-width of the total envelope as the total PDF uncertainty. Since variations of the central values corresponding to the three PDF sets are negligible, the central asymmetry values are not modified. The bin-to-bin correlations are evaluated using the CT10 error set.

5.5.6 Other systematic sources

In this Section we review other sources of systematics found to have small or negligible contributions to the total systematic uncertainty. Unless specified otherwise, each systematic uncertainty is evaluated by taking the deviation (or maximum deviation) from the default asymmetry value as we vary the corresponding source of the systematics. The bin-to-bin correlations are ±100%. The sign of the correlation for a given systematic source between the uncertainties in two bins is positive (negative) if the asymmetries shift in the same (opposite) directions for the corresponding variation.

Pileup

Additional proton-proton interactions in the event affect the resolution of $\not\!\!E_{\mathrm{T}}$. To estimate the corresponding uncertainty, we follow the standard procedure employed in CMS, and vary the minimum bias cross section by ±5%. For each variation we generate a new pileup distribution in data and redo the pileup re-weighting. This variation takes into account all the effects of the mis-modeling the pileup, including the uncertainty of the pileup distribution and mis-modeling of the physics content in each minimum-bias interaction. Pileup

affects the $\not\!\!E_{\mathrm{T}}$ shapes coherently in all pseudorapidity bins, therefore the bin-to-bin correlations are 100%.

Recoil and ϕ-modulation corrections

The hadronic recoil correction affects the shape of the $\not\!\!E_{\mathrm{T}}$ distribution in all MC samples. To calculate the systematic uncertainties in this source, the average recoil and resolution parameters are smeared within their uncertainties, taking into account the correlations between them. This procedure is repeated 400 times and the RMS of the resulting asymmetry distribution is taken as a systematic uncertainty.

To evaluate systematic uncertainty due to ϕ-modulation of $\vec{\not\!\!E}_T$, the correction for ϕ-modulation is removed and the shift in the extracted charge asymmetry is taken as a systematic uncertainty.

Electroweak background normalization

As described in Section 5.2.6, we apply residual mass-dependent k-factors to the $Z/\gamma^* \to \mu^+\mu^-$ background. To estimate the systematics, we remove these residual corrections and redo the fits.

The $W^\pm \to \tau^\pm\nu$ background is normalized to the $W^\pm \to \mu^\pm\nu$ yields in data with a ratio obtained from an MC simulation. This ratio is largely determined by the branching fraction of τ decaying to μ. A 2% uncertainty is assigned to the $W^\pm \to \tau^\pm\nu$ to $W^\pm \to \mu^\pm\nu$ ratio [14].

We use the integrated luminosity to normalize the EWK and $t\bar{t}$ samples. To

estimate the systematic uncertainty, the luminosity is varied by ±2.2%. To be on the conservative side, $Z/\gamma^* \to \mu^+\mu^-$ background normalization is also allowed to vary with the luminosity[5].

The $t\bar{t}$ sample is normalized to the integrated luminosity using the theoretical cross section. Its normalization is additionally varied by ±15% to take into account the uncertainty of the cross section.

Modeling of the W transverse momentum

To improve the agreement between the data and the simulation, the boson p_T spectrum is reweighted using weight factors that are the ratios of the distribution of boson p_T for the $Z/\gamma^* \to \mu^+\mu^-$ events in the data and in the MC simulation. In doing so, we have made the assumption that the scale factors to correct the boson p_T distribution in MC simulation to match the data are the same for W and Z events. This assumption is tested using two different sets of MC simulations: one from the POWHEG event generator and the other from MADGRAPH [63]. Here, the MADGRAPH simulation is treated as "data", and the ratio of Z boson p_T between the MADGRAPH simulation and the POWHEG simulation is compared to the same ratio in simulated W events. This double ratio is parameterized using an empirical function to smooth the statistical fluctuations, and additional weights are obtained using the fitted function. These additional factors are used to reweight the POWHEG W events, and the deviation of the result asymmetries from the default value is taken as the systematic uncertainty.

[5]Although there is double-counting in the variation of the overall normalization from the mass-dependent k-factors, luminosity and PDFs, since all these systematics are small we can afford to stay on the conservative side.

Muon charge mis-identification

Bias in the measured charge asymmetry can be introduced by an incorrect measurement of the muon charge. A charge mis-identification rate w would dilute the asymmetry by a factor of $(1 - 2w)$. The muon charge mis-identification rate has been studied in detail previously and was found to have a negligible effect on the muon charge asymmetry [31].

5.5.7 Summary of systematic uncertainties

Tables 5.8 and 5.9 show the summary of various systematic uncertainties in the muon charge asymmetry measurement for $p_T > 25$ GeV and $p_T > 35$ GeV analyses, respectively. The total systematic error is calculated by adding contributions from all systematics sources in quadrature. Similarly, the total uncertainty is calculated by adding the statistical and the total systematic errors in quadrature. Contributions from statistical and dominant systematic sources to the total uncertainties are illustrated in Fig. 5.24.

For $p_T > 25$ GeV analysis, the systematic uncertainty is dominated by the muon efficiency and the QCD. For the $p_T > 35$ GeV analysis, the uncertainty of the muon momentum scale also adds a significant contribution. As one can also see from the figure, uncertainties from the PDFs are rather small in both cases, meaning that the result of the muon charge asymmetry measurement is not sensitive to which PDF set is used to model the MC signal and background samples. This fact is crucial to our analysis, since the main purpose of the muon charge asymmetry measurement is to constrain uncertainties in the PDFs.

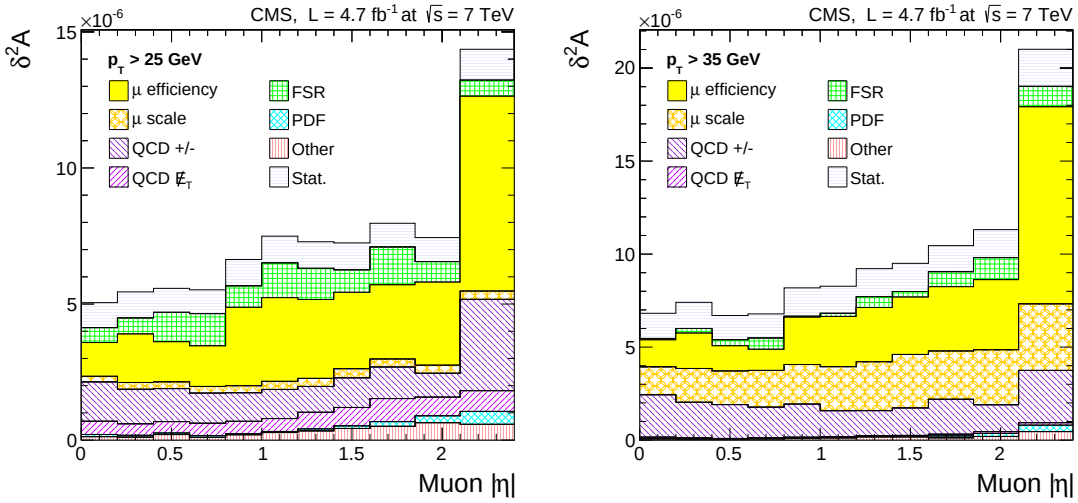

Figure 5.24: The dominant systematic and statistical contributions to the total uncertainty in $p_T > 25$ GeV (left) and $p_T > 35$ GeV analysis (right). On the vertical axis $\delta^2\mathcal{A}$ is the square of the uncertainty. All contributions to the total $\delta^2\mathcal{A}$ are stacked.

The total correlation matrix of systematic uncertainties is shown in Table 5.10. Since the dominant systematic sources are uncorrelated between the different bins, the total bin-to-bin correlations are also small. The maximum correlation factors in the $p_T > 25$ GeV and $p_T > 35$ GeV analyses are about 30% and 15%, respectively. The dominant sources of the correlations are the uncertainties of the QCD $\not\!\!E_T$ shape and the FSR.

5.6 Results and discussion

In this Section we discuss the results of the muon charge asymmetry measurement and their implications. We first check the robustness of the results by comparing the two independent measurements in the positive and negative η sides of the detector. We will also compare the two measurements using two

Table 5.8: Systematic uncertainties in 11 $|\eta|$ bins for $p_T > 25$ GeV. The units are in 10^{-5}.

$\|\eta\|$ bin	0.00 – 0.20	0.20 – 0.40	0.40 – 0.60	0.60 – 0.80	0.80 – 1.00	1.00 – 1.20	1.20 – 1.40	1.40 – 1.60	1.60 – 1.85	1.85 – 2.10	2.10 – 2.40
Stat. unc.	96	98	94	93	98	99	99	99	93	94	106
$\mu^{\pm}$ efficiency	111	133	121	122	170	175	170	168	165	175	268
QCD +/-	120	113	110	105	102	103	97	104	108	94	183
QCD $\not{E}_{\mathrm{T}}$	70	65	65	67	68	69	78	82	92	83	87
$p_T(\mu^{\pm})$	45	50	50	49	51	54	54	58	54	54	55
FSR	74	77	104	109	89	113	107	91	118	87	77
PDF	28	26	23	25	18	20	27	31	42	50	69
$W^{\pm} \to \tau^{\pm}\nu$	26	26	26	26	26	25	25	25	25	25	24
$t\bar{t}$	12	13	12	12	11	11	10	9	8	7	5
$Z/\gamma^* \to \mu\mu$	2	1	2	3	0	7	1	13	19	38	46
L_{int}	2	3	4	4	6	9	12	17	24	33	40
$\phi(\vec{\not{E}}_T)$	11	9	33	12	29	34	44	45	55	49	38
Pileup	17	13	11	5	14	25	22	31	19	28	0
Recoil	3	3	3	3	3	3	3	3	3	4	3
$p_T(W)$	3	4	4	5	8	11	8	9	6	3	0
Total sys.	203	212	217	216	238	255	251	250	266	256	364
Total unc.	225	233	236	235	258	274	270	269	282	273	379

statistically independent data samples, corresponding to the 2011A and 2011B data collection periods.

The final muon charge asymmetry results will be compared with the previous CMS measurements of muon and electron charge asymmetries. We will then discuss the consistency of the results with various theoretical calculations using different PDF models.

Finally, we will present the first QCD analysis of the impact of the muon charge asymmetry results on HERA PDFs .

Table 5.9: Systematic uncertainties in 11 $|\eta|$ bins for $p_T > 35$ GeV. The units are in 10^{-5}.

$\|\eta\|$ bin	0.00 – 0.20	0.20 – 0.40	0.40 – 0.60	0.60 – 0.80	0.80 – 1.00	1.00 – 1.20	1.20 – 1.40	1.40 – 1.60	1.60 – 1.85	1.85 – 2.10	2.10 – 2.40
Stat. unc.	116	119	114	114	124	121	123	123	118	123	141
$\mu^{\pm}$ efficiency	120	138	116	107	159	164	171	176	186	194	325
QCD +/-	151	138	135	128	133	118	116	122	137	120	168
QCD $\not\!\!E_{\mathrm{T}}$	30	25	17	23	24	22	18	17	31	31	37
$p_T(\mu^{\pm})$	122	135	134	141	146	154	162	170	161	172	189
FSR	28	50	57	78	22	41	76	55	90	109	105
PDF	8	8	7	11	12	10	17	22	31	40	58
$W^{\pm} \to \tau^{\pm}\nu$	13	12	13	12	12	12	11	12	11	11	11
$t\bar{t}$	11	13	12	11	11	10	10	9	7	6	5
$Z/\gamma^* \to \mu\mu$	10	9	9	3	6	10	8	9	9	20	40
L_{int}	1	2	0	0	0	1	4	10	16	25	39
$\phi(\vec{\not\!\!E}_T)$	2	9	10	3	8	28	37	35	22	22	1
Pileup	15	3	5	18	19	2	7	3	13	14	32
Recoil	5	6	5	4	5	4	5	4	4	6	8
$p_T(W)$	4	2	4	4	7	5	6	9	9	1	14
Total sys.	234	245	232	234	258	261	278	283	301	313	436
Total unc.	261	272	259	260	286	288	304	308	323	336	458

5.6.1 Charge asymmetry without η symmetry imposed

The muon charge asymmetry in $pp \to W$ production must be symmetric for the two η sides of the detector: $A(\eta) = A(-\eta)$. As a first cross-check, we perform the muon charge asymmetry measurement in 22 η bins instead of 11.

The $\epsilon^+(\eta)/\epsilon^-(\eta)$ ratio, measured from the $Z/\gamma^* \to \mu^+\mu^-$ events, differs from unity in certain regions of the detector. These deviations are not, in general, equal for $+\eta$ and $-\eta$ bins. Therefore, this cross-check provides an important test

Table 5.10: Correlation matrix of systematic uncertainties between different $|\eta|$ bins. The units are in percent.

$\|\eta\|$ bin	0.00 – 0.20	0.20 – 0.40	0.40 – 0.60	0.60 – 0.80	0.80 – 1.00	1.00 – 1.20	1.20 – 1.40	1.40 – 1.60	1.60 – 1.85	1.85 – 2.10	2.10 – 2.40
$p_T > 25$ GeV											
0.00 – 0.20	100	28.1	32.4	32.9	27.1	29.0	29.5	28.0	30.5	26.1	16.7
0.20 – 0.40		100	30.7	31.4	25.6	27.5	27.9	26.3	28.9	24.5	15.8
0.40 – 0.60			100	37.4	30.9	33.8	34.5	32.1	36.1	30.3	19.3
0.60 – 0.80				100	31.1	34.0	34.4	32.0	36.3	30.4	20.0
0.80 – 1.00					100	28.5	29.5	28.0	31.2	26.9	17.3
1.00 – 1.20						100	32.6	31.1	34.8	30.2	19.3
1.20 – 1.40							100	32.8	36.9	32.2	20.8
1.40 – 1.60								100	36.0	32.7	21.3
1.60 – 1.85									100	37.1	24.9
1.85 – 2.10										100	24.4
2.10 – 2.40											100
$p_T > 35$ GeV											
0.00 – 0.20	100	4.6	4.8	6.4	3.4	3.6	4.7	3.4	5.4	5.8	4.3
0.20 – 0.40		100	6.4	8.5	3.3	4.3	6.3	4.4	7.2	8.0	5.8
0.40 – 0.60			100	9.8	3.8	5.6	8.4	6.2	8.9	9.9	6.6
0.60 – 0.80				100	5.1	6.9	10.7	7.8	11.9	13.5	9.7
0.80 – 1.00					100	3.2	4.2	3.3	4.7	5.0	3.6
1.00 – 1.20						100	7.0	5.4	7.0	7.5	4.7
1.20 – 1.40							100	8.1	10.8	12.0	7.8
1.40 – 1.60								100	8.8	9.9	6.7
1.60 – 1.85									100	14.2	10.3
1.85 – 2.10										100	12.6
2.10 – 2.40											100

for the corrections that we apply to remove the bias due to differences in the selection efficiencies of positive and negative muons.

Figure 5.25 depicts the comparison of raw and corrected muon charge asym-

metries between positive and negative η sides. As one can see, the $\epsilon^+(\eta)/\epsilon^-(\eta)$-correction brings the asymmetry values in positive and negative η bins into agreement within their uncertainties.

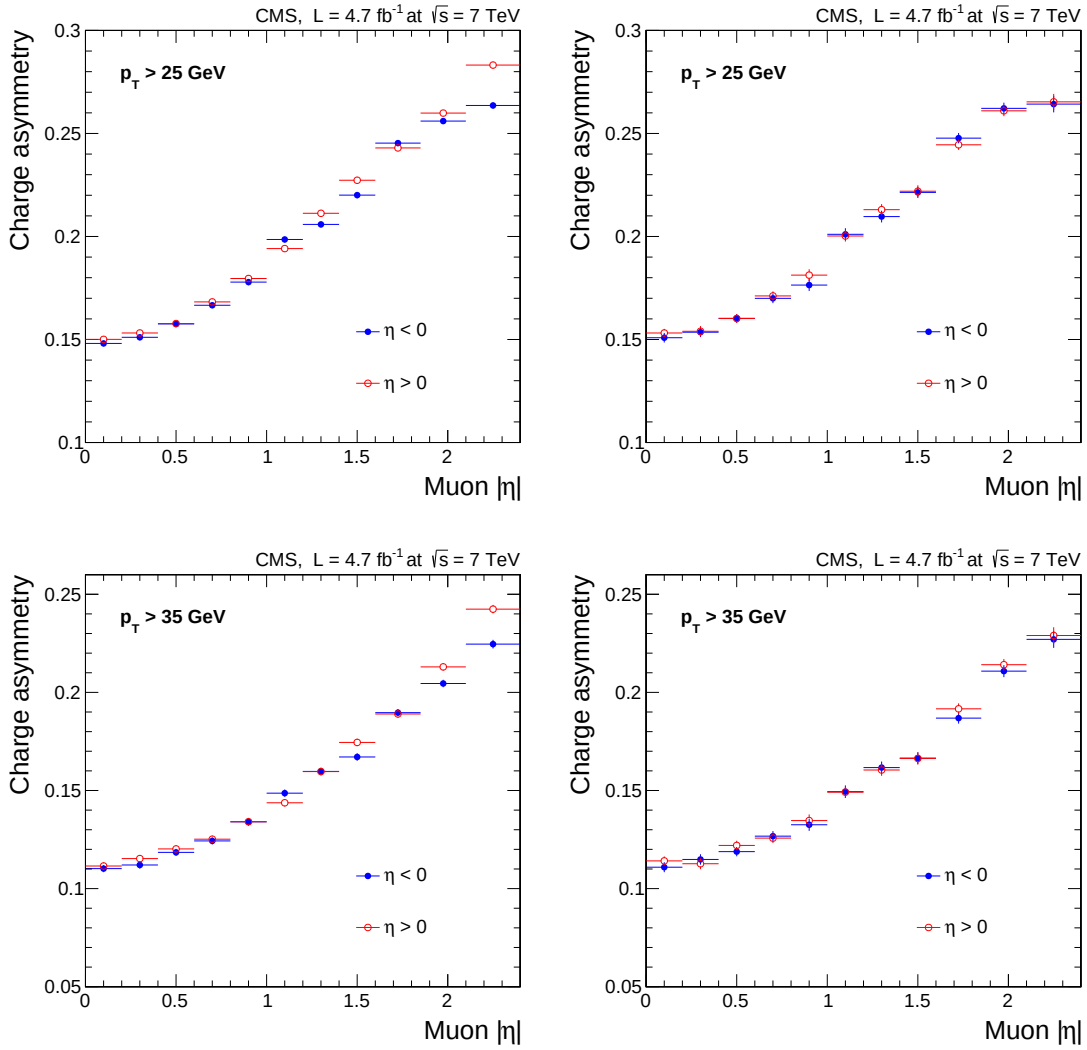

Figure 5.25: The raw (left) and corrected (right) muon charge asymmetry in positive (solid circle) and negative (open circle) η regions in $p_T > 25$ GeV (top) and $p_T > 35$ GeV (bottom) analysis. The uncertainties of the left figures are only statistical. The uncertainties of the right figures include the uncertainty of the $\epsilon^+(\eta)/\epsilon^-(\eta)$ ratio.

5.6.2 Charge asymmetry in 2011A and 2011B

Here we compare the muon charge asymmetry measurements using two statistically independent data samples: 2011A and 2011B, which correspond to integrated luminosities of 2.3 fb^{-1} and 2.4 fb^{-1}, respectively.

Various conditions, including detector alignment and the online trigger parameters, changed during the two data collection periods. Therefore, both the muon momentum correction parameters and the efficiency tables are measured separately, once for each of the two datasets. Instantaneous luminosity also increased during the 2011 data collection period, so the pileup values in 2011B are larger than those in 2011A (Fig. 5.2). Therefore, the $\vec{\not{E}}_T$ correction parameters are also separately derived for the two datasets. Correspondingly, all the MC templates are split into two parts. In each part, the pileup distribution is matched to either the 2011A or the 2011B dataset, as appropriate.

Figure 5.26 shows a comparison between the muon charge asymmetries measured in the 2011A and 2011B datasets. As one can see, the corresponding asymmetry values are within their uncertainties both before and after the $\epsilon^+(\eta)/\epsilon^-(\eta)$ corrections are applied. This implies that the ratio of positive and negative muon selection efficiencies is not very different in the two datasets. However, since the efficiencies are measured using the $Z/\gamma^* \to \mu^+\mu^-$ control sample, with 10 times less number of events than the $W \to \mu\nu$ signal sample, the fluctuations in the corrected asymmetry values are larger than the raw ones (although they are within their corresponding statistical uncertainties).

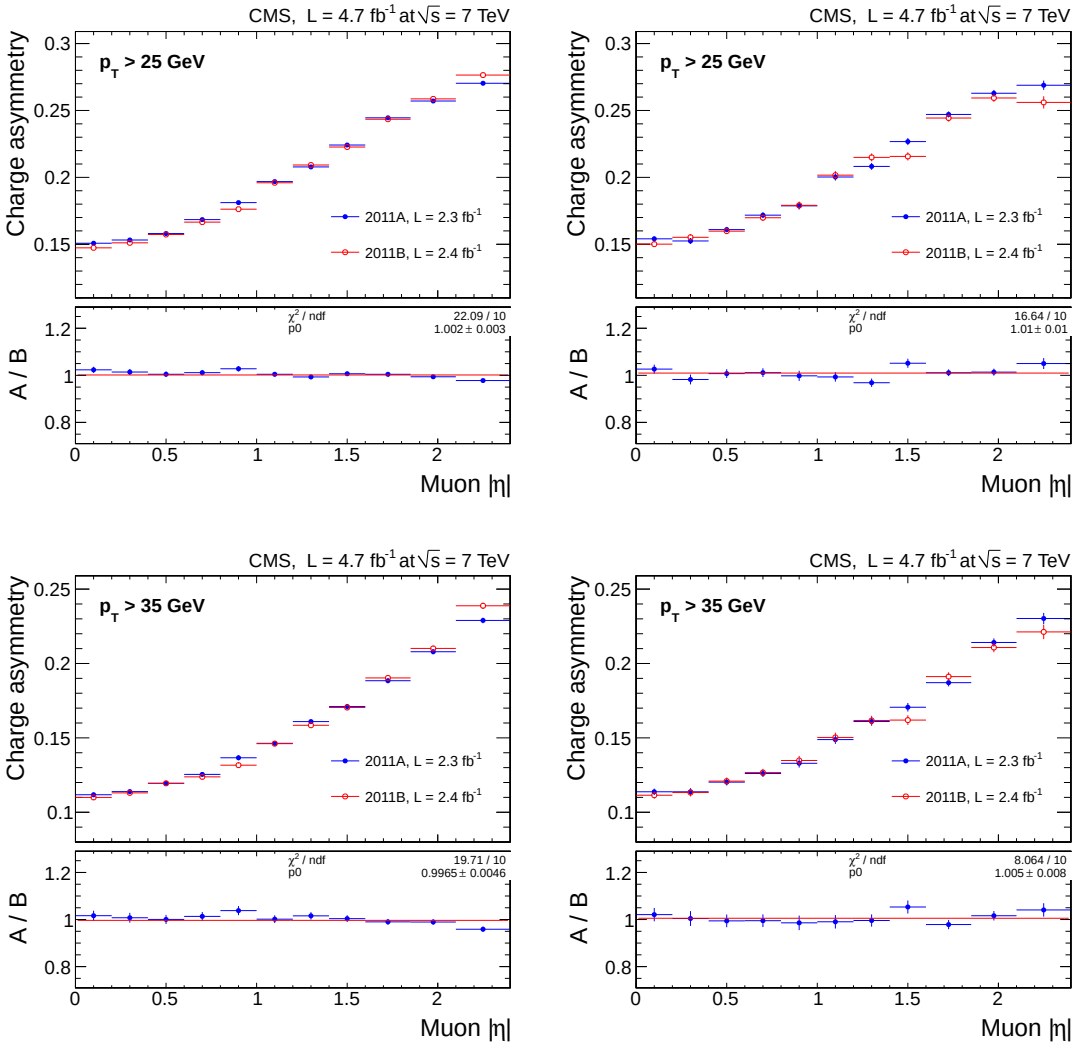

Figure 5.26: The raw (left) and corrected (right) muon charge asymmetry, measured with 2011A (solid circles) and 2011B (open circles) datasets, in $p_T > 25$ GeV (top) and $p_T > 35$ GeV (bottom) analysis. The uncertainties of the left figures are only statistical. The uncertainties of the right figures include the uncertainty of the $\epsilon^+(\eta)/\epsilon^-(\eta)$ ratio. The bottom panel of each plot shows the ratio $A(2011A)/A(2011B)$, fitted with the constant function.

5.6.3 Comparison with previous CMS measurements

Figure 5.27 shows the comparison of our muon charge asymmetry result with previous CMS lepton charge asymmetry measurements, as discussed in Section 2.5. For most of the data points the agreement is within one standard derivation.

In previous muon charge asymmetry analysis, the central A_{raw} values are not corrected for differences in the selection efficiencies for positive and negative muons; but the statistical uncertainty of $\epsilon^+(\eta)/\epsilon^-(\eta)$ is included in the total systematic error. Assuming the ϵ^+/ϵ^- ratios are the same in the first 0.234 fb^{-1} data as what we measured in the full 2011 dataset (Fig. 5.9), the $\epsilon^+(\eta)/\epsilon^-(\eta)$ correction can account for about a half of the observed overall shift. One should also note that the detector alignment corrections were significantly worse in the data sample used in the previous measurement, and hence, large residual corrections for the muon momentum were needed. The data sample used in the previous muon charge asymmetry measurement is included in the dataset used here. Therefore, our result supersedes the previous measurement.

The data samples used in our measurement and in the previous electron charge asymmetry measurements are statistically independent. Combining the results of the two measurements can potentially improve the constraints in global PDF fits. The correlation between uncertainties in the electron charge asymmetry and our measurement is small. The completely correlated systematic sources of error include the luminosity measurement, $t\bar{t}$ background, $W^{\pm} \to \tau^{\pm}\nu$ background, and the PDF uncertainty.

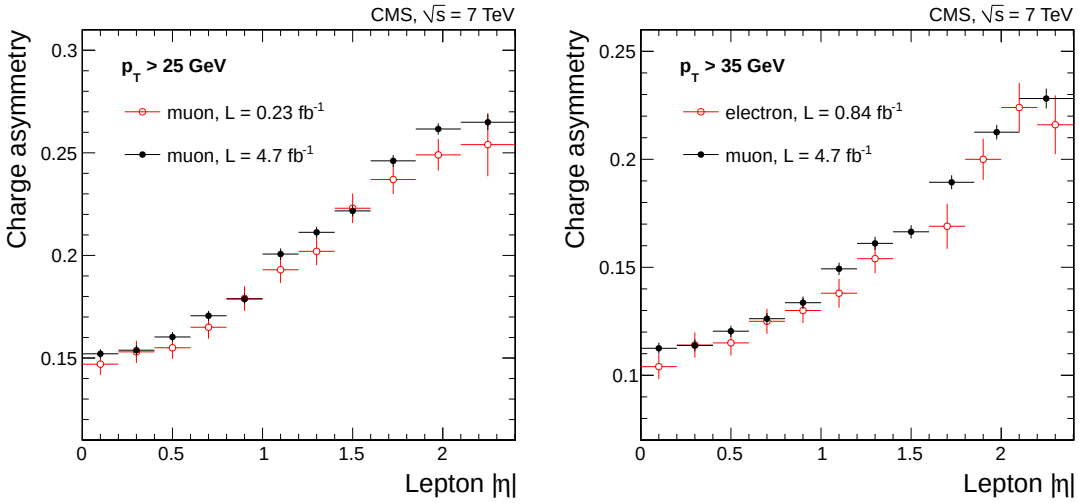

Figure 5.27: Comparison of our muon charge asymmetry results with previous CMS measurements of muon (left) and electron (right) charge asymmetries.

5.6.4 Comparison with theoretical predictions

We compare the measured muon charge asymmetry values in each pseudorapidity bin with theoretical calculations. The theoretical predictions are obtained using the NLO FEWZ 3.1 MC tool, interfaced with the CT10, NNPDF2.3, HERAPDF1.5, MSTW2008, and MSTW20008CPDeout PDF models. The FEWZ configuration parameters are summarized in Table 5.11.

Theoretical errors, corresponding to the uncertainties in the MSTW and the CT10 PDF models, are evaluated with the asymmetric master Eqs. 2.11. CT10 errors are divided by 1.64485 to scale the uncertainties at 90% C.L down to 68% C.L. For the NNPDF set, uncertainty in each bin is calculated as a RMS of the asymmetry distribution over 100 PDF error replicas.

The HERA PDF set constructs the full uncertainty as a combination of ex-

Table 5.11: FEWZ 3.1 configuration parameters.

$\sqrt{s}$ of pp collisions	7 TeV
μ_F, μ_R	80.403 GeV
Alpha QED	0.0078125
Fermi constant	0.0000116637 GeV^{-2}
W mass	80.403 GeV
W width	2.141 GeV
$W \to l\nu$ partial width	0.2263
$\sin^2\theta_W$	0.22255
(V_{ud}, V_{us}, V_{ub})	(0.97428, 0.22530, 0.00347)
(V_{cd}, V_{cs}, V_{cb})	(0.22530, 0.97345, 0.04100)
QCD perturbation order	NLO (NNLO)
Muon p_T threshold	25 (35) GeV
PDF sets	CT10, NNPDF2.3, HERA1.5, MSTW2008, MSTW2008CPdeut

perimental, modeling, and parameterization uncertainties [23]. To evaluate the experimental part, the symmetric master Eq. 2.10 is used. Modeling and parameterization uncertainties are also evaluated as described in [23]. The total uncertainties are calculated by summing the three contributions in quadrature.

The numerical values of the theoretical predictions and measured asymmetries are shown in Table 5.12. The corresponding distributions are displayed in Fig. 5.28. The theoretical predictions with CT10, NNPDF2.3, and HERAPDF1.5 PDF models are in good agreement with the data. The data set used to obtain the NNPDF2.3 PDF model includes the previous CMS electron charge asymmetry and other LHC results. The old MSTW2008 PDF model poorly describes the asymmetry results measured by CMS. The more recent model of the same group, MSTW20008CPDeout [64], uses more flexible parameterization of PDFs, which results in much better agreement between the theoretical predictions and

the data[6]. The agreement between the measured asymmetry values and the theoretical calculations is quantified with a χ^2 test in Table 5.13.

Table 5.12: Summary of the final results for muon charge asymmetry $\mathcal{A}$. Theoretical predictions are obtained using the NLO FEWZ 3.1 MC tool interfaced with the NLO CT10, NNPDF2.3, HERA-PDF1.5, and MSTW2008CPDEUT PDF models. The PDF uncertainty is at the 68% C.L. All units are in percent.

$\lvert\eta\rvert$ bin	$\mathcal{A}$ (±stat.±sys.)	CT10	NNPDF	HERA	MSTW
		$p_T > 25$ GeV			
0.00 – 0.20	$15.21 \pm 0.10 \pm 0.20$	$15.35^{+0.74}_{-0.68}$	14.94 ± 0.39	$15.33^{+0.30}_{-0.84}$	$14.34^{+0.75}_{-0.69}$
0.20 – 0.40	$15.38 \pm 0.10 \pm 0.21$	$15.63^{+0.73}_{-0.69}$	15.16 ± 0.37	$15.58^{+0.32}_{-0.85}$	$14.67^{+0.75}_{-0.69}$
0.40 – 0.60	$16.03 \pm 0.09 \pm 0.22$	$16.27^{+0.71}_{-0.70}$	15.90 ± 0.36	$16.16^{+0.34}_{-0.88}$	$15.27^{+0.75}_{-0.70}$
0.60 – 0.80	$17.06 \pm 0.09 \pm 0.22$	$17.27^{+0.68}_{-0.71}$	16.71 ± 0.34	$16.98^{+0.37}_{-0.91}$	$16.19^{+0.74}_{-0.71}$
0.80 – 1.00	$17.88 \pm 0.10 \pm 0.24$	$18.45^{+0.66}_{-0.74}$	17.99 ± 0.33	$17.98^{+0.42}_{-0.94}$	$17.33^{+0.74}_{-0.73}$
1.00 – 1.20	$20.07 \pm 0.10 \pm 0.26$	$19.85^{+0.64}_{-0.76}$	19.46 ± 0.33	$19.25^{+0.48}_{-0.95}$	$18.74^{+0.73}_{-0.74}$
1.20 – 1.40	$21.13 \pm 0.10 \pm 0.25$	$21.50^{+0.63}_{-0.80}$	21.03 ± 0.33	$20.51^{+0.54}_{-0.92}$	$20.45^{+0.72}_{-0.76}$
1.40 – 1.60	$22.17 \pm 0.10 \pm 0.25$	$23.13^{+0.64}_{-0.84}$	22.66 ± 0.34	$21.92^{+0.59}_{-0.84}$	$22.12^{+0.70}_{-0.78}$
1.60 – 1.85	$24.61 \pm 0.09 \pm 0.27$	$24.87^{+0.65}_{-0.89}$	24.49 ± 0.35	$23.32^{+0.63}_{-0.70}$	$24.01^{+0.68}_{-0.79}$
1.85 – 2.10	$26.16 \pm 0.09 \pm 0.26$	$26.42^{+0.67}_{-0.95}$	25.88 ± 0.38	$24.70^{+0.65}_{-0.57}$	$25.70^{+0.65}_{-0.81}$
2.10 – 2.40	$26.49 \pm 0.11 \pm 0.36$	$27.13^{+0.74}_{-1.03}$	26.46 ± 0.42	$25.40^{+0.81}_{-0.48}$	$26.48^{+0.65}_{-0.87}$
		$p_T > 35$ GeV			
0.00 – 0.20	$11.25 \pm 0.12 \pm 0.23$	$11.00^{+0.52}_{-0.48}$	10.68 ± 0.37	$10.80^{+0.32}_{-0.76}$	$10.39^{+0.67}_{-0.67}$
0.20 – 0.40	$11.38 \pm 0.12 \pm 0.24$	$11.36^{+0.52}_{-0.49}$	10.91 ± 0.33	$11.07^{+0.33}_{-0.77}$	$10.61^{+0.68}_{-0.68}$
0.40 – 0.60	$12.04 \pm 0.11 \pm 0.23$	$11.80^{+0.52}_{-0.50}$	11.40 ± 0.31	$11.51^{+0.34}_{-0.79}$	$11.10^{+0.70}_{-0.69}$
0.60 – 0.80	$12.62 \pm 0.11 \pm 0.23$	$12.59^{+0.53}_{-0.53}$	12.18 ± 0.33	$12.17^{+0.36}_{-0.80}$	$11.71^{+0.72}_{-0.71}$
0.80 – 1.00	$13.36 \pm 0.12 \pm 0.26$	$13.60^{+0.55}_{-0.58}$	13.21 ± 0.35	$13.02^{+0.37}_{-0.82}$	$12.70^{+0.74}_{-0.74}$
1.00 – 1.20	$14.93 \pm 0.12 \pm 0.26$	$14.79^{+0.59}_{-0.64}$	14.24 ± 0.36	$14.10^{+0.40}_{-0.81}$	$13.75^{+0.77}_{-0.77}$
1.20 – 1.40	$16.11 \pm 0.12 \pm 0.28$	$16.14^{+0.64}_{-0.73}$	15.65 ± 0.36	$15.31^{+0.41}_{-0.77}$	$15.24^{+0.79}_{-0.79}$
1.40 – 1.60	$16.64 \pm 0.12 \pm 0.28$	$17.72^{+0.70}_{-0.83}$	17.11 ± 0.36	$16.68^{+0.40}_{-0.68}$	$16.69^{+0.79}_{-0.82}$
1.60 – 1.85	$18.94 \pm 0.12 \pm 0.30$	$19.53^{+0.77}_{-0.94}$	18.87 ± 0.36	$18.22^{+0.40}_{-0.51}$	$18.62^{+0.77}_{-0.86}$
1.85 – 2.10	$21.26 \pm 0.12 \pm 0.31$	$21.52^{+0.82}_{-1.06}$	20.89 ± 0.38	$20.15^{+0.41}_{-0.32}$	$20.71^{+0.71}_{-0.90}$
2.10 – 2.40	$22.81 \pm 0.14 \pm 0.44$	$23.53^{+0.86}_{-1.17}$	22.73 ± 0.42	$22.17^{+0.71}_{-0.33}$	$22.79^{+0.66}_{-0.99}$

[6]It should be noted that the CMS asymmetry results are not used in the QCD analysis to obtain the parameters in the MSTW20008CPDeout PDF model.

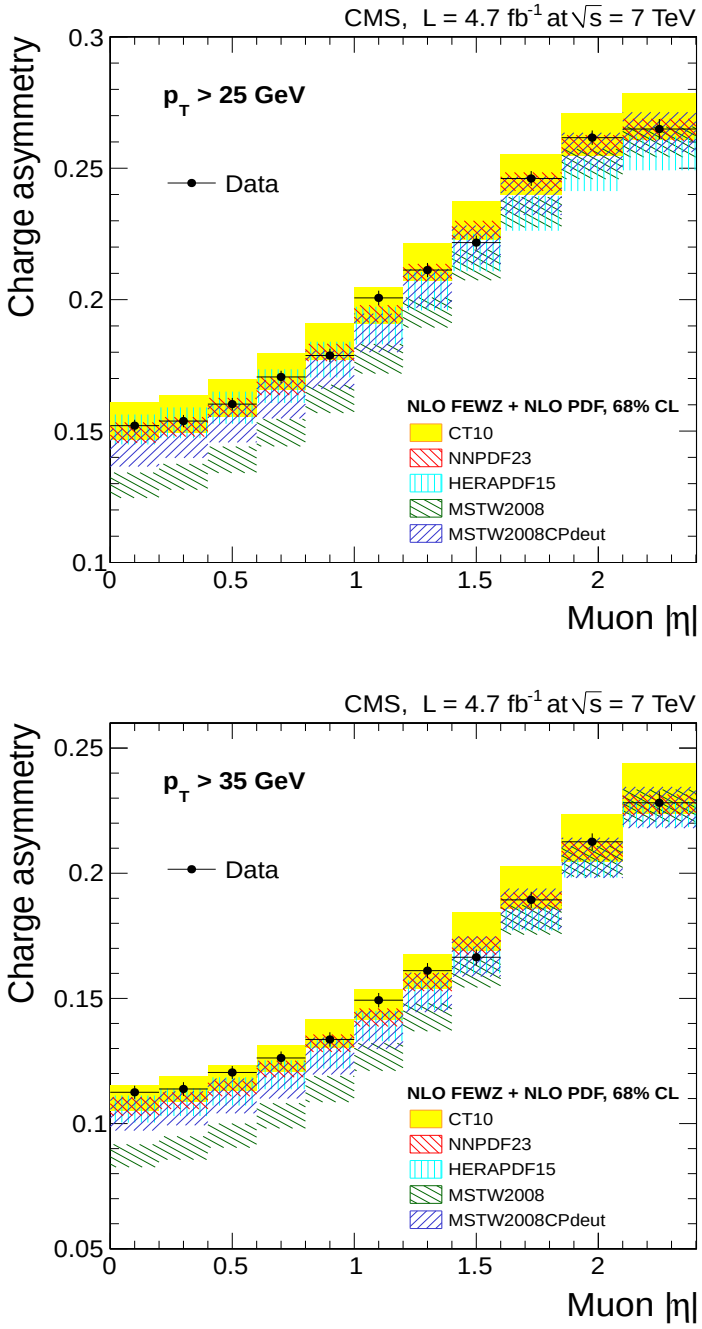

Figure 5.28: Comparison of measured muon charge asymmetries to theoretical predictions with the NLO CT10, NNPDF2.3, HERAPDF1.5, MSTW2008, and MSTW2008CPDEUT PDF models. The results for muon $p_T > 25$ GeV and $p_T > 35$ GeV are shown. The error bands on the data points include the statistical and systematic uncertainties. The PDF uncertainty band for theoretical predictions corresponds to the 68% confidence level. The theoretical predictions are calculated using the FEWZ 3.1 MC tool.

Table 5.13: χ^2 test for the measured asymmetries and the theoretical calculations using four different PDF models. Only the experimental covariance matrix is used in the χ^2 calculation.

	χ^2 (NDF = 11)	
PDF Set	$p_T > 25$ GeV	$p_T > 35$ GeV
CT10	21	21
NNPDF2.3	16	25
MSTW2008CPDEUT	43	63
HERAPDF1.5	64	34

Since the total experimental uncertainties of the measured asymmetries are significantly smaller than the uncertainties of the theoretical predictions for each PDF model, the measurement we have laid out in this paper can be used to constrain the parameters in the next generation of PDF sets.

Theoretical predictions for lepton charge asymmetry are given for the kinematic region specified by the lepton p_T threshold. Acceptance is affected by the modeling of the W boson p_T. However, the effects on W^+ and W^- are largely correlated. Therefore, the impact on lepton charge asymmetry cancels to first order. Figure 5.29 shows a comparison of measured charge asymmetries from NLO CT10 predictions based on FEWZ and RESBOS [65, 66, 67]. RESBOS does a resummation of soft gluon radiation at an approximate next-to-next-to-leading logarithm order, which yields a more realistic description of boson p_T compared with the fixed-order calculations, such as FEWZ. However, the difference between FEWZ asymmetry predictions and RESBOS predictions is negligible; and our measurement is not sensitive to the small difference between fixed-order and resummed calculations.

Figure 5.30 shows a comparison of measured asymmetries and theoretical

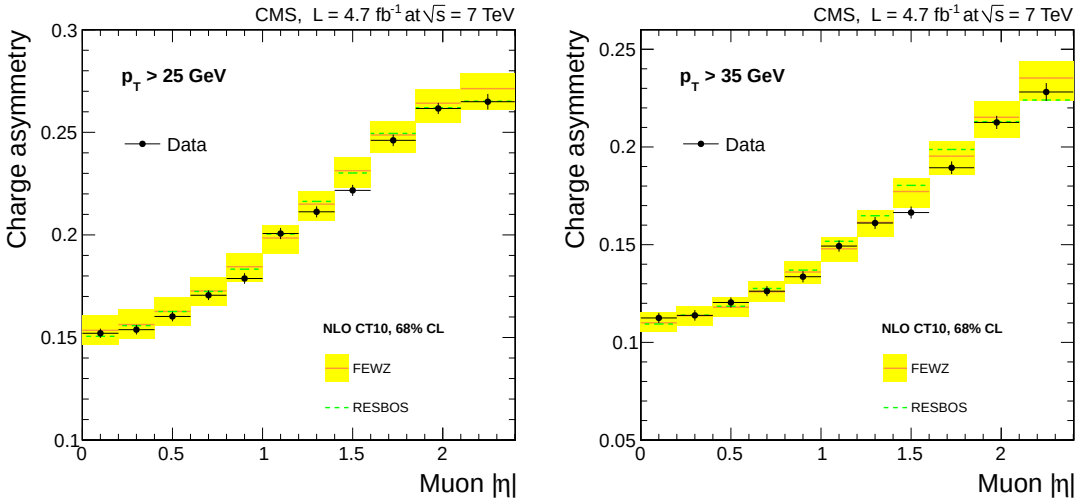

Figure 5.29: Comparison of the measured muon charge asymmetry with theoretical predictions based on the RESBOS and FEWZ 3.1 MC tools. The NLO CT10 PDF set is used in both calculations. The results are shown for muon $p_T > 25$ GeV (left) and $p_T > 35$ GeV (right).

predictions, using FEWZ 3.1 at NLO and NNLO QCD. Each calculation uses HERA PDF with a corresponding QCD order. In addition, the NNLO calculation was performed using the DYNNLO [68, 69] MC tool. The two MC tools' predictions agree within 1%. For the 25 GeV threshold of the muon, the predictions at NLO and at NNLO are very similar. For the 35 GeV threshold of the muon, the difference between the NLO and NNLO calculations becomes much more pronounced. However, the predictions still lie within the quoted PDF uncertainties.

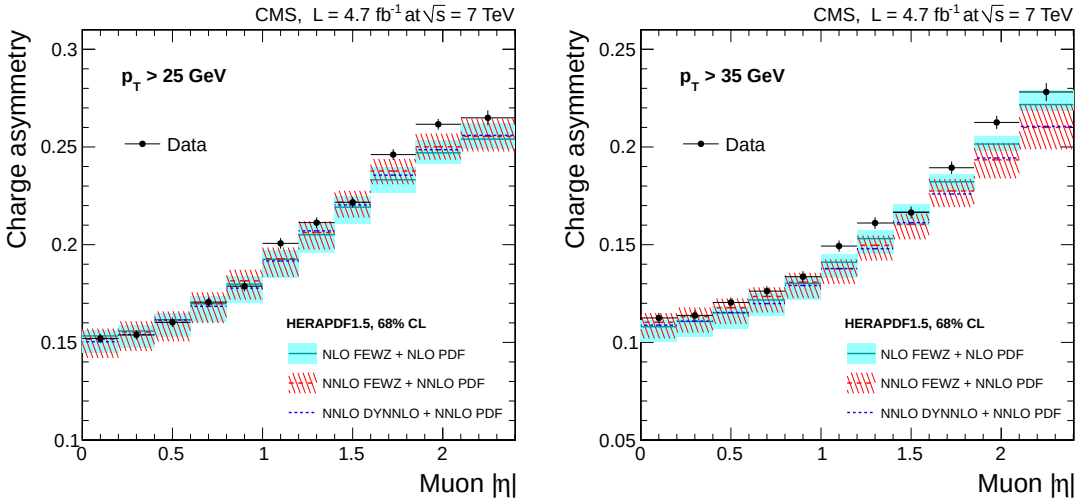

Figure 5.30: Comparison of the measured muon charge asymmetry with theoretical predictions at NNLO QCD for muon $p_T > 25$ GeV (left) and $p_T > 35$ GeV (right). The NNLO HERAPDF1.5 set is used in the NNLO calculations. Calculations are performed with the FEWZ and DYNNLO MC tools. For comparison, theoretical predictions for NLO FEWZ (using the NLO HERA PDF) are also displayed.

5.7 Impact of charge asymmetry on PDFs

Here we present the first QCD analysis, performed by HERA PDF experts, that studies the impact of our muon charge asymmetry results on HERA PDFs. The reference HERA PDFs are based on the neutral current (NC) and the charged current (CC) cross sections measured in the H1 and the ZEUS experiments. The muon charge asymmetry $\mathcal{A}(\eta)$ results in 11 bins of the muon pseudorapidity for $p_T > 25$ GeV are added to the reference dataset to study the impact of our results on the HERA PDFs.

The analysis is performed within the HERAFitter [70] framework at the NLO QCD, using the MCFM [60] tool for the calculations. The partons are evolved

from a starting scale of $Q_0^2 = 1.9\ \text{GeV}^2$ using the QCDNUM program [71]. Heavy quark contributions are treated with the *General Mass Variable Flavor Number* scheme [72], with $m_c = 1.4$ GeV and $m_b = 4.75$ GeV. Renormalization and factorization scales are set to the corresponding scale of the process, $\mu_R = \mu_F = Q$; and the strong coupling constant is set to the PDG value, $\alpha_S(M_Z) = 0.1176$ [14].

The following combinations of PDFs are floating in the fit at the starting scale:

$$\begin{aligned}
xu_v(x) &= A_{u_v} x^{B_{u_v}} (1-x)^{C_{u_v}} (1 + E_{u_v} x^2), \\
xd_v(x) &= A_{d_v} x^{B_{d_v}} (1-x)^{C_{d_v}}, \\
x\bar{U}(x) &= A_{\bar{U}} x^{B_{\bar{U}}} (1-x)^{C_{\bar{U}}}, \\
x\bar{D}(x) &= A_{\bar{D}} x^{B_{\bar{D}}} (1-x)^{C_{\bar{D}}} \\
xg(x) &= A_g x^{B_g} (1-x)^{C_g} + A_g x^{B_g} (1-x)^{C_g},
\end{aligned} \tag{5.38}$$

where $x\bar{U}(x) = x\bar{u}(x)$ and $x\bar{D} = x\bar{d}(x) + x\bar{s}(x)$. The normalization parameters A_{u_v}, A_{d_v}, A_g are fixed by QCD sum rules; B parameters describe the behavior of PDFs at small x; and C parameters describe their behavior at $x \to 1$. The following constraints $A_{\bar{u}} = A_{\bar{d}}$ and $B_{\bar{u}} = B_{\bar{d}}$ are applied to ensure the same normalization for $\bar{u}$ and $\bar{d}$ at small x. The second term in the gluon density provides more flexibility; $C_g' = 25$ value is motivated by the approach of the MSTW group [21]. As for the strange antiquark density, $B_{\bar{D}}$ is set equal to $B_{\bar{U}}$, and $A_{\bar{U}} = A_{\bar{D}}(1 - f_s)$, where $f_s = \bar{s}/(\bar{d} + \bar{s})$ is a strangeness fraction, and its value, $f_s = 0.31 \pm 0.08$, is taken[7] from [21]. A total of 13 parameters are floating in the fit.

Measurements used in this QCD analysis, along with the corresponding partial χ^2 values, are listed in Table 5.14. Figure 5.31 shows the valence quark distributions before and after the muon charge asymmetry data were included in

[7] HERA data are not sensitive to the strange quark density.

Table 5.14: Measurements used in the HERA QCD analysis and corresponding partial χ^2 values reported by the fit.

Dataset	χ^2 / NDF
H1+ ZEUS NC cross sections in $e^- p$	107 / 145
H1+ ZEUS NC cross sections in $e^+ p$	416 / 379
H1+ ZEUS CC cross sections in $e^- p$	20 / 34
H1+ ZEUS CC cross sections in $e^+ p$	36 / 34
CMS muon charge asymmetry in pp	15 / 11
Total	594 / 590

PDFs. As one can see, both u_v and d_v central distributions are significantly affected. Also, the asymmetry data significantly reduces the uncertainties on the valence d quark, which is poorly constrained by the HERA data alone.

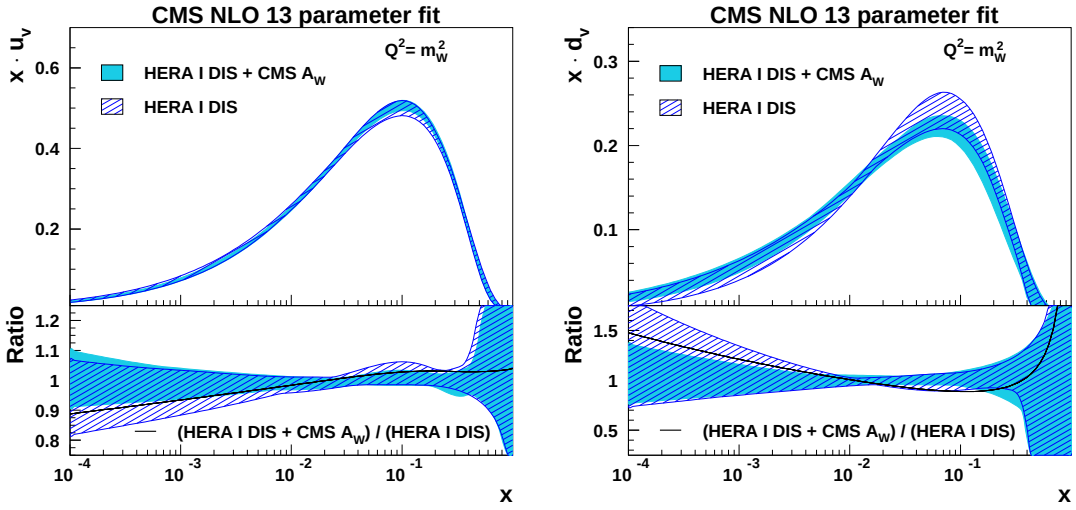

Figure 5.31: Valence u_v (left) and d_v (right) quark distributions in the HERA PDF model. The dashed band shows the PDF uncertainties corresponding to the reference HERA data, while the solid light-blue shows the new PDF uncertainties after our muon charge asymmetry results have been included. The solid line in the bottom panels shows the ratio between the new and the reference central PDFs.

CHAPTER 6

SUMMARY

We have presented a precision measurement of muon charge asymmetry in $pp \to W$ events at 7 TeV using a data sample corresponding to an integrated luminosity of 4.7 fb^{-1} collected with the CMS detector at the LHC. The asymmetry is measured in 11 bins of absolute muon pseudorapidity for two different muon p_T thresholds: 25 GeV and 35 GeV. The precision of this measurement is significantly improved compared with previous CMS asymmetry measurements. The total absolute uncertainty per bin is 0.2% – 0.4%.

The measured asymmetries are in good agreement with theoretical predictions calculated using the CT10, NNPDF2.3, and HERAPDF1.5 PDF models. The data are in poor agreement with the MSTW2008 model, although the agreement is significantly improved by using a more flexible parameterization of PDFs in the MSTW2008CPDEUT set.

We found the experimental errors to be significantly smaller than the current PDF uncertainties in the QCD calculations. Therefore, our measurement can be used to improve the determination of PDFs in future fits. We also presented the first QCD analysis performed by HERA PDF experts. The study showed that our results have a significant impact on the central distributions of both valence quarks in the proton. The asymmetry results we present also significantly reduce the uncertainty of d valence quark distribution in a HERA PDF model.

W charge asymmetry will be measured with the ~20 fb^{-1} of $\sqrt{s} = 8$ TeV data collected by CMS in 2012. The large data sample is expected to reduce the uncertainty of ϵ^+/ϵ^-, which is currently dominated by the statistical uncertainty

in the Drell-Yan control sample. However, since during the 2012 data-collection the pileup was significantly higher, the resolution of $\not{E}_{\mathrm{T}}$ is larger. Consequently, the ability to separate the signal from QCD events is expected to be poorer. Therefore, the systematic uncertainty of the QCD background is expected to be the dominating issue. This measurement will also serve as a preparatory step towards analyzing even higher pileup data of $\sqrt{s} = 13$ (14) TeV, which will extend the study of parton densities into different kinematic region of lower x-values.

BIBLIOGRAPHY

[1] CMS Collaboration, "Missing transverse energy performance of the CMS detector", *JINST* **6** (2011) P09001, doi:10.1088/1748-0221/6/09/P09001, arXiv:1106.5048.

[2] L. Evans and P. Bryant, "LHC Machine", *JINST* **3** (2008) S08001, doi:10.1088/1748-0221/3/08/S08001.

[3] CMS Collaboration, "The CMS experiment at the CERN LHC", *JINST* **3** (2008) S08004, doi:10.1088/1748-0221/3/08/S08004.

[4] R. K. Ellis, W. J. Stirling, and B. Webber, "QCD and collider physics", *Camb.Monogr.Part.Phys.Nucl.Phys.Cosmol.* **8** (1996) 1–435.

[5] G. Dissertori, I. Knowles, and M. Schmelling, "High energy experiments and theory". 2003.

[6] M. Gell-Mann, "A Schematic Model of Baryons and Mesons", *Phys.Lett.* **8** (1964) 214–215, doi:10.1016/S0031-9163(64)92001-3.

[7] G. Zweig, "An SU(3) model for strong interaction symmetry and its breaking. Pt. 1", Technical Report CERN-TH-401, (1964).

[8] H. Fritzsch, M. Gell-Mann, and H. Leutwyler, "Advantages of the Color Octet Gluon Picture", *Phys.Lett.* **B47** (1973) 365–368, doi:10.1016/0370-2693(73)90625-4.

[9] CTEQ Collaboration Collaboration, "Handbook of perturbative QCD: Version 1.0", *Rev.Mod.Phys.* **67** (1995) 157–248, doi:10.1103/RevModPhys.67.157.

[10] D. E. Soper, "Basics of QCD perturbation theory", arXiv:hep-ph/0011256.

[11] R. P. Feynman, "Very high-energy collisions of hadrons", *Phys.Rev.Lett.* **23** (1969) 1415–1417, doi:10.1103/PhysRevLett.23.1415.

[12] J. Bjorken and E. A. Paschos, "Inelastic Electron Proton and gamma Proton Scattering, and the Structure of the Nucleon", *Phys.Rev.* **185** (1969) 1975–1982, doi:10.1103/PhysRev.185.1975.

[13] CMS Collaboration, "Measurement of the 3-jet mass cross section in pp collisions at 7 TeV and determination of the strong coupling constant from 3-jet masses in the TeV range", Technical Report CMS-PAS-SMP-12-027, CERN, Geneva, (2013).

[14] Particle Data Group Collaboration, "Review of Particle Physics", *Phys. Rev. D* **86** (Jul, 2012) 010001, doi:10.1103/PhysRevD.86.010001.

[15] J. M. Campbell, J. Huston, and W. Stirling, "Hard Interactions of Quarks and Gluons: A Primer for LHC Physics", *Rept.Prog.Phys.* **70** (2007) 89, doi:10.1088/0034-4885/70/1/R02, arXiv:hep-ph/0611148.

[16] S. Drell and T.-M. Yan, "Partons and their Applications at High-Energies", *Annals Phys.* **66** (1971) 578, doi:10.1016/0003-4916(71)90071-6.

[17] G. Altarelli and G. Parisi, "Asymptotic Freedom in Parton Language", *Nucl. Phys. B* **126** (1977) 298, doi:10.1016/0550-3213(77)90384-4.

[18] V. Gribov and L. Lipatov, "Deep inelastic e p scattering in perturbation theory", *Sov. J. Nucl. Phys.* **15** (1972) 438–450.

[19] W. Stirling. private communication. http://www.hep.ph.ic.ac.uk/~wstirlin/plots/plots.html.

[20] H.-L. Lai et al., "New parton distributions for collider physics", *Phys.Rev.* **D82** (2010) 074024, doi:10.1103/PhysRevD.82.074024, arXiv:1007.2241.

[21] A. Martin, W. Stirling, R. Thorne, and G. Watt, "Parton distributions for the LHC", *Eur.Phys.J.* **C63** (2009) 189–285, doi:10.1140/epjc/s10052-009-1072-5, arXiv:0901.0002.

[22] R. D. Ball et al., "Parton distributions with LHC data", *Nucl. Phys. B* **867** (2013) 244–289, doi:10.1016/j.nuclphysb.2012.10.003, arXiv:1207.1303.

[23] H1,ZEUS Collaboration, "Combination and QCD analysis of the HERA inclusive cross sections", *PoS* **ICHEP2010** (2010) 168, arXiv:1308.0374.

[24] W. J. Stirling, "Progress in Parton Distribution Functions and implications for LHC",

doi:10.3204/DESY-PROC-2009-01/41,10.3360/dis.2008.4, arXiv:0812.2341.

[25] S. Alekhin et al., "The PDF4LHC Working Group Interim Report", arXiv:1101.0536.

[26] K. Melnikov and F. Petriello, "The W boson production cross section at the LHC through $O(\alpha_s^2)$", *Phys.Rev.Lett.* **96** (2006) 231803, doi:10.1103/PhysRevLett.96.231803, arXiv:hep-ph/0603182.

[27] C. Anastasiou, L. J. Dixon, K. Melnikov, and F. Petriello, "High precision QCD at hadron colliders: Electroweak gauge boson rapidity distributions at NNLO", *Phys.Rev.* **D69** (2004) 094008, doi:10.1103/PhysRevD.69.094008, arXiv:hep-ph/0312266.

[28] Y. Li and F. Petriello, "Combining QCD and electroweak corrections to dilepton production in FEWZ", arXiv:1208.5967.

[29] CDF Collaboration, "Direct measurement of the W production charge asymmetry in $p\bar{p}$ collisions at $\sqrt{s}$ = 1.96 TeV", *Phys. Rev. Lett.* **102** (2009) 181801, doi:10.1103/PhysRevLett.102.181801, arXiv:0901.2169.

[30] D0 Collaboration, "Measurement of the muon charge asymmetry in $p\bar{p} \to W + X \to \mu\nu + X$ events at $\sqrt{s}$ = 1.96 TeV", *Phys.Rev.* **D88** (2013) 091102, doi:10.1103/PhysRevD.88.091102, arXiv:1309.2591.

[31] CMS Collaboration, "Measurement of the lepton charge asymmetry in inclusive W production in pp collisions at $\sqrt{s}$ = 7 TeV", *JHEP* **04** (2011) 050, doi:10.1007/JHEP04(2011)050, arXiv:1103.3470v1.

[32] ATLAS Collaboration, "Measurement of the inclusive $W^{\pm}$ and Z/gamma cross sections in the electron and muon decay channels in pp collisions at $\sqrt{s}$ = 7 TeV with the ATLAS detector", *Phys.Rev.* **D85** (2012) 072004, doi:10.1103/PhysRevD.85.072004, arXiv:1109.5141.

[33] LHCb Collaboration, "Inclusive W and Z production in the forward region at $\sqrt{s}$ = 7 TeV", *JHEP* **06** (2012) 058, doi:10.1007/JHEP06(2012)058, arXiv:1204.1620v3.

[34] CMS Collaboration, "Measurement of the electron charge asymmetry in

inclusive W production in pp collisions at $\sqrt{s} = 7$ TeV", *Phys. Rev. Lett.* **109** (2012) 111806, doi:10.1103/PhysRevLett.109.111806, arXiv:1206.2598.

[35] CMS Collaboration, "Measurement of the muon charge asymmetry in inclusive W production in pp collisions at $\sqrt{s} = 7$ TeV", Technical Report CMS-PAS-EWK-11-005, CERN, Geneva, (2011).

[36] O. Bruning, H. Burkhardt, and S. Myers, "The Large Hadron Collider", *Prog.Part.Nucl.Phys.* **67** (2012) 705–734, doi:10.1016/j.ppnp.2012.03.001.

[37] CMS Collaboration, G. L. Bayatian et al., "CMS Physics: Technical Design Report Volume 1: Detector Performance and Software". Technical Design Report CMS. CERN, Geneva, 2006.

[38] CMS Collaboration, "Performance of the CMS Hadron Calorimeter with Cosmic Ray Muons and LHC Beam Data", *JINST* **5** (2010) T03012, doi:10.1088/1748-0221/5/03/T03012, arXiv:0911.4991.

[39] CMS Collaboration, "L1 Trigger DPG Results". https://twiki.cern.ch/twiki/bin/viewauth/CMSPublic/L1TriggerDPGResults.

[40] W. Adam, B. Mangano, T. Speer, and T. Todorov, "Track Reconstruction in the CMS tracker", Technical Report CMS-NOTE-2006-041, CERN, Geneva, (Dec, 2006).

[41] R. Fruhwirth, "Application of Kalman filtering to track and vertex fitting", *Nuclear Instruments and Methods in Physics Research Section A: Accelerators, Spectrometers, Detectors and Associated Equipment* **262** (1987), no. 23, 444 – 450, doi:http://dx.doi.org/10.1016/0168-9002(87)90887-4.

[42] CMS Collaboration, "Tracking and vertexing performance in CMS", Technical Report CMS-CR-2012-384. CERN-CMS-CR-2012-384, CERN, Geneva, (Dec, 2012).

[43] K. Rose, "Deterministic annealing for clustering, compression, classification, regression, and related optimization problems", *Proceedings of the IEEE* **86** (1998), no. 11, 2210–2239, doi:10.1109/5.726788.

[44] R. Fruhwirth, W. Waltenberger, and P. Vanlaer, "Adaptive vertex fitting", *J.Phys.* **G34** (2007) N343, doi:10.1088/0954-3899/34/12/N01.

[45] CMS Collaboration, "Performance of CMS muon reconstruction in pp collision events at $\sqrt{s}$ = 7 TeV", *JINST* **7** (2012) P10002, doi:10.1088/1748-0221/7/10/P10002, arXiv:1206.4071.

[46] CMS Collaboration, "Particle-Flow Event Reconstruction in CMS and Performance for Jets, Taus, and MET", Technical Report CMS-PAS-PFT-09-001, CERN, 2009. Geneva, (Apr, 2009).

[47] W. Adam, R. Fruhwirth, A. Strandlie, and T. Todorov, "Reconstruction of electrons with the Gaussian sum filter in the CMS tracker at LHC", *eConf* **C0303241** (2003) TULT009, doi:10.1088/0954-3899/31/9/N01, arXiv:physics/0306087.

[48] M. Cacciari, G. P. Salam, and G. Soyez, "The anti-k_t jet clustering algorithm", *JHEP* **04** (2008) 063, doi:10.1088/1126-6708/2008/04/063, arXiv:0802.1189.

[49] CMS Collaboration, "Measurements of Inclusive W and Z Cross Sections in pp Collisions at $\sqrt{s}$ = 7 TeV", *JHEP* **1101** (2011) 080, doi:10.1007/JHEP01(2011)080, arXiv:1012.2466.

[50] R. J. Barlow and C. Beeston, "Fitting using finite Monte Carlo samples", *Comput.Phys.Commun.* **77** (1993) 219–228, doi:10.1016/0010-4655(93)90005-W.

[51] CMS Collaboration, "CMS Luminosity Collision Data". https://twiki.cern.ch/twiki/bin/view/CMSPublic/LumiPublicResults2011.

[52] CMS Collaboration, "Absolute Calibration of Luminosity Measurement at CMS: Summer 2011 Update", Technical Report CMS-PAS-EWK-11-001, CERN, Geneva, (2011).

[53] S. Van der Meer, "Calibration of the effective beam height in the ISR", Technical Report CERN-ISR-PO-68-31. ISR-PO-68-31, CERN, Geneva, (1968).

[54] CMS Collaboration, "Absolute Calibration of the Luminosity Measurement at CMS: Winter 2012 Update", Technical Report CMS-PAS-SMP-12-008, CERN, Geneva, (2012).

[55] S. Frixione, P. Nason, and C. Oleari, "Matching NLO QCD computations

with parton shower simulations: the POWHEG method", *JHEP* **11** (2007) 070, doi:10.1088/1126-6708/2007/11/070, arXiv:0709.2092.

[56] T. Sjöstrand, S. Mrenna, and P. Z. Skands, "PYTHIA 6.4 physics and manual", *JHEP* **05** (2006) 026, doi:10.1088/1126-6708/2006/05/026, arXiv:hep-ph/0603175.

[57] Z. Was, "TAUOLA the library for tau lepton decay, and KKMC / KORALB / KORALZ /... status report", *Nucl. Phys. Proc. Suppl.* **98** (2001) 96–102, doi:10.1016/S0920-5632(01)01200-2, arXiv:hep-ph/0011305.

[58] GEANT4 Collaboration, "GEANT4: a simulation toolkit", *Nucl. Instrum. Meth. A* **506** (2003) 250–303, doi:10.1016/S0168-9002(03)01368-8.

[59] J. Pumplin et al., "New generation of parton distributions with uncertainties from global QCD analysis", *JHEP* **07** (2002) 012, doi:10.1088/1126-6708/2002/07/012, arXiv:hep-ph/0201195.

[60] J. M. Campbell and R. K. Ellis, "Radiative corrections to $Zb\bar{b}$ production", *Phys. Rev. D* **62** (2000) 114012, doi:10.1103/PhysRevD.62.114012, arXiv:hep-ph/0006304.

[61] A. Bodek et al., "Extracting Muon Momentum Scale Corrections for Hadron Collider Experiments", *Eur.Phys.J.* **C72** (2012) 2194, doi:10.1140/epjc/s10052-012-2194-8, arXiv:1208.3710.

[62] F. James, "MINUIT Function Minimization and Error Analysis: Reference Manual Version 94.1", Technical Report CERN-D-506, CERN-D506, (1994).

[63] J. Alwall et al., "MadGraph 5 : Going Beyond", *JHEP* **1106** (2011) 128, doi:10.1007/JHEP06(2011)128, arXiv:1106.0522.

[64] A. Martin et al., "Extended Parameterisations for MSTW PDFs and their effect on Lepton Charge Asymmetry from W Decays", *Eur. Phys. J. C* **73** (2013) 2318, doi:10.1140/epjc/s10052-013-2318-9, arXiv:1211.1215.

[65] G. A. Ladinsky and C. P. Yuan, "The nonperturbative regime in QCD resummation for gauge boson production at hadron colliders", *Phys. Rev.*

D **50** (1994) 4239, doi:10.1103/PhysRevD.50.R4239, arXiv:hep-ph/9311341.

[66] C. Balazs and C. P. Yuan, "Soft gluon effects on lepton pairs at hadron colliders", *Phys. Rev. D* **56** (1997) 5558–5583, doi:10.1103/PhysRevD.56.5558, arXiv:hep-ph/9704258.

[67] F. Landry, R. Brock, P. M. Nadolsky, and C. P. Yuan, "Tevatron Run-1 Z boson data and Collins-Soper-Sterman resummation formalism", *Phys. Rev. D* **67** (2003) 073016, doi:10.1103/PhysRevD.67.073016, arXiv:hep-ph/0212159.

[68] S. Catani et al., "Vector boson production at hadron colliders: A fully exclusive QCD calculation at NNLO", *Phys. Rev. Lett.* **103** (2009) 082001, doi:10.1103/PhysRevLett.103.082001, arXiv:0903.2120.

[69] S. Catani and M. Grazzini, "An NNLO subtraction formalism in hadron collisions and its application to Higgs boson production at the LHC", *Phys. Rev. Lett.* **98** (2007) 222002, doi:10.1103/PhysRevLett.98.222002, arXiv:hep-ph/0703012.

[70] https://www.herafitter.org/HERAFitter.

[71] M. Botje, "QCDNUM: Fast QCD Evolution and Convolution", *Comput.Phys.Commun.* **182** (2011) 490–532, doi:10.1016/j.cpc.2010.10.020, arXiv:1005.1481.

[72] R. Thorne, "A Variable-flavor number scheme for NNLO", *Phys. Rev. D* **73** (2006) 054019, doi:10.1103/PhysRevD.73.054019, arXiv:hep-ph/0601245.